Acta Polytechnica

Editorial Board:

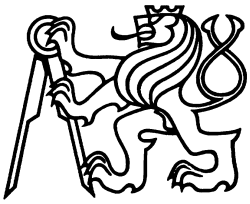

Title of journal: Acta Polytechnica. **Volume:** 62. **Number:** 3.
Periodicity: Bimonthly; 6 issues per year. **Date of issue:** June 30, 2022.
Published by: Czech Technical University in Prague,
Jugoslávských partyzánů 1580/3, 160 00 Praha 6 – Dejvice, Czech Republic.
IČO: 68407700.

Editorial Office: CTU — Central Library,
Technická 6, 160 80 Praha 6, Czech Republic.
acta@cvut.cz

Acta Polytechnica is available at http://ojs.cvut.cz/ojs/index.php/ap
Each article is assigned a digital object identifier https://doi.org/10.14311/AP.2022.62.⟨*4-digit article page number*⟩

ISSN 1805–2363 (online) MK ČR E 4923

Dear Reader

The Acta Polytechnica journal that you have just opened is a scientific journal published by the Czech Technical University in Prague. This journal first appeared in 1961 under the name "Proceedings of the Czech Technical University". The main purpose of the journal was to support publication of the results of scientific and research activities at the Czech technical universities. Five years later, in 1966, the name of the journal was changed to Acta Polytechnica, and it started appearing quarterly. The main title Acta Polytechnica is accompanied by the subtitle Journal of Advanced Engineering, which expresses the scope of the journal more precisely. Acta Polytechnica covers a wide spectrum of engineering topics in civil engineering, mechanical engineering, electrical engineering, nuclear sciences and physical engineering, architecture, transportation science, biomedical engineering and computer science and engineering. The scope of the journal is not limited to the realm of engineering. We also publish articles from the area of natural sciences, in particular physics and mathematics.

Acta Polytechnica is now being published in an enlarged format. Our aim is to be a high-quality multi-disciplinary journal publishing the results of basic research and also applied research. We place emphasis on the quality of all published papers. The journal should also serve as a bridge between basic research in natural sciences and applied research in all technical disciplines.

We invite researchers to submit high-quality original papers. The conditions of the submission process are explained in detail on: `http://ojs.cvut.cz/ojs/index.php/ap`. All papers will be reviewed, and accepted papers are published in English.

We hope that you will find our journal interesting, and that it will serve as a valuable source of scientific information.

Editorial Board

Contents

MEASUREMENT OF SOLID PARTICLE EMISSIONS FROM OXY-FUEL COMBUSTION OF BIOMASS IN FLUIDIZED BED

Ondřej Červený*, Pavel Vybíral, Jiří Hemerka, Luděk Mareš

Czech Technical University in Prague, Faculty of Mechanical Engineering, Department of Environmental Engineering, Technická 4, 166 07 Prague, Czech Republic

* corresponding author: ondrej.cerveny@fs.cvut.cz

Abstract. The presented work summarizes the results of the measurement of solid particle emissions from an experimental 30 kW combustion unit. This unit has been used for the research of oxy-fuel combustion of biomass in a fluidized bed, which, when accompanied with carbon capture technologies, is one of the promising ways for decreasing the amount of CO_2 in the atmosphere. To implement a carbon capture system, it is first needed to separate various impurities from the flue gas. Therefore, the goal of this work was to identify solid particles contained in the flue gas.

Part of the apparatus used for this measurement was an ejector dilutor. To evaluate the results of this measurement, it is key to know the dilution ratio of the dilutor. For this purpose, a method for determining the dilution ratio of an ejector dilutor was proposed and experimentally verified.

Keywords: Oxy-fuel biomass combustion, solid particle emission, ejector dilutor, dilution ratio.

1. Introduction

As global warming is becoming an increasingly pressing issue, people are starting to look for new ways of decreasing carbon dioxide emissions. According to EPA [1], CO_2 is widely considered the most important anthropogenic greenhouse gas. Still, coal is one of the main energy sources and it contributes with approximately 40 % to the total energy production [2]. Replacing or cofiring coal with biomass fuels and utilization of carbon capture systems is one of the ways to reduce CO_2 emissions. We recognize two carbon capture systems: carbon capture and storage (CCS) and carbon capture and use/utilization (CCU). By combusting biomass with CCS or CCU system implemented, we can achieve negative or neutral CO_2 emissions, respectively [3].

The goal of this work was to identify solid particle emissions from the process of oxy-fuel biomass combustion in a fluidized bed. As a part of Research Center for Low-Carbon Energy Technologies project, this measurement was performed to get data for an efficient solid particle separation. This measurement took place on an experimental 30 kW combustion unit, which is shown in Figure 1. The fuel used for the experiment were spruce wooden pellets with 6 mm diameter.

A part of the apparatus is an ejector dilutor. To get the correct data from such a measurement, it is needed to know the actual dilution ratio of the dilutor. Although this ratio is provided by the manufacturer of the dilutor (in our case Dekati®), the real dilution ratio may differ. As stated in [5], the dilution ratio is influenced by the composition of the gas. Thus, when the nominal values of the dilution ratio are obtained using air, it is clear that these values will not be appropriate when diluting flue gas, as in our case. The composition of the gas may change the dilution ratio by 20 %, which would cause a quite significant error in the results. Specifically, the composition of the flue gas in our case was ca. 90 % CO_2, 6 % O_2 and some minor gases in the dry flue gas. Wet flue gas had around 40 % vol. water vapour content. This composition can be calculated using equations from [6], where the authors described the oxy-fuel combustion specifics. The secondary goal of this work was, therefore, to set and verify a method to obtain a more accurate dilution ratio for gases different from the calibration

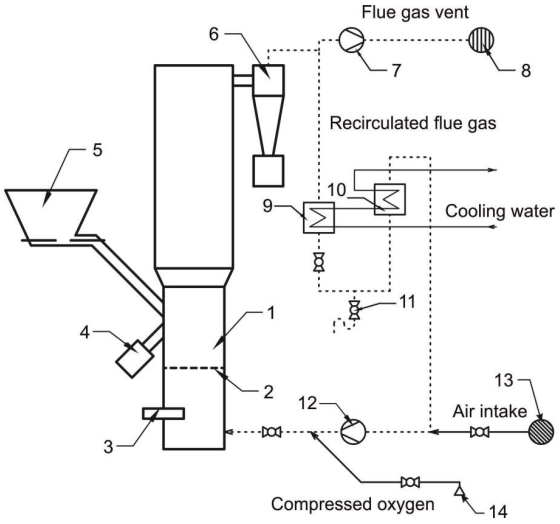

Figure 1. Scheme of the 30 kWth BFB experimental facility 1) fluidized bed region, 2) distributor of the fluidizing gas, 3) gas burner mount, 4) fluidized bed spill way, 5) fuel feeder, 6) cyclone separator, 7) flue gas fan, 8) flue gas vent, 9) and 10) water coolers, 11) condensate drain, 12) primary fan, 13) air-suck pipe, 14) vessels with oxygen [4].

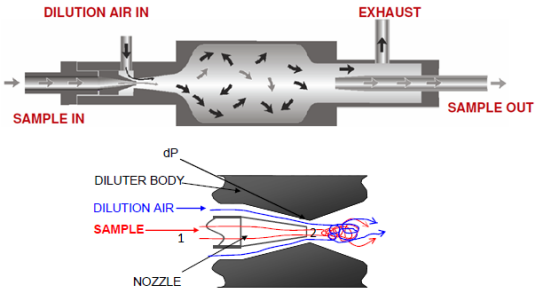

Figure 2. Operating principle of Dekati® dilutor [7].

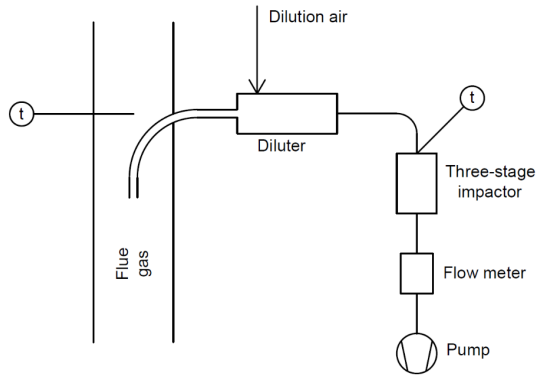

Figure 3. Scheme of experimental set-up of solid particle emission measurement.

gas. The operating principle of the ejector dilutor is shown in Figure 2. Pressurized dilution air enters the dilutor and is accelerated in the orifice ring, which causes a vacuum in front of the sample nozzle and the sample gas is sucked in. These two gases are mixed and then leave the dilutor.

2. Method

2.1. Solid particle emission measurement

To determine the properties of solid particles contained in the flue gas, we used the gravimetric analysis. The apparatus used was a three-stage impactor with an ejector dilutor, both from Dekati® company. The scheme of the experimental set-up can be seen in Figure 3. The impactor classifies the solid particles into three fractions, which are PM10, PM2,5 and PM1. The use of the dilutor provides a longer running time for each measurement. That is desirable, because the impaction plates of the impactor have a limited mass capacity, about 1 mg each. Additionally, it helps to avoid condensation of water vapour, which is useful here, because the flue gas from this combustion technology is specific for its high water vapour content (around 40 % vol.). The dilutor was heated up to the temperature of the flue gas in the vent (200 °C). The dilution air had an ambient temperature and was dried before feeding into diluter.

2.2. Correction of the dilution ratio for a gas of general composition

The following method is based on the theory of gas flow through a nozzle. To use it, we have to know the nominal dilution ratio (obtained with air) and the composition of the gas we are diluting. The method consists in comparing the air flow rate and the desired gas flow rate through the entry nozzle. The procedure is as follows. On the basis of the theoretically calculated air and gas flow rates, the air flow rate measured during the calibration is corrected to correspond to the case when the different gas would enter the nozzle under the same conditions (temperature and pressure). To calculate the mass flow rate through the nozzle, we use Saint-Venant-Wantzel equation [8] in the following form:

$$\dot{m}_s = K_s \times \rho_{s,1} \times A_{s,2} \left(\frac{P_{s,2}}{P_{s,1}}\right)^{\frac{1}{\kappa_s}} \times \left(\frac{2\kappa_s}{\kappa_s - 1} \frac{P_{s,1}}{\rho_{s,1}} \left(1 - \left(\frac{P_{s,2}}{P_{s,1}}\right)^{\frac{\kappa_s - 1}{\kappa_s}}\right)\right)^{\frac{1}{2}} \quad (1)$$

Index 1 in equation (1) indicates the point of entry into the dilutor, index 2 is the narrowest point of the nozzle – its outlet. ρ_s is the density, A_s flow cross section, P_s static pressure, κ_s Poisson's constant and K_s coefficient, which takes into account the internal friction and contraction of the flow. It follows from equation (1) that the flow rate depends on the composition, here expressed by density and Poisson's constant, and the state of the gas.

Mass flow rates obtained using equation (1) are first converted to volume flow rates and then their ratio is expressed:

$$VR = \frac{\dot{V}_{air,teor}}{\dot{V}_{gas,teor}}. \quad (2)$$

This calculated VR ratio is then used to convert the measured air flow rate to the desired gas flow rate:

$$\dot{V}_{gas} = \frac{\dot{V}_{air}}{VR}. \quad (3)$$

Now, with the knowledge of the gas flow V_{gas} and the dilution air flow V_{DA}, it is possible to determine the dilution ratio as given by equation (4):

$$N_{gas} = \frac{\dot{V}_{DA} + \dot{V}_{gas}}{\dot{V}_{gas}}. \quad (4)$$

By adjusting equations (3) and (4), an equation for a direct conversion between the dilution ratio with air N_{air} (nominal) and with gas N_{gas} can be obtained:

$$N_{gas} = (N_{air} - 1)VR + 1. \quad (5)$$

2.2.1. Experimental verification

To verify the method described in the previous section, an experimental measurement was performed using

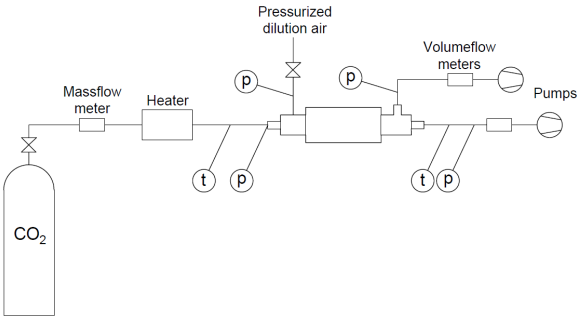

FIGURE 4. Scheme of the experimental set-up.

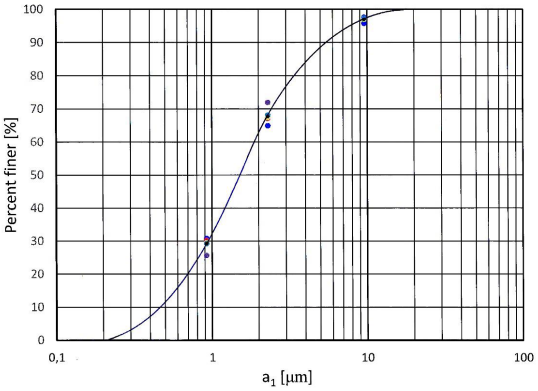

FIGURE 5. Particle size distribution curve.

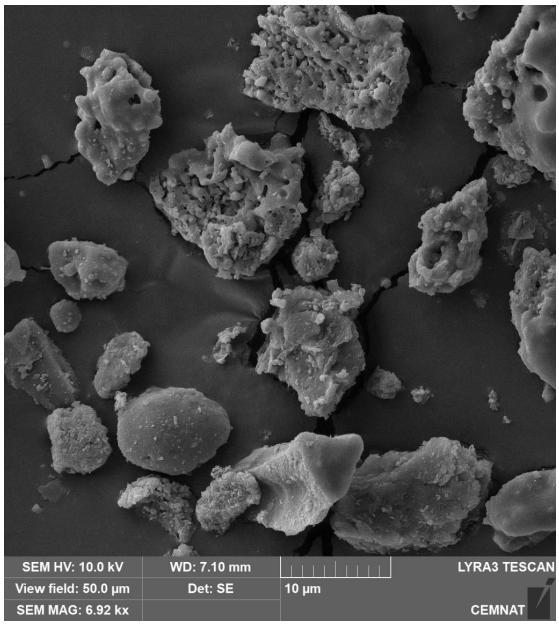

FIGURE 6. PM2,5 particles captured in the impactor.

carbon dioxide as the diluted gas. Dekati® dilutor in Figure 2 was used. The overpressure of the dilution air was set to nominal 2×10^5 Pa. The flow rate and pressure were measured at the sample inlet and both dilutor outlets. A heater preceded the sample inlet and the measurement was performed in the range from room temperature to a temperature of about 200 °C. This temperature was measured using a thermocouple placed in the gas stream before the entrance to the dilutor. The dilution air had ambient temperature during the whole experiment. The experimental set-up is shown in Figure 4. To calculate the flow rate according to equation (1), it is necessary to determine the static pressure $P_{s,2}$, which causes the suction of the sample gas. This can be achieved by blocking the sample inlet to the dilutor and measuring the static pressure there without the sample gas flowing in. Similarly, the dilution air flow rate V_{DA} can be determined, again, by blocking the sample inlet and measuring the two outlet flow rates of the dilutor.

3. Results and discussion

3.1. Solid particle emission characteristics

With the apparatus described, we performed five separated measurements and specified the concentration and particle size distribution in the flue gas. Cut-off diameters of the impactor were corrected according to temperature. The acquired particle size distribution is shown in Figure 5 with a curve plotted with the average values. Our results showed a relatively small mass median aerodynamic diameter of 1.6 µm. The solid particle concentration in the flue gas was found to be cca 30 mg/mN^3. It is important to add that these results were influenced by the fact that the flue gas goes through a cyclone before exhausting to the vent, as can be seen in Figure 1. According to different theories, the cut-off diameter of this cyclone was estimated to lay between 3 and 5 µm. That explains the relatively small median and concentration found.

Images of the particles captured in the impactor have been taken with an electron microscope. In Figure 6, there is an image of particles captured in the second stage of the impactor. This picture shows many particles larger than 2.5 µm, which should be the cut-off diameter of this stage. These particles correspond to particles penetrating from the previous stage.

3.2. Evaluation of the proposed method for dilution ratio correction

Experimental measurements with CO_2, the results of which can be seen in Figure 7, showed a very good agreement between the presented method and the experiment. The average value of the deviation between the measured and calculated values of the dilution ratio is, on average, about 1 % over the entire temperature course. The largest deviation was found at room temperature, where it reaches about 3 %. Figure 7 also demonstrates how a significant error can be caused by using the air dilution ratio N_{air} for a different gas. In the case of CO_2, the error is almost 20 %. The same figure also shows that the dilution ratio also varies with the sample gas temperature, which is another factor that should be remembered during field measurements.

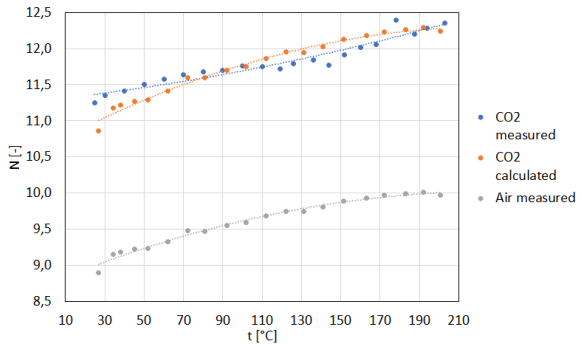

Figure 7. Values of dilution ratio obtained using the given method and experimentally by measurement as a function of sample gas temperature.

4. Conclusions

A measurement on the experimental 30 kW boiler during a biomass combustion in oxy-fuel regime was carried out to specify the solid particle emission present in the flue gas. We found a relatively small mass median aerodynamic diameter of 1.6 µm and a concentration of 30 mg/m$_N^3$. Both these values were affected by the presence of a cyclone at the outlet of the boiler. The results of this measurement will be used for the design of an appropriate precipitator for this combustion technology. To correctly interpret the data acquired during the solid particle emission measurement, there rose a need to specify the dilution ratio of the ejector dilutor we used for the measurement. Therefore, in this paper, we also proposed and experimentally verified a method for a correction of the nominal dilution ratio to fit the actual case during a field measurement. The experimentally obtained data differ from the proposed method by an average of about 1 %. This method could find good use wherever the sample gas composition differs from air (calibration gas) and the knowledge of accurate concentrations of the sample is important. Such cases might be, for example, boiler flue gases or car exhaust gases.

Acknowledgements

This work was supported by projects Research Center for Low-Carbon Energy Technologies CZ.02.1.01/0.0/0.0/16_019/0000753 and Optimization of HVAC systems SGS22/154/OHK2/3T/12. We gratefully acknowledge the support from these grants. We would also like to thank Ing. Stanislav Šlang, Ph.D. for providing us the electron microscope photos of the impactor stages.

References

[1] EPA. Greenhouse gases. [2021-10-18], https://www.epa.gov/report-environment/greenhouse-gases.

[2] S. Black, J. Szuhánszki, A. Pranzitelli, et al. Effects of firing coal and biomass under oxy-fuel conditions in a power plant boiler using CFD modelling. *Fuel* **113**:780–786, 2013. https://doi.org/10.1016/j.fuel.2013.03.075.

[3] T. Mendiara, F. García-Labiano, A. Abad, et al. Negative CO_2 emissions through the use of biofuels in chemical looping technology: A review. *Applied Energy* **232**:657–684, 2018. https://doi.org/10.1016/j.apenergy.2018.09.201.

[4] M. Vodička, N. E. Haugen, A. Gruber, J. Hrdlička. NO_X formation in oxy-fuel combustion of lignite in a bubbling fluidized bed – Modelling and experimental verification. *International Journal of Greenhouse Gas Control* **76**:208–214, 2018. https://doi.org/10.1016/j.ijggc.2018.07.007.

[5] B. Giechaskiel, L. Ntziachristos, Z. Samaras. Calibration and modelling of ejector dilutors for automotive exhaust sampling. *Measurement Science and Technology* **15**(11):2199–2206, 2004. https://doi.org/10.1088/0957-0233/15/11/004.

[6] P. Skopec, J. Hrdlička. Specific features of the oxyfuel combustion conditions in a bubbling fluidized bed. *Acta Polytechnica* **56**(4):312–318, 2016. https://doi.org/10.14311/AP.2016.56.0312.

[7] Dekati Ltd. Ejector diluter in exhaust measurements: Technical note, 2001.

[8] A. J. C. Barré de Saint-Venant, P. L. Wantzel. Mémoire et expériences sur l'écoulement de l'air, déterminé par des différences de pression considérables. *Journal de l'École polytechnique* **27**:85–122, 1839.

APPLICABILITY OF SECONDARY DENITRIFICATION MEASURES ON A FLUIDIZED BED BOILER

Jitka Jeníková*, Kristýna Michaliková, František Hrdlička, Jan Hrdlička, Lukáš Pilař, Matěj Vodička, Pavel Skopec

Czech Technical University in Prague, Faculty of Mechanical Engineering, Department of Energy Engineering, Technická 4, Prague 6, Dejvice, 160 00, Czech Republic

* corresponding author: jitka.jenikova@fs.cvut.cz

Abstract. This article compares the performance of selective catalytic reduction (SCR) and selective non-catalytic reduction (SNCR) applied on the same pilot unit, a 500 kW fluidized bed boiler burning Czech lignite. A correlation of the denitrification efficiency and the normalized stoichiometric ratio (NSR) is investigated. The fundamental principle of the SCR and SNCR is similar with the same reaction scheme. The difference is in the use of the catalyst that lowers the activation energy of the key reaction. As a result, the reduction is performed at lower temperatures during the SCR method. During experiments, the NSR was up to 1.6 for the SCR method. For the SNCR method, which has a higher reducing agent consumption, the maximum denitrification efficiency was reached for NSR of about 2.5. The efficiency of both secondary methods was investigated. The denitrification efficiency during experiments exceeded 98 % for the SCR method, and the SNCR method, together with the primary measures, reached an efficiency of 58 %.

Keywords: SCR, SNCR, fluidized bed boiler, denitrification, deNO$_X$, coal.

1. Introduction

Many countries rely on and will have to rely on the combustion of fossil fuels for electricity and heat production over the next few years. The combustion of fossil fuels is associated with the production of pollutants that must be minimized in order to operate the technology with low environmental impacts. Nitrogen oxides can be identified among typical pollutants and are responsible for acid gas deposition, ozone depletion, and health effects on humans. In the field of pollutant reduction, the most important regulation is given by the BAT (Best Available Techniques) Reference Document for Large Combustion Plants (LCP) [1] that describes the primary and secondary measures to reduce the release of nitrogen oxides (so-called denitrification) from combustion plants to the atmosphere. These measures, which are usable for fluidized bed boilers, are summarized in Table 1 with the corresponding general NO_X reduction rates efficiencies.

Primary measures	**NO_X reduction rate [%]**
Low excess air firing	10–44
Air staging	10–77
Flue-gas recirculation (FGR)	20–60
Reduction of the combustion air temperature	20–30
Secondary measures	
Selective catalytic reduction (SCR)	80–95
Selective non-catalytic reduction (SNCR)	30–50

Table 1. NO_X reduction rates of primary and secondary measures [1].

This article is focused on the experimental investigation of secondary denitrification measures in a bubbling fluidized bed boiler using Czech lignite as a fuel. Reachable denitrification levels are analysed using the SCR and SNCR technologies. The mitigation of nitrogen oxides is important for more than just meeting the BAT and emission standards. Regarding upcoming trends of lowering CO_2 emissions from energy conversion, combustion systems using fossil fuels can be extended by CCS/U technologies, most typically post-combustion systems or oxy-fuel combustion. The reduction in NO_X production is crucial for those technologies as well, since a high purity of CO_2 and low levels of acid-forming gases (like nitrogen oxides) are required.

2. Nitrogen oxides

2.1. Formation of NO_X emissions

There are three known mechanisms of nitrogen oxides formation in combustion processes [2–4]:

- thermal NO_X – oxidation of molecular nitrogen from the oxidant at high temperatures, known as the Zeldovich mechanism,
- fuel NO_X – oxidation of chemically bound nitrogen in solid fuels,

- prompt NO_X – reactions of molecular nitrogen with hydrocarbon radicals with subsequent oxidation of intermediate products in high-temperature reducing flame zones, known as the Fenimore mechanism.

NO_X from conventional coal combustion typically consists of nitric oxide (NO) and nitrogen dioxide (NO_2), where NO is the most dominant with a share of about 90 % and more. The dominating formation mechanisms depend on the type of combustor. In the high-temperature systems, e.g. pulverized coal combustion, Zeldovich and Fenimore mechanisms are more dominant, while fuel-N oxidation dominates in fluidized beds. The fuel-N mechanism is only weakly dependent on the combustion temperature, and there is a proportional correlation with oxygen stoichiometry [5–8]. In addition to NO and NO_2, a significant nitrous oxide production (N_2O) can also be observed. N_2O is not part of NO_X emission limits and the measures for its reduction are not part of BAT, it is a gas of importance due to its high GWP potential [9]. The measured N_2O emissions from coal combustion systems (except fluidized bed) as the ratio of N_2O/NO_X emissions are typically less than 2 percent [4]. For coal-fired fluidized bed combustors, N_2O emissions are within the range of 17 to 48 % of overall NO_X emissions [4]. N_2O is produced in fluidized bed boilers due to its dependence on the bed temperature. A higher temperature leads to lower N_2O emissions, which is the reverse of the bed temperature dependence of NO formation [10]. The amount of conversion of fuel-bound nitrogen to NO and N_2O is considered to be roughly constant as shown by de las Obras-Loscertales et al. [11].

2.2. Denitrification methods

Denitrification is a general term for a NO_X limitation. Technologies for NO_X reduction can be categorized into primary measures that consist of modifying the operating parameters of combustion, leading to a suppression of the formation mechanisms, and secondary measures. Secondary measures represent flue gas treatment leading to the reduction of NO_X already formed. Those technologies can be used independently or in combinations.

2.2.1. Primary measures

The primary measures are typically most effective for the Zeldovich and Fenimore mechanisms, and they are focused on reducing the oxygen available in the combustion zone and reducing the peak temperatures. Primary measures technologies include air or fuel staging, low NO_X burners, and flue gas recirculation systems.

When solid fuels are burned in fluidized bed boilers, the relevant measures to reduce the NO_X production are those that focus on fuel-N-originating NO_X. As explained in Section 2.1, the fuel-NO_X mechanism is mostly dependent on the concentration of oxygen in the primary combustion zone. Therefore, the most effective measures aim only at lowering the stoichiometry of the primary air and not at lowering the combustion temperature, since the fluidized bed temperature is inevitably too low for the thermal and prompt mechanism to occur. In particular, the only primary measure, which is not an inherent part of the fluidized bed combustion control process, is the staged injection of combustion air. It is used to achieve the required combustion parameters, such as sub-stoichiometric conditions in the dense bed (which decrease the NO_X formation), simultaneous combustion of the unburned CO in the freeboard section, and increase of the freeboard temperature for efficient injection of the reducing agent. When secondary air is used to burn unburned CO, no more nitrogen oxides are formed in the freeboard section [3, 12–16]. Air staging has been shown to be an effective primary measure for NO_X reduction in a fluidized bed boiler; for example, Lupiáñez et al. [13] observed a 40 % reduction in NO_X for a 20 % secondary air ratio as compared to NO_X without air staging. However, air staging shows insufficient NO_X reduction rates to meet the emission limits defined in the LCP directive, and secondary measures have to be applied.

2.2.2. Secondary measures

Secondary measures, also called post-combustion methods, represent a group of chemical processes in which already formed nitrogen oxides are decomposed into molecular nitrogen and water vapor using a reducing agent. Typical reducing agents are ammonia and urea solutions. Selective non-catalytic reduction and selective catalytic reduction are the basic secondary methods. Other processes developed to date, such as simultaneous denitrification and desulphurization methods or wet scrubbing, have not been applied on a larger scale [7, 17, 18].

SNCR The selective non-catalytic reduction is a method that reduces nitrogen oxides in the absence of a catalyst. The process is based on the following reaction [18]:

$$4\,NH_3 + 4\,NO + O_2 \longrightarrow 4\,N_2 + 6\,H_2O \qquad (1)$$

To achieve a sufficient NO to N_2 conversion, the reaction temperature of 900 °C is required according to the calculation of the Gibbs energy. The typical temperature window for SNCR in industrial applications is between 850 and 1100 °C. When the reducing agent is injected into the low temperature region, the nitrogen oxides do not react with the NH_2 radical due to the low reaction rate and unreacted ammonia leaves the combustor with the flue gas. As a result, the concentration of ammonia in the flue gas increases and it may also be adsorbed on fly ash particles. On the other hand, when the reducing agent is injected above the high boundary of the temperature range, the NH_2 radical preferentially begins to react with

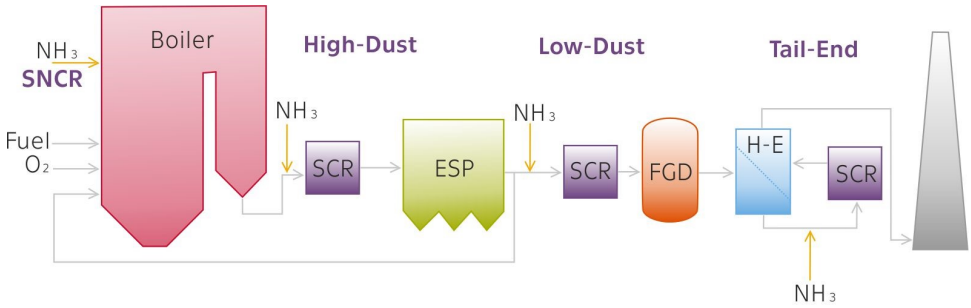

FIGURE 1. Possible locations of secondary denitrification measures.

oxygen, resulting in an increase in NO_X concentration in the flue gas. The efficiency of this method is, therefore, highly dependent on the injection of the reducing agent at the right temperature, which can differ with the used reducing agent. The optimum temperature for the reaction also varies depending on the reducing agent used. For example, for ammonia, it is in the range of 850–1000 °C, and for urea, between 950–1100 °C [4–6, 17].

SCR The fundamental principle of the selective catalytic reduction is similar to that of the non-selective reduction with the same reaction scheme. In this method, a catalyst is used that lowers the activation energy of the key reaction. As a result, the reduction can be performed at lower temperatures, and there is no need to keep the reacting substances for the necessary period of time in the high-temperature region. Depending on the type of catalyst, the temperature window can be 250 °C to 600 °C (for zeolite catalysts) [7], but the most commonly used vanadium pentoxide catalyst in the titanium dioxide carrier has an optimal temperature window of 250–430 °C with an achievable denitrification efficiency of more than 90 % [3, 7, 17, 19]. The lower temperature limit is set by the reaction rate and formation and deposition of the ammonium sulphate salt, which may deposit on the catalyst and cause its temporary deactivation. The upper temperature limit is established by physical damage to the catalyst by sintering and by oxidation of NH_3 to NO, thus limiting the NO_X conversion, and by supersaturation of the catalyst that leads to an excess of unreacted ammonia, which escapes along with the combustion gas [4, 18, 20]. The latest V_2O_5-based SCR catalysts are produced with the addition of tungsten trioxide (WO_3) and molybdenum trioxide (MoO_3), which are added for the expansion of the optimal temperature window and because of their ability to resist catalyst poisoning. These are applied by impregnation on a TiO_2 support that has a good resistance to sulfur oxides. This support is coated on the ceramic skeleton of the catalyst body. Vanadium catalysts work the best at temperatures of about 350 °C [5]. At lower temperatures, their efficiency decreases rapidly and at higher temperatures, corrosion problems arise [2, 7, 19]. The catalyst can be placed at different locations along the flue gas conduit as shown in Figure 1, and the placement depends on its type and material. It is not appropriate to place the catalyst in the high dust region for the fluidized bed combustion while using the dry additive desulfurization method because of the high abrasion properties of the present particles.

3. Experimental set-up

3.1. Experimental facility

The experimental boiler is located in the CTU laboratories in Prague. This pilot unit is a fluidized bed boiler with a thermal output of 500 kW, and its scheme is shown in Figure 2.

Fluidization is achieved by primary air together with recirculated flue gas passing through the distributor, which consists of 36 nozzles. The distributor is described in detail in [21] and the boiler in [22]. The combustion chamber has a cylindrical cross section. In the freeboard area, there are 6 thermocouples placed along the height. The secondary air is supplied to the freeboard section by four evenly placed distributors on a perimeter, and each distributor can provide a secondary air inlet at 4 different heights. The heat exchanger is located in the second descending draft of the boiler. The flue gases are sampled downstream of the boiler prior to the cyclone particle separator, and its composition is continuously analysed. In particular, the volumetric fractions of the following components are measured: O_2 using a paramagnetic sensor; SO_2, NO_X, CO_2 and CO using NDIR analysers. The boiler can also be operated in oxy-fuel mode. The off gas was also sampled downstream of the deNO_X unit and analysed using the multicomponent FT-IR analyser.

The SNCR reducing agent distribution line basically consists of two main components: a probe with a spray nozzle and a system for transporting the reducing agent to the spray system. The probe is cooled by water to prevent the reducing agent from boiling before it is sprayed. Compressed air is introduced in front of the nozzle orifice to improve the atomization of the supplied reducing agent. It is possible to place the probe in various inspection holes in the combustion space of the boiler and thus change the height of the injection of the reducing agent. For the experiments, secondary air inlets at a height of

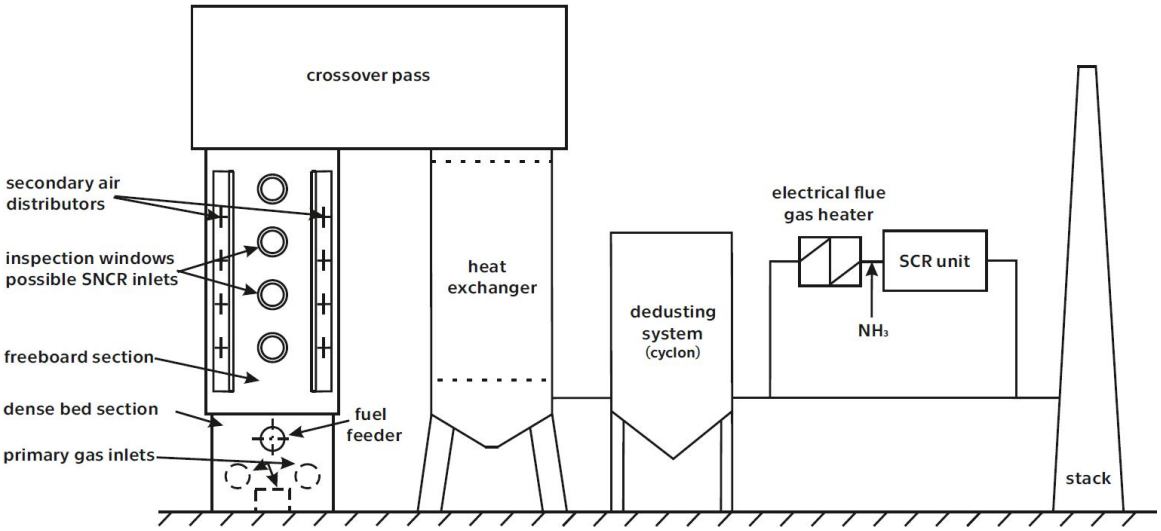

Figure 2. Fluidized bed boiler scheme.

Properties "As received"			Properties "Dry ash free"				
LHV [MJ/kg]	Water [wt. %]	Ash [wt. %]	C [wt. %]	H [wt. %]	O [wt. %]	N [wt. %]	S [wt. %]
18.5	25.0	9.3	72.3	6.3	19.0	1.1	1.3

Table 2. Proximate and ultimate analysis of the fuel

550 mm above the fluidized bed were used to achieve the optimal temperature window.

The catalyst for the SCR method has dimensions of 160 mm × 160 mm × 1260 mm. The reduction of NO_X in the flue gas is carried out by means of ammonia, which is dosed into the flue gas stream before the reactor itself. The technology is connected to the output of a cyclone separator from the fluidized bed boiler. Dedusted flue gases at a temperature of 150–180 °C are heated in an electric heater to the required temperature of 250–300 °C. The amount of flue gas that passes through the reactor at a speed of 4.5 m/s through the catalyst is approximately 150 Nm3/hour. It is necessary to inject the ammonia gas into the flue gas for the reaction on the catalyst surface. The stoichiometric amount of ammonia is approximately 0.012–0.016 kg/h. The catalyst itself is a honeycomb-type based on vanadium pentoxide (V_2O_5) with the addition of tungsten trioxide (WO_3) and molybdenum trioxide (MoO_3). Doping is applied by impregnation of the TiO_2 supporting body and is used to improve the mechanical stability and chemical resistance of the catalyst, which is related to the widening of the optimal temperature window.

3.2. Fuel and reducing agents

Lignite from the coal basin of North Bohemia was used as fuel for the experiments. Its proximate and ultimate analysis is shown in Table 2. The size of the coal particles was less than 10 mm. Pure ammonia was used as the SCR reducing agent and AdBlue (a chemically highly pure aqueous solution of synthetic urea – 32.5 % wt. urea) was used for the SNCR.

3.3. Methods

The normalized stoichiometric ratio is the proportion of the molar ratio of the reducing agent and nitrogen oxides at the beginning of the denitrification process. The range of variables measured was as follows. A detailed description of the variables is given in Table 2, where the O_2 concentrations are related to 6 % vol. of O_2 in dry flue gas.

For the SNCR method:

- NSR values from 0.55 to 3.47,
- application of primary measures (flue gas recirculation and air staging),
- temperature for reducing agent injection from 880 to 950 °C,
- the average time in one setting was 45 min.

For the SCR method:

- NSR values from 0.29 to 1.6,
- application of primary measures (flue gas recirculation),
- catalyst temperatures from 259 to 299 °C,
- the average time in one setting was 74 min.

Individual states were set maintaining a constant temperature while the injection of the reducing agent was gradually changed. The urea solution was chosen

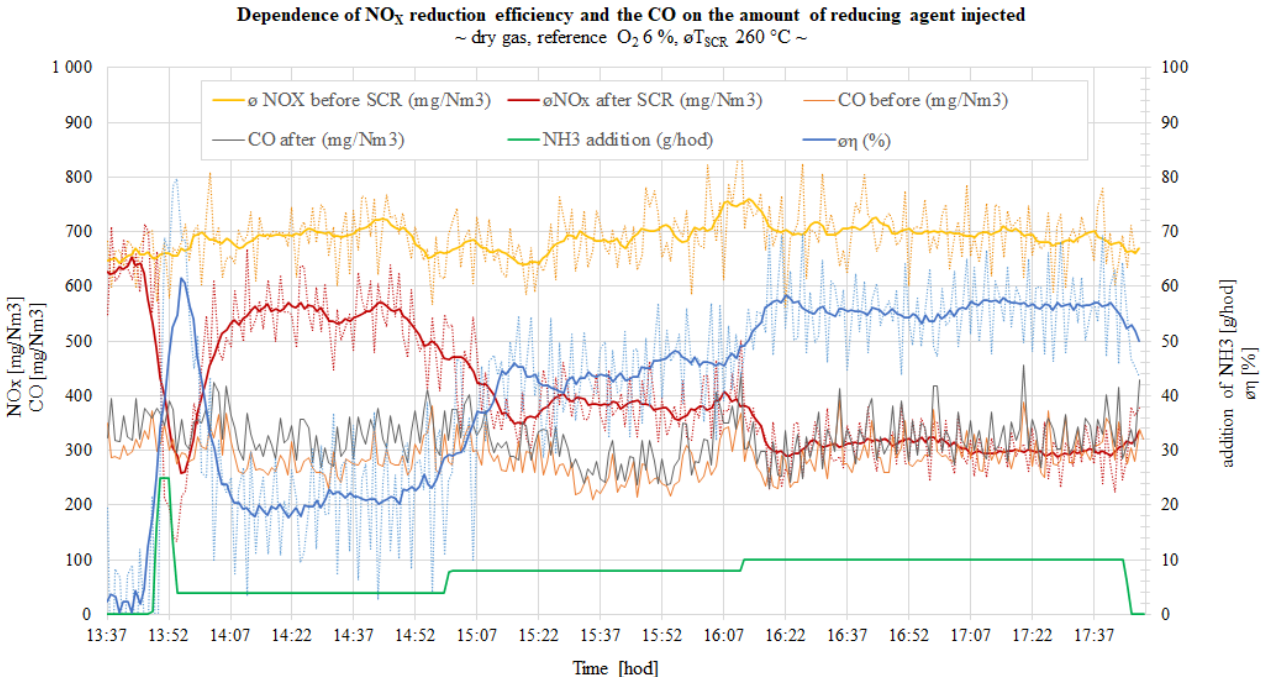

FIGURE 3. Summarization of the experimental results for SCR and SNCR.

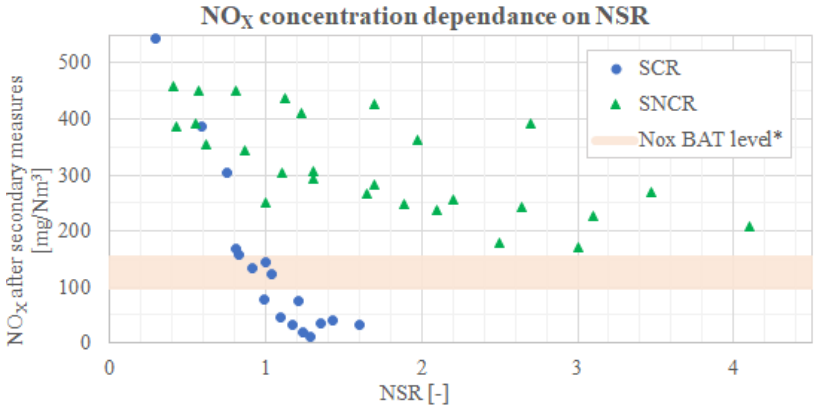

FIGURE 4. Achievable NOX level for SCR and SNCR methods in NSR for the same BFB boiler. *BAT-AELs (mg/Nm^3) for NO_X emissions from combustion of black and/or brown coal into the atmosphere for the new combustion plants with the total rated thermal output < 100 MWth of 100–150 mg/m$_N^3$ [23].

for the SNCR due to the properties of ammonia, which has very strict storage rules, and therefore is not used in large industrial plants for the SNCR method. Nevertheless, the fundamental reaction scheme for SCR and SNCR and both used reagents remains similar. Furthermore, the experiments performed are closer to the practical results due to the size of the experimental boiler.

4. Results and discussion

Measured data are presented in Table 3 and Figure 4. More detailed data with their variations are listed in Appendix.

The CO emissions were also measured, however, no significant correlation between CO and NO_X was observed as can be seen in Figure 3.

4.1. Reducing agent excess

As shown in Figure 4, there is a significant difference between the excess of reducing agent needed to achieve the same NO_X reduction efficiency for the SCR and SNCR denitrification methods. As can be seen from Figure 4, the experiments confirmed that for SCR, a lower excess of the reducing agent is needed to reach the same NO_X level after the secondary denitrification method because the catalyst reduces the activation energy of the chemical process.

According to [24], the reducing agent stoichiometry for SNCR has the optimum values between 1.5–2.5. Experiments showed the highest efficiency values when using NSR around 2.5, but it is always necessary to monitor the ammonia slip in the flue gas, which is subject to the BAT-associated emission level. According to BAT, the level of NH_3 emissions into the air from

Measurement no.	Temperature	NO_X before SNCR	NO_X after SNCR	NO_X conversion	NSR	NH_3 slip
	[°C]	[mg/Nm^3]	[mg/Nm^3]	[%]	[mol/mol]	[mg/Nm3]
1	959	321	250	22.1	1.00	not measured
2			238	26.0	2.10	
3			228	29.0	3.10	
4			209	35.1	4.10	
5	883	459	392	14.7	0.55	
6			303	34.1	1.10	
7			267	41.9	1.65	
8			257	43.9	2.20	
9			242	47.2	2.64	
10	886	408	356	12.9	0.62	
11			293	28.2	1.30	
12			249	39.0	1.89	
13			179	56.3	2.50	
14			170	58.4	3.00	
15	868	424	388	8.7	0.43	0.3
16			343	19.2	0.87	0.2
17			306	28.0	1.30	0.1
18			284	33.0	1.70	0.2
19			269	36.7	3.47	0.4
20	948	461	450	2.3	0.57	0.0
21			437	5.2	1.12	0.0
22			426	7.7	1.70	0.0
23			393	14.7	2.70	0.8
24	925	498	458	8.0	0.41	0.1
25			450	9.5	0.81	0.0
26			410	17.7	1.23	0.0
27			364	26.9	1.97	0.3
Measurement no.	**Temperature**	**NO_X before SCR**	**NO_X after SCR**	**NO_X conversion**	**NSR**	**NH_3 slip**
	[°C]	[mg/Nm^3]	[mg/Nm^3]	[%]	[mol/mol]	[mg/Nm3]
1	260	692	544	21.0	0.29	0
2		705	386	45.0	0.59	0
3		698	305	56.0	0.75	0
4		593	132	77.6	0.91	0
5		533	31	94.1	1.17	0.1
6		613	12	98.0	1.29	0.9
7	290	518	168	67.4	0.81	0.2
8		519	158	71.1	0.83	0.3
9		504	79	85.2	0.99	0.2
10		528	124	76.7	1.04	0.2
11		487	47	90.4	1.09	0.2
12		477	18	96.2	1.28	0.3
13		486	36	93.0	1.35	0.0
14	300	520	144	72.4	1.00	0.1
15		531	75	85.9	1.21	0.1
16		519	40	92.3	1.43	0.1
17		539	31	94.1	1.60	0.1

Table 3. Summarization of the experimental results for SCR and SNCR.

the use of SCR and/or SNCR is < 3–10 mg/m_N^3 [1]. In the case of plants that burn biomass and operate at variable loads, the upper end of the BAT-AEL range is 15 mg/m_N^3 [1]. Some of the unreacted ammonia is converted to ammonia salts and bound to fly ash, which then exhibits an unwanted odour and could become unapplicable in future use. In addition, leachable ammonia salts can restrict its application as well. Stricter requirements are therefore required by fly ash buyers who use it in the construction industry. Therefore, large combustion sources require values as low as 7 mg/m_N^3 for NH_3 in the flue gas after ESP, although ammonia can be smelled already at values of 5 mg/m_N^3. For these reasons, the feeding of higher amounts of the reducing agent and thus a higher NSR is not desirable.

The NO_X reduction efficiency of more than 90 % can be reached with the NSR greater than 1.1 for the SCR method. Further increase in the reducing agent feed is not desirable because the catalyst would be supersaturated and excess unreacted ammonia would escape along with the flue gas, causing the above-mentioned problems with the ash utilisation. In general, the SCNR method requires higher doses of the reducing agent for the same NO_X level required in the flue gas.

4.2. SCR and SNCR efficiency

The NO_X reduction efficiency varied between 2 % and 58 % for the SNCR method and between 21 % and 98 % for the SCR method. The lower value corresponds to the lowest injection rate of the reducing agent for both methods. For the SNCR method, the best results were achieved for temperatures between 880 and 890 °C and NSR between 2.2 and 3.0 when efficiency reached 44 to 58 %. For the SCR method, efficiencies higher than 90 % were reached for all catalyst temperatures, while the NSR's were between 1.1 and 1.6. The results agree with the BAT conclusions as stated in Section 1. From Table 2, it can be seen that the primary measures reduce the input NO_X concentrations for the SNCR method to values between 321 and 498 mg/Nm^3. The primary measures on this boiler are used mainly to increase the temperature in the freeboard section and thus to ensure that the optimum temperatures for NO_X reduction are reached. The SCR method was tested with flue gas recirculation (in order not to lower NO_X emission but to keep the combustion process stable) and the initial NO_X concentrations ranged between 477 and 705 mg/Nm^3. The nitrogen emissions concentrations after the denitrification measures were between 170 and 458 mg/Nm^3 for the SNCR method and between 12 and 544 mg/Nm^3 for the SCR method (the highest value is for an insufficiently low NSR of 0.3).

4.3. SCR and SNCR efficiency correlation with temperature

There is a clear effect of temperature on the SNCR method at the feeding point of the reducing agent. In Figure 5, it can be seen that higher efficiencies are achieved at temperatures up to about 900 °C, and with increasing temperature, the efficiency decreases at the same NSRs. This corresponds to the theoretical knowledge as mentioned in Section 2.2.2, where the optimal temperature window for urea is said to be between 850 and 1000 °C.

In contrast, in the case of the SCR method, the correlation with temperature is minimal and the efficiency basically depends only on the NSR, as shown in Figure 6.

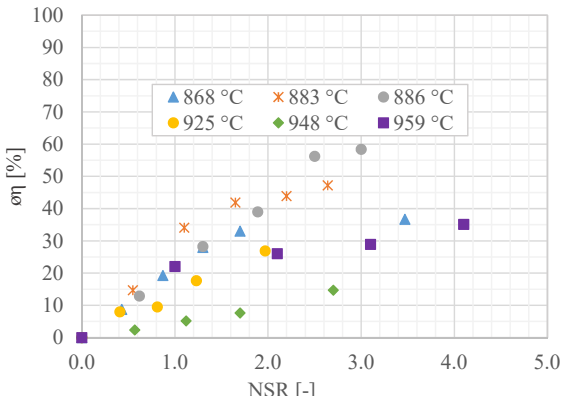

Figure 5. Correlation of SNCR efficiency and temperature.

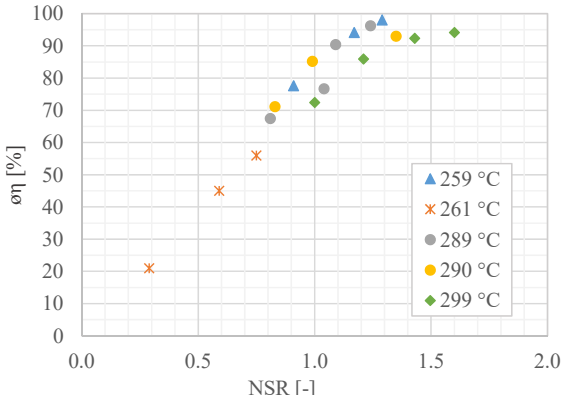

Figure 6. Correlation of SCR efficiency and temperature.

4.4. SCR and SNCR comparison for the same NO_X input concentrations

A specific comparison was made for the same NO_X input concentrations. The inlet nitrogen oxides concentration was kept at 500 mg/Nm^3, and no primary measures were used with the purpose of lowering nitrogen oxides levels. Different NSRs were used and the trend of NO_X reduction according to the NSR can be seen in Figure 7.

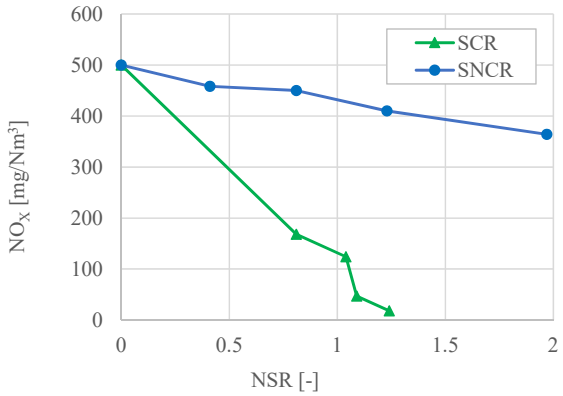

Figure 7. Comparison of the SCR and SNCR methods used within the same BFB boiler.

The maximum NSR for the SNCR method was 1.97. From other experimental results, we can assume that with a greater injection of the reducing agent and a lower temperature of the fluidized bed, lower nitrogen emissions could be achieved. In general, from the results it can be seen that a lower excess of the reducing agent is needed for the SCR method. The decision of whether to use the SCR or SNCR denitrification method depends on the final required level of nitrogen oxides and on the consideration of investment and operating costs.

5. Conclusions

The experimental results show the denitrification possibilities applied on the fluidized bed boiler with a thermal output of 500 kW. The size of the experimental equipment is the biggest benefit of performed experiments. The combustion of various fuel types and the generation of emissions have already been investigated, but those are mainly experimental reactors with a diameter of 100–150 mm and laboratory-made flue gas mixtures [16, 25]. Initial NO_X concentrations in the experimental boiler with lignite combustion range from 321 mg/Nm^3 to 705 mg/Nm^3.

The correlation of the denitrification efficiency and the NSR was investigated. It has been found that the SCR needs a lower NSR than the SNCR method to reach the same efficiency. The lower need for the reducing agent corresponds to the higher efficiency of the method because the catalyst reduces the activation energy of the reaction. In particular, NSR up to 1.6 was used for the SCR method. With higher NSRs, the ammonia slip could become too high and the ash could be degraded in the practical use of High-Dust catalysts. In contrast, the SNCR method has a higher reducing agent consumption and the best denitrification results were achieved for NSR around 2.5.

For the efficiency of both denitrification methods, the results are as follows. The SNCR method, together with primary measures (flue gas recirculation and air staging), reaches the efficiency of 58 % and the efficiency of the SCR method exceeds 98 %.

Acknowledgements

This work was supported by the project from Research Center for Low-Carbon Energy Technologies, CZ.02.1.01/0.0/0.0/16_019/0000753 which is gratefully acknowledged.

List of symbols

BAT best available techniques
CTU Czech Technical University
FT-IR Fourier transform infrared spectroscopy
LCP large combustion plants
MoO_3 molybdenum trioxide
NDIR non-dispersive infrared
NH_3 ammonia
NSR normalized stoichiometric ratio
NO nitric oxide
NO_X oxide emissions
NO_2 nitrogen dioxide
N_2O nitrous oxide
SCR selective catalytic reduction
SNCR selective non-catalytic reduction
TiO_2 titanium dioxide
V_2O_5 vanadium pentoxide
WO_3 tungsten trioxide

References

[1] T. Lecomte, J. Ferrería de la Fuente, F. Neuwahl, et al. *Best Available Techniques (BAT) reference document for large combustion plants*. EUR 28836 EN. Publications Office of the European Union, 2017. https://doi.org/10.2760/949.

[2] J. Vejvoda, P. Machač, P. Buryan. *Technologie ochrany ovzduší a čištění odpadních plynů*. University of Chemistry and Technology, 2003. ISBN 80-708-0517-X.

[3] F. Normann, K. Andersson, B. Leckner, F. Johnsson. Emission control of nitrogen oxides in the oxy-fuel process. *Progress in Energy and Combustion Science* **35**(5):385–397, 2009. https://doi.org/10.1016/j.pecs.2009.04.002.

[4] C. T. Bowman. Control of combustion-generated nitrogen oxide emissions: Technology driven by regulation. *Symposium (International) on Combustion* **24**(1):859–878, 1992. https://doi.org/10.1016/S0082-0784(06)80104-9.

[5] J. Hemerka, P. Vybíral. *Ochrana ovzduší*. Czech Technical University in Prague, 2010. ISBN 978-80-01-04646-3.

[6] P. Machač, E. Baraj. A simplified simulation of the reaction mechanism of NO_x formation and non-catalytic reduction. *Combustion Science and Technology* **190**(6):967–982, 2018. https://doi.org/10.1080/00102202.2017.1418335.

[7] P. Forzatti. Present status and perspectives in de-NO_x SCR catalysis. *Applied Catalysis A: General* **222**(1-2):221–236, 2001. https://doi.org/10.1016/S0926-860X(01)00832-8.

[8] K. El Sheikh, M. J. H. Khan, M. Diana Hamid, et al. Advances in reduction of NO_x and N_2O_1 emission formation in an oxy-fired fluidized bed boiler. *Chinese Journal of Chemical Engineering* **27**(2):426–443, 2019. https://doi.org/10.1016/j.cjche.2018.06.033.

[9] IPCC, 2007. *Climate Change 2007: Synthesis Report. Contribution of Working Groups I, II and III to the Fourth Assessment Report of the Intergovernmental Panel on Climate Change [Core Writing Team and Pachauri, R.K. and Reisinger, A. (eds.)].* IPCC, Geneva, Switzerland, 2007. ISBN 92-9169-122-4.

[10] L. E. Aamand, B. Leckner, S. Andersson. Formation of nitrous oxide in circulating fluidized-bed boilers. *Energy & Fuels* **5**(6):815–823, 1991. https://doi.org/10.1021/ef00030a008.

[11] M. de las Obras-Loscertales, T. Mendiara, A. Rufas, et al. NO and N_2O emissions in oxy-fuel combustion of coal in a bubbling fluidized bed combustor. *Fuel* **150**:146–153, 2015. https://doi.org/10.1016/j.fuel.2015.02.023.

[12] M. Vodička, J. Hrdlička, P. Skopec. Experimental study of the NO_X reduction through the staged oxygen supply in the oxy-fuel combustion in a 30 kW_{th} bubbling fluidized bed. *Fuel* **286**:119343, 2021. https://doi.org/10.1016/j.fuel.2020.119343.

[13] C. Lupiáñez, L. I. Díez, L. M. Romeo. Influence of gas-staging on pollutant emissions from fluidized bed oxy-firing. *Chemical Engineering Journal* **256**:380–389, 2014. https://doi.org/10.1016/j.cej.2014.07.011.

[14] M. de las Obras-Loscertales, A. Rufas, L. de Diego, et al. Effects of temperature and flue gas recycle on the SO_2 and NO_x emissions in an oxy-fuel fluidized bed combustor. *Energy Procedia* **37**:1275–1282, 2013. https://doi.org/10.1016/j.egypro.2013.06.002.

[15] T. Czakiert, Z. Bis, W. Muskala, W. Nowak. Fuel conversion from oxy-fuel combustion in a circulating fluidized bed. *Fuel Processing Technology* **87**(6):531–538, 2006. https://doi.org/10.1016/j.fuproc.2005.12.003.

[16] W. Moroń, W. Rybak. NO_x and SO_2 emissions of coals, biomass and their blends under different oxy-fuel atmospheres. *Atmospheric Environment* **116**:65–71, 2015. https://doi.org/10.1016/j.atmosenv.2015.06.013.

[17] X. Cheng, X. T. Bi. A review of recent advances in selective catalytic NO_x reduction reactor technologies. *Particuology* **16**:1–18, 2014. https://doi.org/10.1016/j.partic.2014.01.006.

[18] F. Gholami, M. Tomas, Z. Gholami, M. Vakili. Technologies for the nitrogen oxides reduction from flue gas: A review. *Science of The Total Environment* **714**:136712, 2020. https://doi.org/10.1016/j.scitotenv.2020.136712.

[19] Y. GAO, T. LUAN, T. LÜ, et al. Performance of $V_2O_5-WO_3-MoO_3/TiO_2$ catalyst for selective catalytic reduction of NO_x by NH_3. *Chinese Journal of Chemical Engineering* **21**(1):1–7, 2013. https://doi.org/10.1016/S1004-9541(13)60434-6.

[20] L. Olsson, H. Sjövall, R. J. Blint. A kinetic model for ammonia selective catalytic reduction over $Cu-ZSM-_5$. *Applied Catalysis B: Environmental* **81**(3-4):203–217, 2008. https://doi.org/10.1016/j.apcatb.2007.12.011.

[21] J. Hrdlicka, P. Skopec, F. Hrdlicka. Trough air distributor for a bubbling fluidized bed boiler with isobaric nozzles. In *Proceedings of the 22nd International Conference on Fluidized Bed Conversion*, vol. 1. Turku, Finland, 2015. ISBN 978-952-12-3222-0.

[22] P. Skopec, J. Hrdlička, J. Opatřil, J. Štefanica. NO_X emissions from bubbling fluidized bed combustion of lignite coal. *Acta Polytechnica* **55**(4):275–281, 2015. https://doi.org/10.14311/AP.2015.55.0275.

[23] Prováděcí rozhodnutí komise (EU) 2021/2326. *Úřední věstník Evropské unie* **L 469**:1–81, 2021. https://eur-lex.europa.eu/legal-content/CS/TXT/PDF/?uri=CELEX:32021D2326&from=EN.

[24] M. Mladenović, M. Paprika, A. Marinković. Denitrification techniques for biomass combustion. *Renewable and Sustainable Energy Reviews* **82**:3350–3364, 2018. https://doi.org/10.1016/j.rser.2017.10.054.

[25] Y. Hu, S. Naito, N. Kobayashi, M. Hasatani. CO_2, NO_x and SO_2 emissions from the combustion of coal with high oxygen concentration gases. *Fuel* **79**(15):1925–1932, 2000. https://doi.org/10.1016/S0016-2361(00)00047-8.

A. Appendix

SNCR							
Measurement no.	**Temperature**	**NO_X before SNCR**	**NO_X after SNCR**	**NO_X conversion**	**NSR**	**O_2**	**NH_3 slip**
	[°C]	[mg/Nm^3]	[mg/Nm^3]	[%]	[mol/mol]	[%]	[mg/Nm^3]
1	959 ± 5	321 ± 31	250 ± 12	22.1 ± 2.3	1.00	5.0 ± 0.2	not measured
2			238 ± 9	26.0 ± 1.0	2.10	6.5 ± 0.7	
3			228 ± 14	29.0 ± 0.8	3.10	7.1 ± 0.2	
4			209 ± 9	35.1 ± 1.7	4.10	6.6 ± 0.2	
5	883 ± 10	459 ± 29	392 ± 33	14.7 ± 7.2	0.55	6.9 ± 0.6	
6			303 ± 14	34.1 ± 3.0	1.10	5.9 ± 0.3	
7			267 ± 15	41.9 ± 3.3	1.65	5.7 ± 0.3	
8			257 ± 14	43.9 ± 3.4	2.20	5.7 ± 0.3	
9			242 ± 10	47.2 ± 2.3	2.64	5.9 ± 0.3	
10	886 ± 8	408 ± 22	356 ± 25	12.9 ± 3.3	0.62	5.3 ± 0.4	
11			293 ± 29	28.2 ± 3.6	1.30	4.6 ± 0.4	
12			249 ± 23	39.0 ± 3.1	1.89	4.5 ± 0.4	
13			179 ± 37	56.3 ± 3.9	2.50	4.7 ± 0.7	
14			170 ± 11	58.4 ± 0.6	3.00	3.6 ± 0.3	
15	868 ± 20	424 ± 33	388 ± 25	8.7 ± 3.6	0.43	6.5 ± 0.8	0.3 ± 0.1
16			343 ± 19	19.2 ± 1.7	0.87	5.8 ± 0.5	0.2 ± 0.1
17			306 ± 15	28.0 ± 1.1	1.30	5.5 ± 0.6	0.1 ± 0.1
18			284 ± 13	33.0 ± 1.2	1.70	5.1 ± 0.4	0.2 ± 0.1
19			269 ± 22	36.7 ± 2.0	3.47	5.5 ± 0.5	0.4 ± 0.2
20	948 ± 29	461 ± 7	450 ± 22	2.3 ± 3.4	0.57	6.4 ± 0.5	0.0 ± 0.1
21			437 ± 38	5.2 ± 1.2	1.12	5.4 ± 1.8	0.0
22			426 ± 27	7.7 ± 2.1	1.70	4.3 ± 0.3	0.0
23			393 ± 12	14.7 ± 0.8	2.70	4.4 ± 0.4	0.8 ± 0.3
24	925 ± 11	498 ± 8	458 ± 12	8.0 ± 2.6	0.41	7.0 ± 0.3	0.1 ± 0.1
25			450 ± 8	9.5 ± 1.5	0.81	7.2 ± 0.3	0.0
26			410 ± 12	17.7 ± 2.6	1.23	7.2 ± 0.2	0.0
27			364 ± 43	26.9 ± 8.8	1.97	7.3 ± 0.8	0.3 ± 0.2

Table 4. Experimental results for SNCR.

SCR							
Measurement no.	**Temperature**	**NO_X before SCR**	**NO_X after SCR**	**NO_X conversion**	**NSR**	**O_2**	**NH_3 slip**
	[°C]	[mg/Nm^3]	[mg/Nm^3]	[%]	[mol/mol]	[%]	[mg/Nm^3]
1	260 ± 2	692 ± 74	544 ± 58	21.0 ± 9.9	0.29 ± 0.02	10.1 ± 0.5	0
2		705 ± 60	386 ± 46	45.0 ± 7.3	0.59 ± 0.03	10.5 ± 0.9	0
3		698 ± 50	305 ± 38	56.0 ± 6.5	0.75 ± 0.03	10.6 ± 0.7	0
4		593 ± 54	132 ± 20	77.6 ± 3.0	0.91 ± 0.07	9.8 ± 0.7	0
5		533 ± 70	31 ± 15	94.1 ± 2.5	1.17 ± 0.12	9.7 ± 0.8	0.1 ± 0.2
6		613 ± 73	12 ± 4	98.0 ± 0.9	1.29 ± 0.09	10.5 ± 0.9	0.9 ± 0.2
7	290 ± 1	518 ± 40	168 ± 24	67.4 ± 4.3	0.81 ± 0.06	9.8 ± 0.6	0.2 ± 0.1
8		519 ± 19	158 ± 11	71.1 ± 1.8	0.83 ± 0.04	9.5 ± 0.5	0.3 ± 0.1
9		504 ± 19	79 ± 9	85.2 ± 1.7	0.99 ± 0.05	9.3 ± 0.5	0.2 ± 0.1
10		528 ± 45	124 ± 24	76.7 ± 3.6	1.04 ± 0.15	10.7 ± 1.4	0.2 ± 0.1
11		487 ± 28	47 ± 9	90.4 ± 1.9	1.09 ± 0.06	8.4 ± 0.4	0.2 ± 0.1
12		477 ± 46	18 ± 7	96.2 ± 1.4	1.28 ± 0.10	8.4 ± 0.6	0.3 ± 0.1
13		486 ± 18	36 ± 8	93.0 ± 1.6	1.35 ± 0.05	9.0 ± 0.5	0.0 ± 0.1
14	300 ± 1	520 ± 37	144 ± 17	0.4 ± 2.4	1.00 ± 0.06	9.2 ± 0.5	0.1 ± 0.1
15		531 ± 15	75 ± 5	85.9 ± 1.0	1.21 ± 0.06	9.4 ± 0.2	0.1 ± 0.1
16		519 ± 15	40 ± 7	92.3 ± 1.2	1.43 ± 0.07	9.3 ± 0.4	0.1 ± 0.1
17		539 ± 30	31 ± 6	94.1 ± 1.2	1.60 ± 0.09	9.5 ± 0.4	0.1 ± 0.1

TABLE 5. Experimental results for SCR.

THEORETICAL AND EXPERIMENTAL STUDY OF WATER VAPOUR CONDENSATION WITH HIGH CONTENT OF NON-CONDENSABLE GAS IN A VERTICAL TUBE

Jakub Krempaský*, Jan Havlík, Tomáš Dlouhý

Czech Technical University in Prague, Faculty of Mechanical Engineering, Department of Energy Engineering, Technická 4, Prague 6 16607, Czech Republic

* corresponding author: jakub.krempasky@fs.cvut.cz

Abstract. This article deals with the possibility of separating water vapour from flue gases after oxyfuel combustion using condensation processes. Those processes can generally be described as condensation of water vapour in the presence of non-condensable gases. Hence, the effect of non-condensable gas (NCG) on the condensation process has been theoretically and experimentally analysed in this study. The theoretical model was developed on the basis of the heat and mass transfer analogy with respect to the effect of the NCG, the flow mode of the condensate film, the shear stress of the flowing mixture, subcooling and superheating. Subsequently, an experimental analysis was carried out on a 1.5 m long vertical pipe with an inner diameter of 23.7 mm. The mixture of vapour and air flowed inside the inner tube with an air mass fraction ranging from 23 % to 62 %. The overall heat transfer coefficients (HTC) from the theoretical model and experimental measurement are significantly lower than the HTC obtained according to the Nusselt theory for the condensation of pure water vapour. The overall HTC decreases along the tube length as the gas concentration increases, which corresponds to a decrease in the local condensation rate. The highest values of the HTC are observed in the condenser inlet, although a strong decrease in HTC is also observed here. Meanwhile, there is a possibility for an HTC enhancement through turbulence increase of the condensing mixture in the condenser outlet. Results also showed that the heat resistance of the mixture is several times higher than the heat resistance of the condensate film. The developed theoretical model based on heat and mass transfer analogy is in good agreement with experimental results with the standard deviation within +25 % and −5 %. The model is more accurate for lower NCG concentrations.

Keywords: Condensation, non-condensable gas, vertical tube, experimental, theoretical.

1. Introduction

One of the promising CCS technologies is oxyfuel combustion. The use of CO_2 captured from oxyfuel combustion technology for other technological purposes and for storage requires a sufficient purity of the product. After emissions cleaning, suitable options for final drying of flue gases are condensation processes in condensing heat exchangers. The aim is to dry the flue gas formed by oxyfuel combustion, which is consists of steam and a high proportion of non-condensing gases (especially CO_2 and O_2). The drying is necessary for the final purification of CO2 prior to its further use. This process can generally be described as the condensation of water vapour with a high content of non-condensable gases.

Condensation of water vapour with the presence of non-condensable gas (e.g. CO_2) is a widely studied topic and its recognition dates back to 1873 [1]. Up to now, the main focus has been on condensation of water vapour with a small fraction of air in tube condensers [2, 3]. Such cases can be found in various technological processes such as refrigeration, condensers in power plants, geothermal power plants and various processes in chemical and process industry. This field of study has been investigated by many authors and, today, represents a well-covered topic. However, there are areas where the content of air during the vapour condensation can be higher or different gas than air is present. For instance, it can be: CCU/S technologies, desalination of water, latent heat recovery from flue gas or LOCA accidents [2–4]. Therefore, studying condensation in tube condensers with respect to new technological challenges has a potential for commercial applications and system improvement.

Chantana [5] conducted an experimental and theoretical study of water vapour condensation in the presence of air in a vertical tube. The water vapour content in the gas vapour mixture was very low. The theoretical model was developed on the basis of the heat and mass transfer analogy. The results showed that the condensation of the vapour and roughness of the film surface cause a disruption of the gas layer accumulated near the phase interface, which increases the HTC. A detailed description of the processes at the vapour-liquid interface is also introduced in [6, 7]. Maheswari [8], in his work, studied the influence of the water vapour and air mixture's Reynolds number on the HTC in a vertical tube. He concluded that the

Method	Semi-theoretical		Theoretical	
	Correction and degradation factor	**Heat and mass transfer analogy**	**Diffusion layer model**	**Boundary layer model**
Description	Empirical equations based on experimental data.	Based on similarities between momentum, energy, heat, and mass transfer equations and empirical coefficients.	Based on Fick's law of molecular diffusion. Vapour diffuses through the layer of non-condensable gas to phase interphase.	Description of condensate film layer and boundary layer with initial and boundary conditions.
Accuracy and output	Low accuracy, simple output.	Moderately high accuracy, usually iteration involved.	Moderately high accuracy, usually iteration involved.	High accuracy, various results, too complex for practical application.

TABLE 1. Overview of theoretical models for film-wise condensation with non-condensable gas.

HTC of the film can be lower than the HTC of the mixture in the case of high Reynolds number of the mixture. No and Park [9] conducted experiments in vertical and horizontal tubes. The most important observation was that the waviness of the film decreases the accumulation of gas near the phase interface, and thereby effectively increases heat transfer. The effect of gas velocity on the flow of the liquid film in the vertical tube is also studied in the work of the Kracik [10], where the effect of shear stress of the flowing gas on the liquid film is analysed experimentally and theoretically with three different diameters of the inner tube. Kuhn [11] created three theoretical models developed on degradation factor, heat and mass transfer analogy, and mass transfer modelling and compared them with results from an experimental measurement. The standard deviations of the HTC were 6.4 %, 8.4 % and 17.6 % for water vapour with air and 3.2 %, 6.1 % and 17.6 % for water vapour with helium according to the mass transfer modelling, diffusion layer modelling and degradation factor, respectively.

This article focuses on research of the process of condensation of water vapour from flue gases from oxyfuel combustion. In this study, the effect of non-condensable gas (NCG) on vapour condensation in a vertical tube condenser is theoretically and experimentally analysed.

2. Theoretical modelling

2.1. Summary of available theoretical models

There are several methods to calculate heat transfer during the condensation of water vapour in the presence of NCG in a vertical tube. In general, theoretical models for such phenomena are governed by the film condensation model, which was first described by Nusselt in 1916 [12]. Theoretical models based on the theory of film-wise condensation are usually divided into two groups, semi-theoretical and theoretical. Semi-theoretical models use, to some extent, experimentally established coefficients and data, which are incorporated into the theoretical analysis. The first option is correction and degradation factors, which modify the standard theory for the condensation of pure vapour. The second option is models based on heat and mass transfer analogy. Meanwhile, theoretical models are not based on experimental data, but on the description of the boundary layer near the phase interphase. The general summary of the theoretical models is shown in Table 1 [3, 11, 13]. The degradation factor is the simplest method for the determination of HTC; however, it gives less accurate results. While the theoretical models are quite complex and can give very accurate results, their practical use is quite complicated.

2.2. Developed theoretical model

A theoretical model based on the heat and mass transfer analogy was developed for a vertical double-pipe condenser in which the condensing water vapour flows downwards in the inner tube and the cooling water flows in counter-current in the outer tube. Detailed descriptions of semi-theoretical models based on heat and mass transfer analogy can be found in the literature [5, 14, 15]. Herein, the condenser was divided into 15 segments where local heat transfer was determined. The overall HTC in the condenser is given by the heat transfer coefficients of several layers as shown in Figure 1 and described with Equation (1). One segment is shown in Figure 2.

Heat transfer of the condenser can be determined by a temperature difference and a corresponding HTC of the certain layer. The overall condenser power can be calculated from the temperature difference of bulk mixture temperature T_{SAT} and cooling water temperature T_K with the overall HTC of the condenser K. The heat transfer from the condensing mixture to the phase interface is given by the temperature difference of the bulk mixture T_{SAT} and phase interface $T_{F,SAT}$ and HTC of condensing mixture $\ddot{\alpha_G}$. This is equal

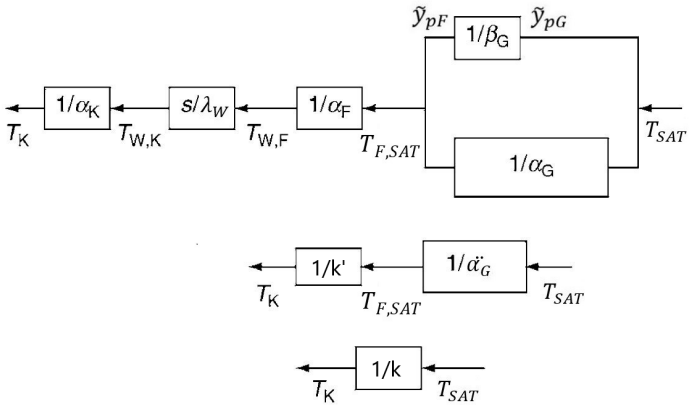

FIGURE 1. Heat and mass resistances during condensation [14].

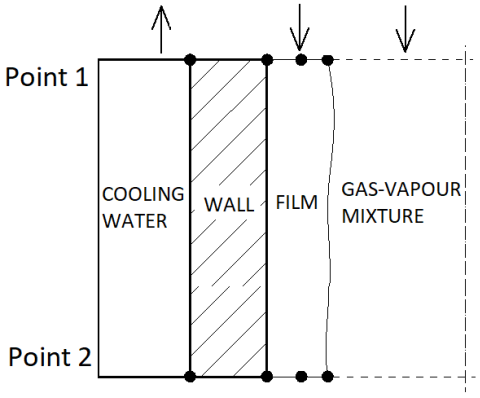

FIGURE 2. Analytical model.

to the heat transfer from the phase interface with temperature $T_{F,SAT}$ to the coolant flow with temperature T_K with corresponding HTC k'. Two dots in HTC of condensing mixture $\ddot{\alpha_G}$ indicates that heat is transferred not only by conduction which is given by α_G but also by mass flow of condensing vapour, which is given by mass transfer coefficient β_G.

The heat flux between the gas-vapour mixture and the cooling water is determined by the heat and mass transfer resistances and the temperature difference of the fluids in the condenser.

$$\begin{aligned}\dot{q} &= \ddot{\alpha}_G(T_{SAT} - T_{F,SAT}) \\ &= k'(T_{F,SAT} - T_K) \\ &= k(T_{SAT} - T_K)\end{aligned} \tag{1}$$

The fundamental assumption in the model is that the condensate flows on a vertical wall in an annular film, similarly to the Nusselt condensation theory with HTC α_F. The vapour condenses on the film surface, while the gas accumulates near the phase interface. This forms another layer of non-condensable gas through which the vapour diffuses towards the phase interface. Heat flux, which is transferred from the gas-vapour mixture, can be divided into sensible heat given by HTC α_{cv} and latent heat given by α_c, as described by Equation (2). The mass transfer resistance occurs only in the mixture since the condensate film is formed only by water with a temperature at the wall $T_{W,F}$.

$$\dot{q} = \frac{1}{\dfrac{1}{\alpha_F} + \dfrac{1}{\alpha_{cv} + \alpha_c}}(T_{SAT} - T_{W,F}) \tag{2}$$

The convective heat flow $\dot{q}_G$ transferred from the gas to the liquid film is calculated with respect to the mass transfer that occurs with heat transfer according to the Ackermann correction factor E_T (Equation (3)) with Equation (4) and Equation (5), where Φ_T is a non-dimensional mass flow, $\dot{n}$ local molar flux, $\tilde{c}_{pG}$ molar specific heat capacity and α_G convective HTC of the mixture.

$$\dot{q} = \alpha_G E_T(T_{SAT} - T_{F,SAT}) \tag{3}$$

$$E_T = \frac{\Phi_T}{1 - \exp(-\Phi_T)} \tag{4}$$

$$\Phi_T = \frac{\dot{n}\tilde{c}_{pG}}{\alpha_G} \tag{5}$$

The latent heat corresponds to the vapour transferred through the gas layer to the phase interface. This can be determined by applying the heat and mass transfer analogy. Mass transfer is based on the same formal relation as heat transfer replacing the Nusselt number Nu with the Sherwood number Sh and the Prandtl number Pr with the Schmidt number Sc as shown in Equations (6) and (7). The relation between mass and heat transfer can then be described by the Lewis number Le according to Equation (8) with molar density of the gas n_G. The mass transfer coefficient is then applied to calculate the local condensing flow according to the diffusion of concentration (Equation (9)) where $\dot{r}_v$ is the relative molar flow of the vapour, $\widetilde{y}_{v,F}$ is the molar concentration of vapour at the phase interface, $\widetilde{y}_{v,B}$ is the molar concentration of vapour in the bulk mixture, and $\dot{n}_v$ is the local vapour molar flux.

$$Nu = CRe^{\alpha}Pr^{0.6} \tag{6}$$

$$Sh = CRe^{\alpha}Sc^{0.6} \tag{7}$$

$$\alpha_G = n_G\beta_G\tilde{c}_{pG}Le^{0.6} \tag{8}$$

$$\dot{n} = n_G\beta_G \ln\left(\frac{\dot{r}_v - \tilde{y}_{v,F}}{\dot{r}_v - \tilde{y}_{v,B}}\right), \tag{9}$$

where:

$$\dot{r}_v = \frac{\dot{n}_v}{\dot{n}}. \tag{10}$$

During the calculation of the heat balance at certain parts of the condenser, it is necessary to know the condensation temperature of the vapour on the phase interface $T_{F,SAT}$. This temperature is calculated from Equation (10), including mass and energy balance. This equation is solved iteratively with the initial estimation of the film temperature at the phase

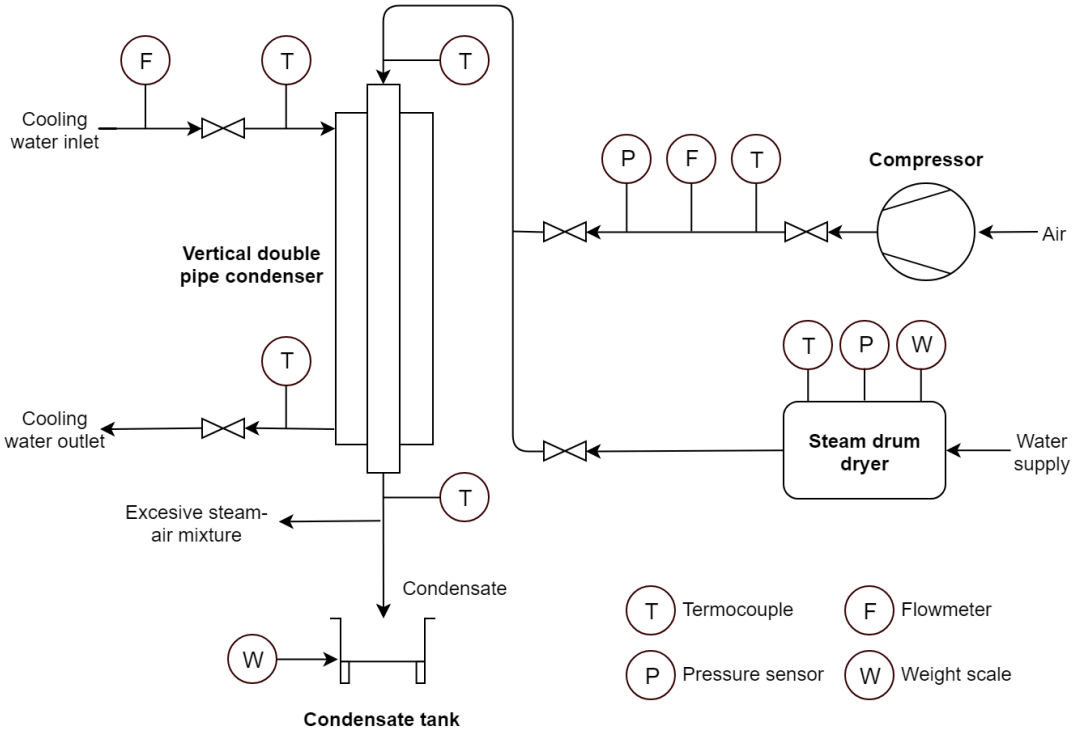

FIGURE 3. Schematic diagram of experimental setup.

interface with $\dot{N}_F$ being the film molar flux and T_F being the film temperature.

$$\dot{N}_F \tilde{c}_{pF} \frac{dT_F}{dA} + k'(T_{SAT} - T_{F,SAT}) = \dot{n}\Delta\tilde{h}_v + \alpha_G E_T (T_{SAT} - T_{F,SAT}) \quad (11)$$

Overall results are given by an arithmetic ratio of results from given segments. The overall condensation performance of the heat exchanger is calculated according to the steps shown below. Two parameters must be estimated at the beginning – the condensation temperature of the vapour on the film surface and the outlet temperature of the cooling water. The temperature of the film surface has to be estimated in each segment, while the temperature of the cooling water has to be estimated only in the outlet segment. The temperature of the cooling water at other points is given by the energy balance corresponding to the condensation and convection of the air-vapour mixture in the given segment. The HTC of the cooling water was experimentally determined by pure water vapour tests. The effects of the film flow mode, the shear stress of the flowing mixture, and the subcooling and superheating are included according to [14].

(1.) Input of initial values (mixture and cooling water inlet parameters – temperature, pressure, mass flow).

(2.) Estimation of the outlet temperature of cooling water.

(3.) Estimation of the saturation temperature at the phase interface of vapour.

(4.) Calculation of fluid thermodynamic properties according to [15].

(5.) Calculation of heat and mass transfer coefficients α_G; β_G.

(6.) Calculation of the local condensation rate and HTC of the film α_F.

(7.) Calculation of saturation temperature at the phase interface using the Ackermann correction factor.

(8.) Check if the calculated saturation temperature on the phase interface corresponds to the estimated (if not, back to step 3 – an adjustment of the saturation temperature on the phase interface is necessary).

(9.) Calculation of the condenser power, heat transfer coefficient, outlet cooling water temperature for a given segment.

(10.) Repeat the calculation from the beginning until the last segment is calculated.

(11.) Check if the calculated outlet temperature of the cooling water corresponds to the estimated temperature (if not, back to Step 2 – the adjustment of cooling water outlet temperature).

(12.) Results and average values.

3. Experimental apparatus

A schematic diagram of the experimental apparatus used for the theoretical model validation is shown in Figure 3. The system is designed as an open loop comprised of three parts: main test section; water

vapour and air supply section; cooling water section. The main test section comprises a vertical double-pipe heat exchanger made of two concentric stainless steel tubes. The mixture of water vapour and air enters the heat exchanger at the top and is directed vertically downwards through a calming section before flowing into the inner vertical tube. The cooling water flows upwards in the annulus. The heat exchanger is in counter-current configuration. The inner tube of the heat exchanger is 2000 mm long with an inner diameter of 23.7 mm and a wall thickness of 1.6 mm. The outer tube is 1500 mm long, with an inner diameter of 29.7 mm and a wall thickness of 2 mm. The tube material is stainless steel 1.4301 (AISI 304). The annulus created from these two concentric tubes is 1.6 mm in width. Stainless steel pins are used as spacers at three circumferential positions to keep the annulus concentric.

The steam generator was placed on the platform weight scale, which measured the amount of vapour generated. The generator produced steam steadily at a rate controlled by the power input to the electrical immersion heaters. In the first stage of the experiments, air was chosen as the NCG and blown in the mixing point by a compressor. The volume flow rate of air was measured by a rotameter. The pressure of the air was measured using a U-tube water manometer. The mixing chamber of water and air was designed so that any possible condensate occurring during the mixing of the vapour and air was flowing back to the steam generator. The flow rate of the cooling water was controlled by a regulating valve. Non-condensing gases in the water circuit were vented from the system through a manual gate valve at the exit of the condenser. Microfiber insulation and rubber foam were wrapped around the heat exchanger to prevent any potential heat loss. Four thermocouples were placed in condenser tapings measuring the inlet and outlet temperature of the cooling water and the inlet and outlet temperature of the water vapour-air mixture. All experiments were performed under atmospheric pressure. Measurements were conducted after the steady state of the system was reached.

4. Results and discussion

4.1. Theoretical analysis

The theoretical model was developed to predict the results from experimental measurements and analyse the condensation process. Six different air mass concentrations in the mixture were tested in the model, ranging from 23 % to 62 %. The condensation of the vapour – air mixture differs in several parameters as compared to condensation of pure vapour. As water vapour condenses along the condenser tube, the concentration of vapour in the mixture changes. Therefore, the HTC, the condensation rate, the saturation temperature, and most of the driving parameters change along the condense tube.

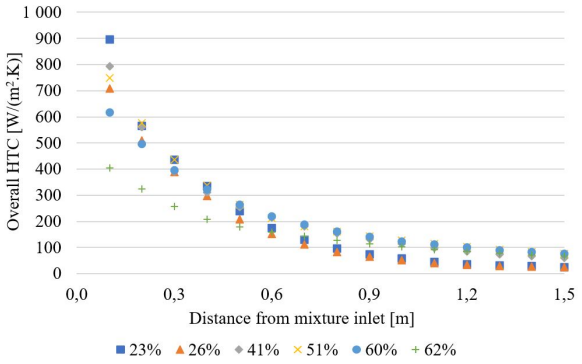

Figure 4. Overall HTC along condenser length.

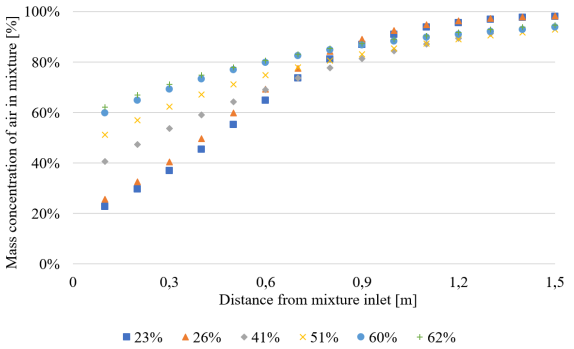

Figure 5. Air concentration in the mixture along condenser length.

The local HTC of the condenser along the tube length for all tests is shown in Figure 4. A rapid decrease in the HTC in the condenser inlet was calculated for the model for all cases of the condenser. As the vapour condenses along the condenser tube, several factors change, which leads to a reduction in vapour condensation and heat transfer; these factors are: increase of air concentration; decrease of velocity and Reynolds number of the mixture; increase of film thickness. As air concentration increases and the local condensation rate decreases, the overall HTC decreases rapidly in the condenser inlet. In the condenser outlet, HTC does not change so much since the local heat transfer is low and the amount of condensed vapour is also very small. Correspondingly, the HTC in the condenser outlet is very low because of the high concentration of air, which forms a gas layer next to the condensate film and prevents the vapour from reaching the phase interface. This can be seen in Figure 5, where the air concentration along the tube length is shown for all measurements. A strong increase in air concentration is observed at the beginning, and slow degradation is seen at the end as a result of a lower local condensation rate. The overall HTC of the condenser is determined by the heat resistance of certain parts of the condenser, as shown in Figure 2 and Equation (11), with the inner radius of the inner tube r_1, inner radius of the outer tube r_2, wall thermal conductivity λ_W, and HTC of the

			Tests					
			1	2	3	4	5	6
Air mass concentration	x	[-]	23 %	26 %	41 %	51 %	60 %	62 %
Air flow	$\dot{M}_a$	[kg/h]	0.58	0.58	1.37	2.04	2.63	2.04
Water vapour flow	$\dot{M}_p$	[kg/h]	1.97	1.68	2.01	1.94	1.77	1.24
Condensate flow	$\dot{M}_{KON}$	[kg/h]	1.98	1.68	1.87	1.58	1.16	-
Cooling water flow	$\dot{M}_K$	[kg/s]	0.0213	0.0213	0.0213	0.0165	0.0213	0.0281
Cooling water inlet temperature	T_{K1}	[°C]	14.8	14.8	14.7	15.0	14.6	16.0
Cooling water outlet temperature	T_{K2}	[°C]	32.0	29.2	30.8	30.4	25.8	22.2
Mixture inlet temperature	T_{p1}	[°C]	94.9	93.9	91.1	82.9	82.1	76.4
Mixture outlet temperature	T_{p2}	[°C]	43.6	40.6	74.6	66.5	64.6	61.3

TABLE 2. Measured values for all six tests.

cooling water $\propto_K$.

$$\frac{1}{r_1 k} = \frac{1}{r_1 \ddot{\propto}_G} + \frac{1}{r_1 \propto_F} + \frac{\ln \frac{r_2}{r_1}}{\lambda_W} + \frac{1}{r_2 \propto_K} \qquad (12)$$

Since the heat resistance of the cooling side and the tube wall of the condenser is quite low, the overall HTC is determined by the heat resistance of the condensing side. During the condensation of water vapour without non-condensing gases, the main heat resistance is usually formed by the condensate film on the cooling surface. This is quite well described by the Nusselt theory. In the case of the presence of NCG, the heat resistance is formed not only by the condensate film but also by the heat resistance of the mixture. The magnitude of heat resistance in the condensate film and the mixture depends on several parameters, mainly the concentration of air in the mixture, the flow of the condensate film, the flow of the mixture and the subcooling of the film. Due to the high amount of NCG in the mixture and low *Re* of the mixture, the heat resistance on the condensing side, in presented tests, was formed mainly by the heat resistance of the mixture. This can be seen in Figure 6 where the HTC of the film and the mixture are compared. The HTC of the condensate film is several times higher than the HTC of the mixture, therefore, the heat transfer is strongly affected by the heat and mass transfer in the gas-vapour mixture. Although the HTC of the film decreases along the condenser length as a result of the increase in film thickness, the HTC of the mixture is at least ten times lower and, in some cases, it is lower even more than two hundred times. This supports the claim that the HTC of the film can be neglected in some cases, since the overall HTC is formed mostly by the HTC of the mixture.

It can also be seen that it is quite difficult to fully condensate the vapour out of the mixture. Since the HTC decreases significantly at the end of the condenser, a very large condensation surface would be necessary to fully separate the vapour and the non-condensable gas. The initial gas concentration is not so crucial when the vapour must be fully condensed,

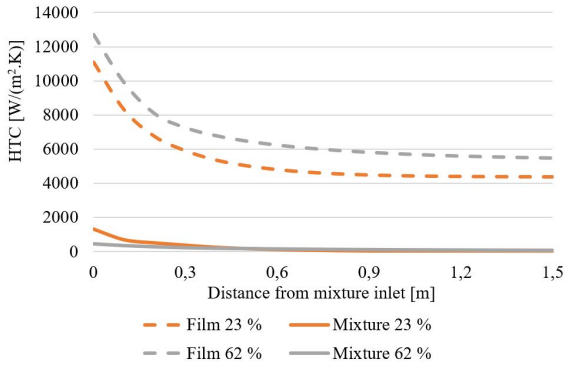

FIGURE 6. Comparison of HTC of film and gas – vapour mixture.

as the HTC is approaching similar parameters at the end of the condenser for all runs.

4.2. EXPERIMENTAL RESULTS

Experimental measurements with a mixture of water and air were conducted in the experimental loop with a vertical double-pipe condenser. The tests were carried out for six different air concentrations. The evaluation of experimental data was determined from the mass and energy conversion equations. The measured parameters and values are shown in Table 2.

The evaluation of the HTC for water vapour condensation is usually done according to the Nusselt's condensation theory. However, in the case when NCG is present, a deviation occurs between results from Nusselt's theory and experimental measurements. In Figure 7, a comparison between the results from experimental measurements and the results predicted with the Nusselt's theory for the mean HTC of the film is shown. As it can be seen, the Nusselt theory cannot be used by itself for a result prediction when NCG is present in the condensing mixture. Therefore, it might be useful to use one of the theoretical models presented in the previous section. In Figure 8, the measured amount of condensate captured during the tests is shown. With increasing air inlet concentration, the ratio of condensed vapour significantly

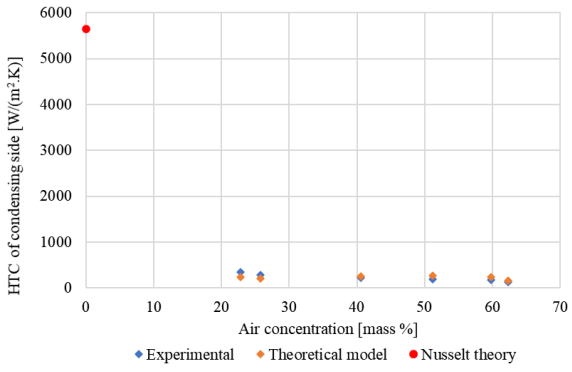

Figure 7. Condensing side HTC comparison obtained from the experiments, developed theoretical model and Nusselt theory.

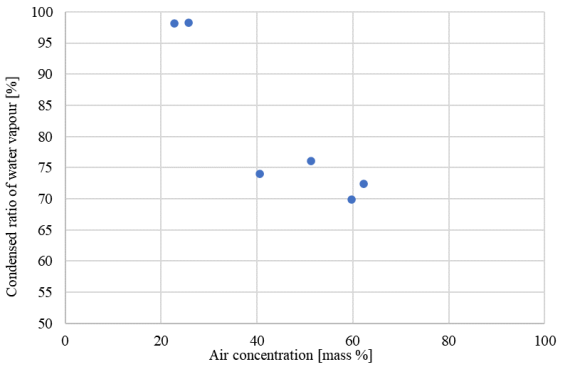

Figure 8. Dependence of the condensed vapour and the air concentration in the mixture.

decreases. It was observed that in the case of the inlet air mixture concentration of 20 %, almost all the vapour condensed. This is in accordance with the results from the theoretical model.

4.3. Comparison of results from experiments and the theoretical model

The predicted results from the theoretical model were compared with the results from the experimental measurements. The results were compared with the overall condenser power and are shown in Figure 9. The heat rejected by the cooling water, determined by the experiments and calculated from the theoretical model, is in good agreement with the standard deviation within +25 % and −5 %. In the case of a lower NCG concentration, the theoretical model can predict, with a very high accuracy, the overall condenser power; however, at a higher NCG concentration, the model is less accurate. Another option to compare experimental and theoretical data is through the overall HTC, which is shown in Figure 7. The HTC predicted from the theoretical model for lower values of air inlet concentration are lower than those measured during the experiment. Although this might not be so accurate, since the overall HTC from the model is calculated as an arithmetic ratio of local values. Another reason

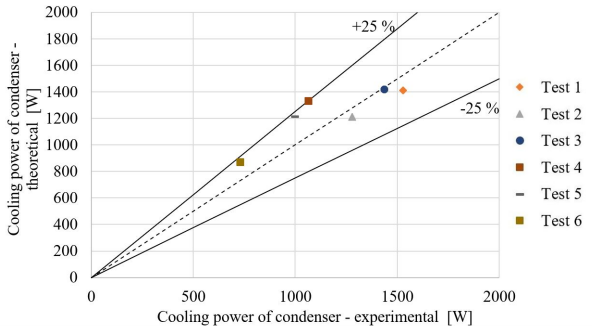

Figure 9. Comparison of condenser power of theoretical model and experiments.

why the HTCs from the theoretical model and experimental measurements differ might be the disturbance of the NCG layer by other phenomena. These might occur during condensation and were not considered in the presented model. In [16, 17], the suction effect, which occurs during the condensation of vapour in the presence of NCG, was analysed and it was concluded that it can improve HTC by even 20 %. The formation of mist can also improve HTC [18, 19]. This occurs when the mass transfer resistance in the mixture is much higher than the heat transfer resistance. However, the clear influence of the suction effect and the formation of mist on the HTC has not yet been determined. Therefore, including these phenomena in the model is rather difficult and unclear, even though it might be viable to do so, since it might improve the accuracy of the results predicted from the theoretical models.

5. Conclusions

Four theoretical methods for the determination of the HTC and heat transfer during condensation of vapour with gas are usually recommended in the literature: degradation and correlation factor, heat and mass transfer analogy, diffusion layer and boundary layer model.

For the theoretical model, based on heat and mass transfer analogy, it was observed that the overall HTC of the condenser decreases as the air concentration increases, also, as the Reynolds number of the mixture decreases, and/or the film thickness increases. An increase in air concentration has the strongest influence on the HTC. This is observed because of the mass transfer resistance of the vapour due to the layer of NCG near the phase interface. Increasing Re number of the mixture or disturbing this layer of NCG near the phase interface might, therefore, increase the HTC of the condensing mixture. The HTC of the film during the condensation of vapour in the presence of a high content of NCG can be several times higher than the HTC of the mixture. Neglecting the HTC of the film might not produce a significant error in calculation and can simplify the theoretical modelling. A significant decrease in film HTC is also seen at the beginning

of the condenser, which corresponds to local condensing flow. A rapid decrease in HTC is observed mainly in the condenser inlet, while in the condenser outlet, HTC is very low and does not change significantly. It was also observed that an effort to condensate all the vapour content out of the mixture leads to a much larger condensing surface, since the HTC is very low at the end of the condenser. Increasing the HTC in the condenser outlet can, therefore, rapidly increase the condenser power and might contribute to condensing a larger portion of the vapour out of the mixture.

An experimental measurement of water vapour condensation in the presence of high concentration of air was carried out in a counter-current vertical double-pipe condenser. Air mass concentration ranged between 23 % and 62 %. A significant decrease in the HTC on the condensing side can be seen in the model and experiment as compared to results from Nusselt theory. Therefore, using the Nusselt theory for vapour condensation in the presence of NCG is not suitable.

The results of the theoretical model and the experimental measurements were compared regarding the cooling power of the condenser. The results from the theoretical model and experiments are in good agreement with the standard deviation within +25 % and −5 %. Therefore, the heat and mass transfer analogy might predict the power of the condenser and the HTC of vapour condensation in the presence of large amount of NCG with a sufficient accuracy. A larger accuracy is observed for a low NCG concentration than for a higher NCG concentration. Precaution is, therefore, recommended when using the model for a higher NCG concentration. Obtained results are valid for all vertical geometries when the width of the condensate film is negligible compared to the cross section of the flow. In addition, studying other factors that might influence the condensation of vapour in the presence of NCG, such as the suction effect and mist formation, can enhance the accuracy of the heat-mass transfer model. Experiments to determine the effect of NCG on water vapour condensation have been performed, so far, for an artificially prepared mixture of water vapour and air, also because of the availability of relevant literature references. Another goal of the research is to verify the process of water vapour condensation from a mixture with CO_2 to apply this method for drying flue gas from oxyfuel combustion.

List of symbols

a Air
A Heat exchanger area $[m^2]$
C Geometric dimensionless number in empirical equation
$\tilde{c}_p$ Molar specific heat capacity $[J\,kg^{-1}\,K^{-1}]$
E_T Ackermann factor [–]
$\Delta\tilde{h}_v$ Molar heat of condensation $[J\,mol^{-1}]$
HTC Heat transfer coefficient $[W\,m^{-2}\,K^{-1}]$
k Overall heat transfer coefficient $[W\,m^{-2}\,K^{-1}]$
k' Heat transfer coefficient between phase interface and coolant $[W\,m^{-2}\,K^{-1}]$
K Cooling water
Le Lewis number
n Molar density $[mol\,m^{-3}]$
$\dot{n}$ Local molar flux $[mol\,m^{-2}\,s^{-1}]$
$\dot{N}$ Molar flux $[mol\,s^{-1}]$
NCG Non-condensable gas
Nu Nusselt number [–]
p Vapour
Pr Prandtl number
$\dot{q}$ Heat flux $[W\,m^{-2}]$
r_1 Radius of inner tube [m]
$\dot{r}_v$ Relative molar flow [–]
r_2 Radius of outer tube [m]
Re Reynolds number [–]
Sc Schmidt number [–]
Sh Sherwood number [–]
$\tilde{y}$ Molar concentration [–]

Greek symbols

α Heat transfer coefficient $[W\,m^{-2}\,K^{-1}]$
$\ddot{\alpha}_G$ Heat transfer coefficient of condensing side $[W\,m^{-2}\,K^{-1}]$
β Mass transfer coefficient $[m\,s^{-1}]$
λ Thermal conductivity $[W\,m^{-1}\,K^{-1}]$
Φ_T Non-dimensional mass flow [–]

Subscripts

1 Inlet
2 Outlet
a Power products in empirical equation
B Bulk
c Condensation
cv Convection
F Film
F,SAT Film saturation
i Inner
KON Condensate
G Gas
SAT Saturation
v Vapour
W Wall

Acknowledgements

This work was supported by the Ministry of Education, Youth and Sports under OP RDE grant number CZ.02.1.01/0.0/0.0/16_019/0000753 "Research centre for low-carbon energy technologies".

References

[1] O. Reynolds, H. E. Roscoe. I. On the condensation of a mixture of air and steam upon cold surfaces. *Proceedings of the Royal Society of London* **21**(139-147):274–281, 1873. https://doi.org/10.1098/rspl.1872.0056.

[2] M. Ge, S. Wang, J. Zhao, et al. Condensation of steam with high CO_2 concentration on a vertical plate. *Experimental Thermal and Fluid Science* **75**:147–155,

2016. https://doi.org/10.1016/j.expthermflusci.2016.02.008.

[3] J. Huang, J. Zhang, L. Wang. Review of vapor condensation heat and mass transfer in the presence of non-condensable gas. *Applied Thermal Engineering* **89**:469–484, 2015. https://doi.org/10.1016/j.applthermaleng.2015.06.040.

[4] J.-D. Li, M. Saraireh, G. Thorpe. Condensation of vapor in the presence of non-condensable gas in condensers. *International Journal of Heat and Mass Transfer* **54**(17-18):4078–4089, 2011. https://doi.org/10.1016/j.ijheatmasstransfer.2011.04.003.

[5] C. Chantana, S. Kumar. Experimental and theoretical investigation of air-steam condensation in a vertical tube at low inlet steam fractions. *Applied Thermal Engineering* **54**(2):399–412, 2013. https://doi.org/10.1016/j.applthermaleng.2013.02.024.

[6] W. Minkowycz, E. Sparrow. Condensation heat transfer in the presence of noncondensables, interfacial resistance, superheating, variable properties, and diffusion. *International Journal of Heat and Mass Transfer* **9**(10):1125–1144, 1966. https://doi.org/10.1016/0017-9310(66)90035-4.

[7] F. Toman, P. Kracík, J. Pospíšil, M. Špiláček. Comparison of water vapour condensation in vertically oriented pipes of condensers with internal and external heat rejection. *Energy* **208**:118388, 2020. https://doi.org/10.1016/j.energy.2020.118388.

[8] N. Maheshwari, D. Saha, R. Sinha, M. Aritomi. Investigation on condensation in presence of a noncondensable gas for a wide range of reynolds number. *Nuclear Engineering and Design* **227**(2):219–238, 2004. https://doi.org/10.1016/j.nucengdes.2003.10.003.

[9] H. C. No, H. S. Park. Non-iterative condensation modeling for steam condensation with non-condensable gas in a vertical tube. *International Journal of Heat and Mass Transfer* **45**(4):845–854, 2002. https://doi.org/10.1016/S0017-9310(01)00176-4.

[10] P. Kracík, F. Toman, J. Pospíšil. Effect of the flow velocity of gas on liquid film flow in a vertical tube. *Chemical Engineering Transactions* **81**:811–816, 2020. https://doi.org/10.3303/CET2081136.

[11] S. Kuhn, V. Schrock, P. Peterson. An investigation of condensation from steam–gas mixtures flowing downward inside a vertical tube. *Nuclear Engineering and Design* **177**(1-3):53–69, 1997. https://doi.org/10.1016/S0029-5493(97)00185-4.

[12] W. Nusselt. *Des oberflachenkondensation des wasserdamfes*, vol. 60. Z. VereinesDeutsch. Ing., 1916.

[13] K. Karkoszka. *Theoretical investigation of water vapour condensation in presence of noncondensable gases*. Licentiate thesis, Royal Institute of Technology, Division of Nuclear Reactor Technology, Stockholm, Sweden, 2005.

[14] VDI e. V. *VDI Heat Atlas*. Springer Berlin, Heidelberg, 2010. https://doi.org/10.1007/978-3-540-77877-6.

[15] A. P. Colburn, O. A. Hougen. Design of cooler condensers for mixtures of vapors with noncondensing gases. *Industrial & Engineering Chemistry* **26**(11):1178–1182, 1934. https://doi.org/10.1021/ie50299a011.

[16] L. E. Herranz, A. Campo. Adequacy of the heat-mass transfer analogy to simulate containment atmospheric cooling in the new generation of advanced nuclear reactors: Experimental confirmation. *Nuclear Technology* **139**(3):221–232, 2002. https://doi.org/10.13182/NT02-A3315.

[17] S. Oh, S. T. Revankar. Experimental and theoretical investigation of film condensation with noncondensable gas. *International Journal of Heat and Mass Transfer* **49**(15-16):2523–2534, 2006. https://doi.org/10.1016/j.ijheatmasstransfer.2006.01.021.

[18] M. Y. a Hijikata Kunio. Free convective condensation heat transfer with noncondensable gas on a vertical surface. *International Journal of Heat and Mass Transfer* **16**(12):2229–2240, 1973. https://doi.org/10.1016/0017-9310(73)90009-4.

[19] H. C. Kang, M. H. Kim. Characteristics of film condensation of supersaturated steam–air mixture on a flat plate. *International Journal of Multiphase Flow* **25**(8):1601–1618, 1999. https://doi.org/10.1016/S0301-9322(98)00077-9.

EXPERIMENTAL VERIFICATION OF THE EFFICIENCY OF SELECTIVE NON-CATALYTIC REDUCTION IN A BUBBLING FLUIDIZED BED COMBUSTOR

Kristýna Michaliková*, Jan Hrdlička, Matěj Vodička, Pavel Skopec, Jitka Jeníková, Lukáš Pilař

Czech Technical University in Prague, Faculty of Mechanical Engineering, Department of Energy Engineering, Technická 4, 166 07 Prague, Czech Republic

* corresponding author: kristyna.michalikova@fs.cvut.cz

Abstract. Controlling nitrogen oxide (NO_X) emissions is still a challenge as increasingly stringent emission limits are introduced. Strict regulations will lead to the need to introduce secondary measures even for boilers with bubbling fluidized bed (BFB), which are generally characterized by low NO_X emissions. Selective non-catalytic reduction has lower investment costs compared to other secondary measures for NO_X reduction, but the temperatures for its efficient utilization are difficult to achieve in BFBs. This paper studies the possibility of an effective application of selective non-catalytic reduction (SNCR) of nitrogen oxides in a pilot-scale facility with a bubbling fluidized bed. The effect of temperatures between 880 and 950 °C in the reagent injection zone on NO_X reduction was investigated. For the selected temperature, the effect of the amount of injected reagent, urea solution with concentration 32.5 % wt., was studied. The experiments were carried out using 500 kW_{th} pilot scale BFB unit combusting lignite. In addition, an experiment was performed with the combustion of wooden pellets. With reagent injection, all experiments led to the reduction of nitrogen oxides and the highest NO_X reduction of 58 % was achieved.

Keywords: Selective non-catalytic reduction, SNCR, fluidized bed, BFB, denitrification.

1. Introduction

The future of the energy industry is inextricably linked to the need to prevent the release of pollutants and greenhouse gases. One of the monitored pollutants is nitrogen oxides, which is the collective term for nitric oxide (NO) and nitrogen dioxide (NO_2). Their formation is well known and is described even in fluidized bed combustion [1, 2]. Nitrogen oxides have a negative impact on the environment and contribute to problems such as acid rain, ozone depletion, and photochemical smog [3]. The nitrous oxide (N_2O) is a gas with a greenhouse effect. It is also formed during combustion, particularly at lower temperatures. At higher temperatures (greater than 1 500 K), it is rapidly decomposed, forming N_2 or NO [4]. Therefore, its emissions may be of significance in the case of combustion in fluidized beds, which are generally operated at lower temperatures and do not reach the temperature range for its oxidation. Besides the combustion process itself, its significant source can be an application of a selective non-catalytic reduction of NO_X [5], particularly at elevated ratios of the reducing agent [6].

Fluidized bed boilers are widely used for their advantages, such as fuel flexibility, uniform temperature distribution, and operation at low temperatures. Bubbling fluidized bed (BFBs) as well as circulation fluidized bed combustors (CFBs) allow the combustion of fuels of different sizes, moisture content, and heating values, and therefore can be used not only for the combustion of coal, but also for the combustion of biomass or various alternative fuels. The operating temperatures in the fluidized bed are in the range of 800–950 °C [7]. This lower operating temperature range also leads to a lower formation of NO_X. The formation of nitrogen oxides can generally be realised by three mechanisms – thermal, prompt, and fuel NO_X [8, 9]. The thermal and prompt pathways become more important above the operating temperature range of fluidized bed combustors and are therefore negligible during fluidized bed combustion and fuel NO_X is then considered the main contributor to nitrogen oxides.

2. Measures for NO_X reduction

Reduction of NO_X emissions can be achieved by modifying the combustion process, thereby preventing the formation of NO_X, known as primary measures, or by secondary measures, which are techniques for the reduction of already generated nitrogen oxides.

In principle, all primary measures involve adjustments leading to combustion conditions with a decreased O_2 availability at the early stage of the combustion process, a reduction of the maximum flame temperature, or a change in residence time in different parts of the combustion zone [5]. For fluidized bed combustors, the early stage of the combustion process takes place in the dense bed zone. One of

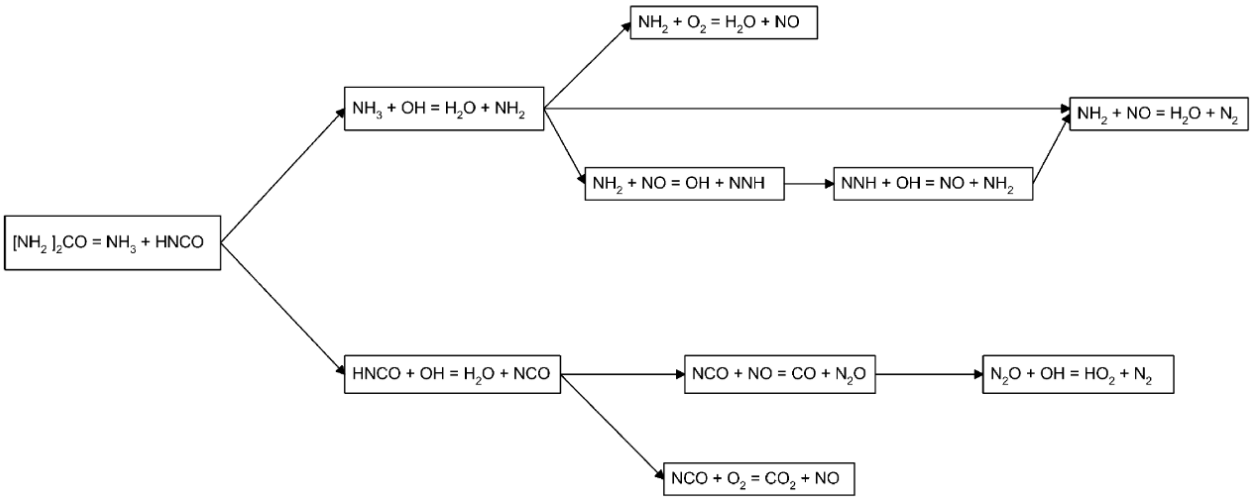

Figure 1. Reaction path diagram with urea as a reagent [5].

the measures can be air staging, which presents the oxygen-lean primary combustion zone and the oxygen-rich secondary combustion zone. It is realized by supplying secondary or even multi-stage air above the area of primary combustion, typically to the freeboard of the BFBs or to the lean bed zone of the CFBs. Air staging is often used in BFBs to control combustion and ensure the required temperature and overall oxygen stoichiometry. The use of flue gas recirculation is required for fluidized bed combustion because it provides the necessary volume flow to fluidize the bed material. Most primary measures are less effective in the case where the generated NO_X is predominantly formed by the oxidation of fuel nitrogen [5], which is a typical situation for fluidized bed combustors. Therefore, to meet the NO_X limits, secondary measures may be necessary.

Secondary measures are used to reduce nitrogen oxides that have been already formed. These post-combustion technologies that reduce NO_X are mainly selective catalytic (SCR) and selective non-catalytic reduction (SNCR). These flue gas treatments reduce NO_X to N_2 by reaction with an amine-based reagent, such as ammonia or urea. Both technologies are widely used.

In the process of SCR, the catalyst is present, reducing the activation energy of key reactions. Therefore, the reduction of NO to molecular nitrogen is realized in the temperature range 290–450 °C [10]. The efficiency of SCR at similar reducing agent stoichiometric ratio is higher than for SNCR and can reach above 90 %, however, the investment and operating costs are significant and its installation has a large space requirement [11]. This may limit its application as a retrofit to an existing facility. Additional problems can be fouling and catalyst poison. On the other hand, SNCR can be easily retrofitted, and its investment costs are lower because of the absence of the catalyst.

2.1. Selective non-catalytic reduction

SNCR is a well-known and described technology [5], but its application in fluidized bed combustors is rare. This is mainly due to the lower formation of NO_X in fluidized bed combustion, which can then operate within the emission limits. The problem may arise if these limits for NO_X emissions are even stricter or fuels with higher fuel-nitrogen content are burned, for example, non-wooden biofuels.

Several different reducing agents can be used in the SNCR process. The reduction process with ammonia is called the Thermal DeNOx process, whereas the use of urea is called the NOxOUT process. A less common reducing agent is cyanuric acid within the RAPRENOx process. Since urea decomposes into ammonia and cyanuric acid, the SNCR process with urea can be considered as the combination of the other two [12]. The reaction path of urea within the selective non-catalytic reduction is shown in Figure 1, which describes the decomposition of urea into ammonia and cyanuric acid and subsequent reactions.

The reduction of NO_X occurs in a temperature range called a temperature window. This required temperature window is affected by many factors and the influence on it has parameters such as the reducing agent, the composition of the flue gas, the residence time, and the mixing between the reagent and the flue gas [5]. However, the interval is usually given in the range 800–1 100 °C; the temperature window for ammonia is 850–1 000 °C and for urea is the temperature window wider (800–1 100 °C) [13]. Below these temperatures, the reaction is too slow and most of the injected ammonia remains unreacted, increasing the slip of ammonia. At temperatures above 1 200 °C, the degree of NO_X reduction decreases due to the thermal decomposition of the reagent that subsequently oxidizes [5].

The amount of reagent injected is usually represented by a normalized stoichiometric ratio (NSR), which defines the number of moles of injected NH_2^- reagent relative to the number of moles of NO_X. For SNCR, the preferred normalized stoichiometric ratio is greater than 1, and a ratio NSR in the range of 1.5–2.5 is generally recommended [13].

As mentioned above, the temperatures in the dense bed of BFB are usually in the range $800 - 900\,°C$, and therefore it is evident that it is difficult to reach sufficiently high temperatures in the freeboard zone for efficient SNCR application. However, our previous work [14] that has been done in a laboratory-scale BFB combustor confirmed that such temperatures can be reached in the freeboard section of a BFB combustor through an intensively staged supply of combustion air. Such an intensive air staging, which means that understoichiometric conditions are established in the primary combustion zone in the dense bed, is not typically applied in the industrial practice. In parallel, the application of SNCR in a BFB combustor is not common, and the original experimental data from this study contribute to the possible realization of this technology.

In this article we have therefore focused on an experimental study of real performance of the selective non-catalytic reduction of NO_X in a $500\,kW_{th}$ pilot scale BFB combustor in connection with intensive air staging in order to increase the temperature of gas phase in the freeboard section, where the reducing agent was injected. This temperature was in the range for effective reduction of NO_X. In this work, the characterization of the SNCR performance in correlation with the NSR and the temperature in the freeboard section where the reducing agent was injected is presented.

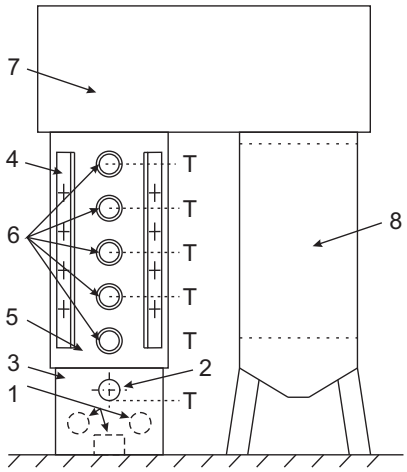

FIGURE 2. Scheme of the $500\,kW_{th}$ pilot-scale BFB facility. 1) primary gas inlets, 2) fuel feeder, 3) dense bed region, 4) secondary air distributors, 5) freeboard section, 6) inspection windows, 7) crossover pass, and 8) heat exchanger. The 'T' signs indicates the temperature measurement points.

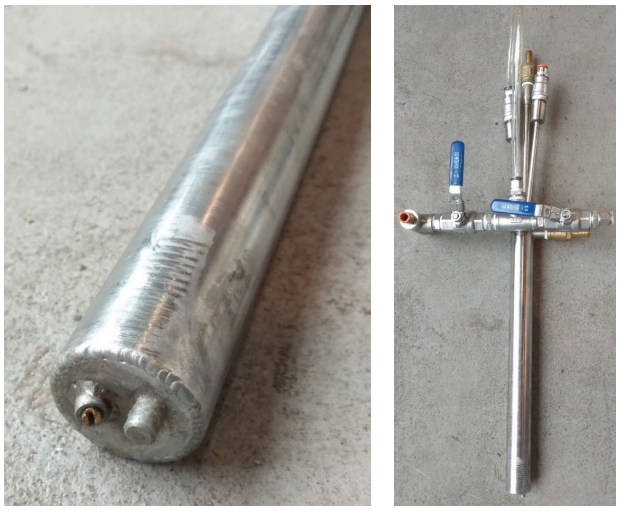

FIGURE 3. Injection probe.

3. EXPERIMENTS

3.1. EXPERIMENTAL SETUP

The experiments were carried out in a pilot scale bubbling fluidized bed combustor with a thermal input of 500 kW, and its scheme is given in Figure 2. The facility is very variable as it allows combustion of different fuels with different oxidants; it is possible to use oxygen-enriched air up to the pure oxy-fuel regime. In the case of the air regime, a mixture of primary air and recirculated flue gas provides the fluidization, and its volume and mixture ratio can be changed arbitrarily. The combustion chamber together with the freeboard is insulated with fireclay lining, and the walls of the boiler are water-cooled. Four secondary air distributors are evenly spaced around the perimeter and each can supply secondary air at 4 heights. In addition, the inspection windows are located in the freeboard, which can be used for injection of reagent within the selective non-catalytic reduction process. The flue gas was continuously sampled. The volumetric fraction of O_2 was measured using a paramagnetic sensor and using a lambda probe (for operation). The volumetric fractions of SO_2, CO_2, CO, NO_X (sum of NO and NO_2), and N_2O were measured using NDIR sensors. The volumetric fraction of NH_3 was measured using a FTIR analyzer.

For selective non-catalytic reduction, the main part of realization is reagent injection. In this case, a single probe with a spray nozzle was used (Figure 3). The probe is water-cooled, and compressed air is used to atomize the reagent. The probe can be placed at five different heights along the freeboard zone using inspection windows. The reducing agent was transported from an accumulation vessel to the nozzle by increasing the air pressure above the level of the reducing agent in the accumulation vessel. The volumetric flow of the reducing agent was controlled by a manually operated proportional valve placed in the stream of the reducing agent. Two rotameters were used to measure the volumetric flow of the reducing agent, which

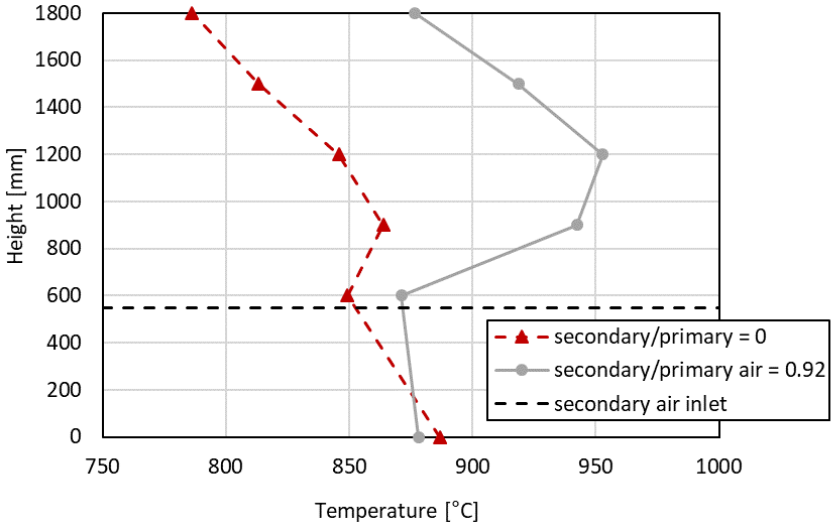

Figure 4. The temperature profile along the height of the facility with and without the use of secondary air.

	As received				Dry ash free					
	LHV [MJ · kg^{-1}]	Water [wt. %]	Ash [wt. %]	Comb.* [wt. %]	C [wt. %]	H [wt. %]	N [wt. %]	S [wt. %]	O* [wt. %]	Volatiles [wt. %]
Lignite	17.6	21.1	9.9	69.0	72.3	6.3	1.1	1.3	19.0	47.0
Wood	16.4	7.8	1.5	90.7	51.0	6.9	0.3	0.003	41.797	84.6

* Calculated as balance to 100 %.

Table 1. Proximate and ultimate analysis of the fuels used within the experiments.

differed in the operating range - the first measured flow in the range 0–1.2 l/h and the second in the range 1–5 l/h.

To achieve the temperature window for efficient injection of the reagent, air staging was realized. It leads to the primary zone with sub-stoichiometric conditions, above which the secondary air inlet is located that creates fuel-lean zone. Thanks to this measure, it was possible to obtain higher temperatures in the freeboard area while keeping the bed temperature below 900 °C. Air staging simultaneously serves as a primary measure that leads to a reduction of NO_X. A comparison of temperature profiles within the combustor during non-staged and staged combustion is given in Figure 4. The dashed horizontal line indicates the height level of secondary air supply in the combustor. Each point in the chart corresponds to a mean temperature value measured at that specific position. The locations of the thermocouples are indicated in Figure 2 by a 'T' sign. The height of 0 mm corresponds to the average temperature in the dense bed measured by 4 thermocouples. The temperatures in the freeboard section were measured by two thermocouples at each height. It can be seen that the temperature of the flue gas slightly higher than 950 °C was reached at a height of 1 200 mm above the dense bed. At this point, the reducing agent for SNCR was injected.

3.2. Materials and methods

The experiments were carried out using Czech lignite Bílina HP1 135 and wooden pellets as fuels. The proximate and ultimate analyses of the lignite and wooden pellets are given in Table 1.

During experiments with lignite coal, its inherent ash was used as a bed material. Experiments with biomass were realized combusting wooden pellets (according to the standard ENplus A1) and using a lightweight ceramic aggregate with a mean diameter of 1.12 mm as a bed material, which is described in detail in [7].

The reagent used in all experiments with lignite as fuel was a urea solution with a concentration of 32.5 % by weight. Since the wooden biomass combustion is expected to lead to a lower production of NO_X due to the significantly lower nitrogen content in the fuel, it was necessary to adjust the concentration of reagent to 10.8 % wt. to ensure sufficient flow of the urea solution.

Several series of experiments were performed for lignite and one experiment for the combustion of wooden pellets. In order to achieve temperatures in the freeboard zone (where the injection takes place) suitable for effective nitrogen oxides reduction using SNCR, the high level of staged supply of combustion air had to be realized. The stoichiometry in the fluidized bed for individual experiments is given in Table 2 for lignite combustion. In the case of combusting wooden

Freeboard temperature [°C]	Required freeboard temperature [°C]	Air excess ratio in the dense bed [–]
Combustion of lignite		
870 ± 0.8	870	0.50
882 ± 0.8	880	0.94
885 ± 0.8	890	0.97
925 ± 2.0	920	0.63
949 ± 0.6	950	0.53
Combustion of wood		
886 ± 0.3	880	1.46

TABLE 2. Stoichiometry in the fluidized bed.

pellets, no secondary air was used and the air excess in the dense bed was 1.7. The value representing the freeboard temperature in Figure 2 is an average of values measured at the place of injection of the reducing agent sampled for at least 30 minutes in the interval of 1 s. The average value is given together with the interval of 95 % confidence.

The experiments were performed with a constant bed temperature of 880 °C and the oxygen level in the dry flue gas maintained at 6 % to diminish the impact of these parameters on the NO_X formation. Secondary air was injected 900 mm above the surface of the fluidized bed for lignite. A reference case was measured for each selected temperature and the measured values of the concentration of NO_X were used to calculate the corresponding values of NSR and the efficiency of NO_X reduction. During all experiments, the selected temperature in the freeboard area was kept constant and the amount of urea solution injected was increased in steps. In the case of lignite combustion, the volumetric flow of the urea solution was increased by 0.25 l/h, except for the measurement with the freeboard temperature 870 °C, when the step was 0.15 l/h. Consequently, steady-state cases with volumetric flows of the urea solution of 0, 0.25, 0.5, 0.75, 1, and 1.2 l/h were measured for freeboard temperatures 882, 885, 925, and 949 °C. For freeboard temperature of 870 °C, volumetric flows of the urea solution were 0, 0.15, 0.3, 0.45, 0.60, and 1.2 l/h. In the case of biomass combustion, steady states were measured with volumetric flows of the urea solution of 0, 0.4, 0.85, 1.3, 2, and 3 l/h. The volumetric flow of the urea solution was used together with the reference concentration of NO_X to determine the stoichiometric ratio NSR. In the case of urea $(NH_2)_2CO$, the normalized stoichiometric ratio is defined as two moles of urea in the urea solution to the mole of NO in the flue gas [15]:

$$NSR = 2 \cdot \frac{n_{urea}}{n_{NO}} \tag{1}$$

The NSR ratio was used in the evaluation of the result as the variable parameter that describes the intensity of the SNCR process. Each of the steady-state cases was measured in the average for 40 minutes (at least for 30 minutes). All measured values were sampled with an interval of 1 s except for the NH_3 concentrations and the NO_X concentrations measured downstream of the SNCR in the case of lignite combustion and freeboard temperature 920 °C, where the data were sampled with an interval of 1 minute. All sampled data reported in the results are expressed using averages with corresponding intervals of 95 % confidence.

4. Results and discussion

The measured data from all experiments relevant for this study can be found in Table 3 (for the combustion of lignite) and Table 4 (for the combustion of biomass). All concentrations reported in these tables are calculated for a reference content of O_2 in dry flue gas of 6 %.

Achieving different temperatures in the freeboard zone was realized by different mass flow of fuel, modification of the volume of fluidizing gas and its composition, and changing the volumetric flow of secondary air as well. These adjustments resulted in different initial concentrations of NO_X, which varied from 438 to 498 mg/m^3_N for lignite combustion. The difference in the initial NO_X concentration could also be caused by a slightly different O_2 volumetric fraction in the flue gas. The formation of NO_X is significantly dependent on the availability of O_2 for the oxidation of the fuel N, which was confirmed by Krzywański et al. [16] or Vodička et al. [17]. Although a constant volumetric fraction of O_2 in dry flue gas was desired within all experimental cases, its value varied in the range from 4.3 to 7.3 %. It can be seen in Table 3 that the higher concentrations of NO_X were measured for higher volumetric fractions of O_2 and vice versa. The NO_X concentrations measured for wood combustion were significantly lower than those measured for lignite combustion, particularly due to the significantly lower nitrogen content in the fuel [18].

The measurement of CO concentration in the freeboard and of NH_3 concentration in the flue gas re-

Freeboard temp. (required) [°C]	NO_X before SNCR [mg/m^3_N]	NO_X after SNCR [mg/m^3_N]	NSR [mol/mol]	η_{NO_X} [%]	NH_3 [mg/m^3_N]	O_2 [% vol.]	CO [mg/m^3_N]	CO freeboard [mg/m^3_N]	N_2O [mg/m^3_N]
870±0.8 (870)	438±0.5	438±0.5	0.00	0.0	NA*	6.1±0.04	313±5.4	NA*	19.2±0.19
		396±0.5	0.43	9.6	NA*	6.4±0.05	294±3.5	843±9.8	32.4±0.24
		348±0.5	0.87	20.5	NA*	5.7±0.05	394±15.0	777±13.9	30.4±0.45
		312±0.4	1.30	28.8	0.1±0.02	5.5±0.05	326±10.0	703±5.4	37.8±0.34
		289±0.4	1.70	34.0	0.2±0.03	5.1±0.04	341±12.2	677±3.3	41.2±0.46
		276±0.9	3.47	37.0	0.4±0.08	5.4±0.06	385±9.8	NA*	47.1±0.88
882±0.8 (880)	460±0.6	460±0.6	0.00	0.0	NA*	6.7±0.04	268±1.9	NA*	23.2±0.18
		390±0.5	0.55	15.1	NA*	6.8±0.04	303±2.3	NA*	30.7±0.19
		303±0.4	1.10	34.1	NA*	5.9±0.03	294±2.2	NA*	43.5±0.22
		265±0.5	1.65	42.3	NA*	5.6±0.03	283±2.3	NA*	55.8±0.30
		256±0.5	2.20	44.4	NA*	5.7±0.03	345±2.5	NA*	72.0±0.29
		241±0.4	2.64	47.5	NA*	5.9±0.03	333±2.4	NA*	83.4±0.27
885±0.8 (890)	443±1.1	443±1.1	0.00	0.0	NA*	4.9±0.05	216±2.5	NA*	19.8±0.09
		415±0.8	0.62	6.4	NA*	5.3±0.04	196±1.0	NA*	30.8±0.12
		360±0.7	1.30	18.7	NA*	4.6±0.03	182±1.2	NA*	32.8±0.13
		299±1.2	1.89	32.5	NA*	4.4±0.05	225±2.1	NA*	33.4±0.23
		202±1.0	2.50	54.4	NA*	4.6±0.04	511±16.7	NA*	37.0±0.40
		181±0.6	3.00	59.6	NA*	4.6±0.04	265±7.3	NA*	73.8±0.61
925±2.0 (920)	498±3.8	498±3.8	0.00	0.0	NA*	7.0±0.08	221±4.8	539±15.7	NA*
		458±1.3	0.41	8.0	0.1±0.02	7.0±0.08	227±3.5	660±72.5	NA*
		450±1.9	0.81	9.5	0.01±0.01	7.2±0.07	283±7.0	1883±94.1	NA*
		410±3.6	1.23	17.7	0.01±0.01	7.2±0.04	216±5.9	1274±39.4	NA*
		364±10.8	1.97	26.9	0.3±0.04	7.3±0.20	265±21.3	1564±71.6	NA*
949±0.6 (950)	468±0.3	468±0.3	0.00	0.0	0.03±0.02	6.8±0.03	219±9.1	NA*	6.8±0.36
		454±0.6	0.57	2.9	0.03±0.01	6.3±0.03	306±24.2	773±34.9	16.0±0.43
		442±0.9	1.12	5.5	0±0	5.5±0.04	358±18.2	958±18.4	14.4±0.55
		430±0.4	1.70	8.3	0±0	4.3±0.02	321±20.7	1027±20.0	12.6±0.54
		399±0.7	2.70	14.7	0.77±0.10	4.7±0.04	282±14.5	833±19.6	23.0±0.69

* The value was not available for this experiment.

Table 3. Operating conditions during experiments for lignite combustion, $O_{2,ref} \approx 6\,\%$.

Freeboard temp. (required) [°C]	NO_X before SNCR [mg/m^3_N]	NO_X after SNCR [mg/m^3_N]	NSR [mol/mol]	η_{NO_X} [%]	NH_3 [mg/m^3_N]	O_2 [% vol.]	CO [mg/m^3_N]	CO freeboard [mg/m^3_N]	N_2O [mg/m^3_N]
886±0.3 (880)	145±0.5	145±0.5	0	0.0	NA*	6.7±0.02	76±0.4	NA*	4.2±0.14
		133±0.2	1	8.7	NA*	6.4±0.02	60±0.1	NA*	7.5±0.01
		113±0.3	2.2	22.0	NA*	5.4±0.02	55±0.1	NA*	12.6±0.03
		107±0.5	3.3	26.6	NA*	5.2±0.02	54±0.2	NA*	13.1±0.08
		86±0.4	5.1	40.9	NA*	4.8±0.02	52±0.2	NA*	18.9±0.11

* The value was not available for this experiment.

Table 4. Operating conditions during experiments for biomass combustion, $O_{2,ref} \approx 6\,\%$.

quired an additional analyzer. The absence of data of NH_3 and N_2O concentrations in the off-gas and CO concentrations in the freeboard section reported in Tables 3 and 4 was caused by non-availability of the additional FTIR analyzer during the corresponding experimental case.

In all experiments, injection of the reagent resulted in a reduction in nitrogen oxides even at the lowest volumetric flows of the urea solution corresponding to the lowest NSRs. The impact of injection of the urea solution on the concentration of NO_X in the flue gas downstream of SNCR is demonstrated in Figure 5 with injection of reagent expressed as NSR. The NO_X reduction efficiency was calculated as the fraction of the difference in the NO_X concentration after and before SNCR over the NO_X concentration before the SNCR process. The best NO_X reduction efficiency of 58 % was achieved for temperature 885 °C and NSR 3.1 and this efficiency decreased with the use of higher or lower temperatures. This trend is shown in Figure 6 for four different NSRs in the range from 0.5 to 3.3. NO_X reduction was also affected by

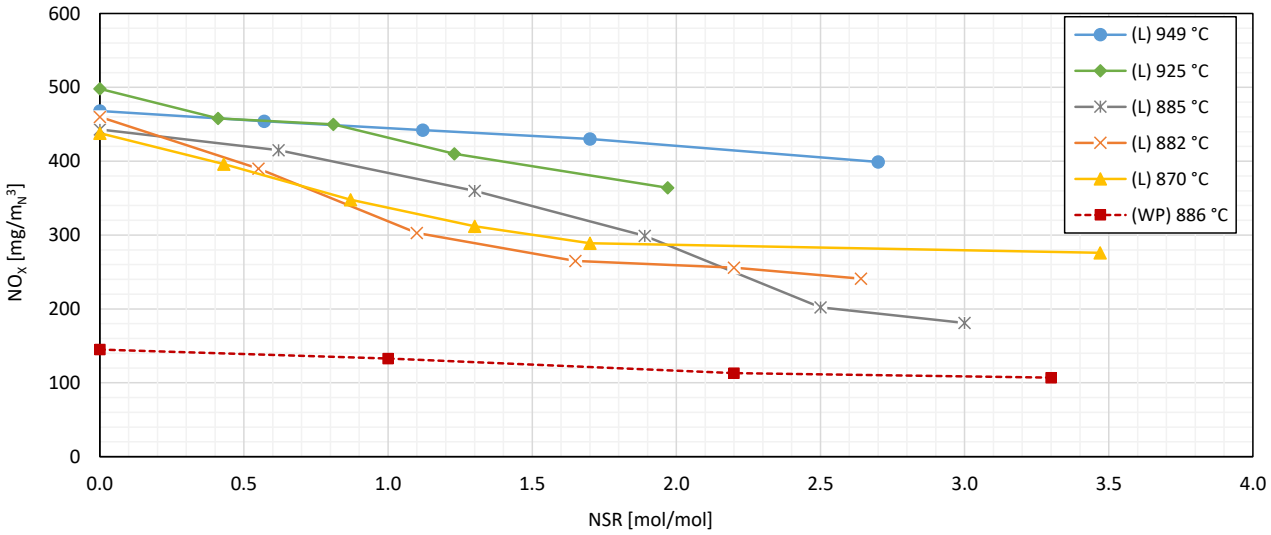

FIGURE 5. Dependence of NO_X concentration in the flue gas downstream the SNCR on NSR for different temperatures, (L) – lignite, (WP) – wooden pellets.

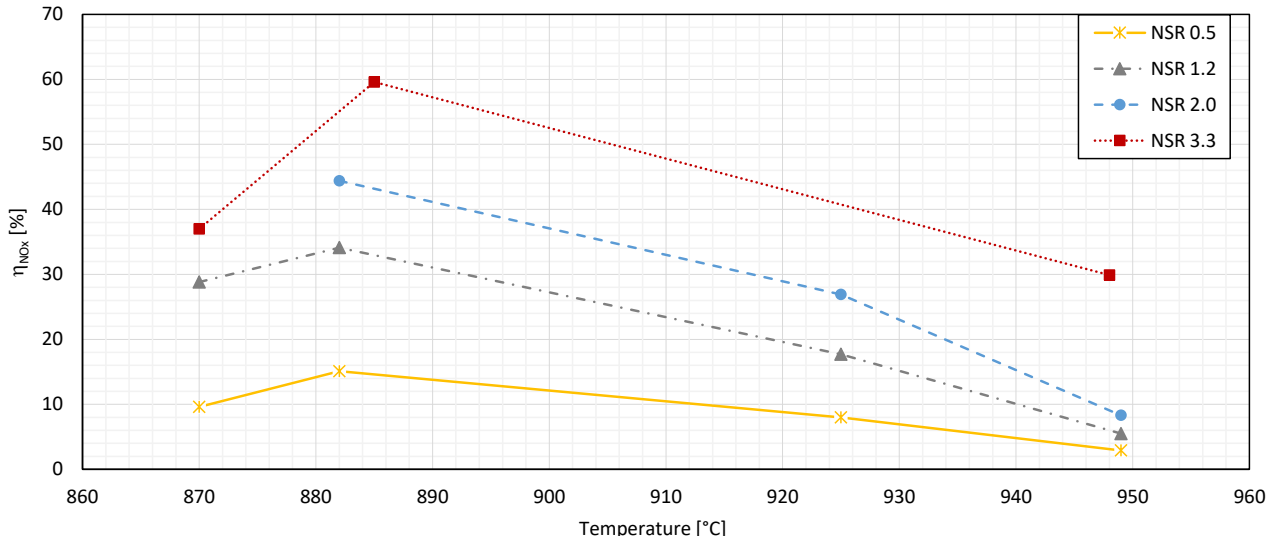

FIGURE 6. Dependence of NO_X reduction efficiency on temperature for different $NSRs$.

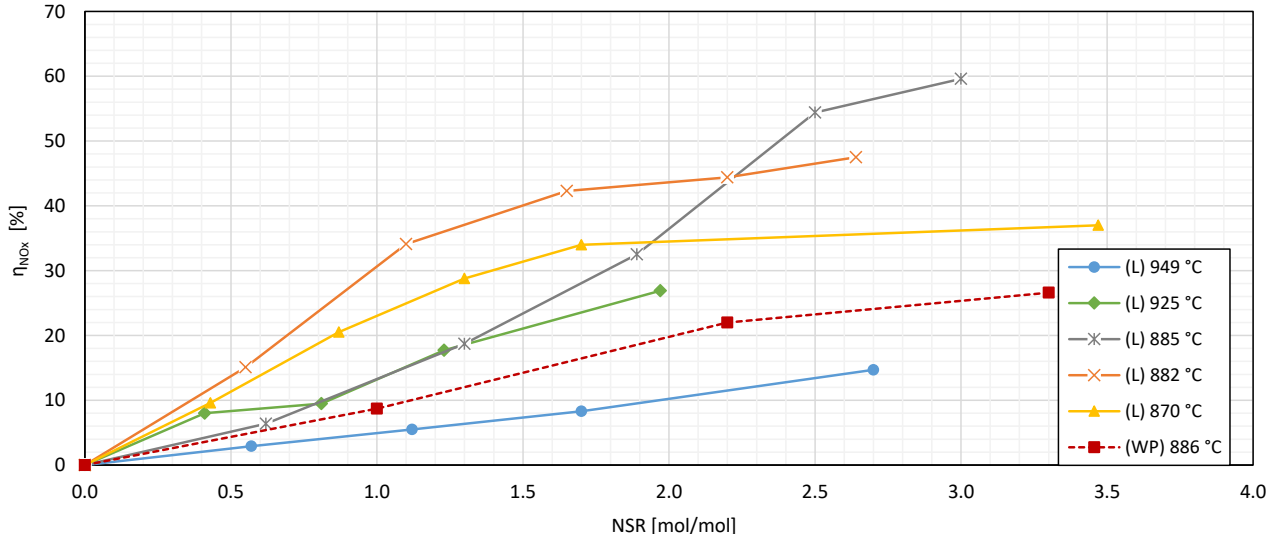

FIGURE 7. Dependence of NO_X reduction efficiency on NSR for different temperatures.

the amount of injected reagent, expressed as NSR. An increase in NSR resulted in an increase in efficiency for all experiments, although the increase in efficiency of the NO_X reduction gradually decreased with increasing NSR, as can be seen in Figure 7, where the dependence of the NO_X reduction efficiency on NSR is given. In the cases where the ammonia slip was measured, the ammonia concentration never exceeded $1\,mg/m^3_N$ for lignite combustion, even for the highest NSRs indicating a strong over-stoichiometry of the urea solution.

N_2O is a greenhouse gas. Its emissions in the energy industry are not currently limited in EU legislation, however, they are negatively affected by selective non-catalytic reduction in the case when urea or cyanuric acid is used as the reducing agent [5]. N_2O concentrations increased with increasing reagent levels, up to four times its initial value, which can be seen in Tables 3 and 4. In the case of lignite combustion, the highest concentrations of N_2O were measured for the highest NSRs and freeboard temperatures 880 and 890 °C, where the NO_X reduction efficiency was the highest and the concentration of NO_X after SNCR was the lowest. For the freeboard temperature of 890 °C and $NSR = 3$, the concentration of N_2O was $73.8\,mg/m^3_N$, which was 40 % of the value of the concentration of NO_X. In the case of the combustion of wooden pellets and NSR 5.1, the concentration of nitrous oxide was $18.9\,mg/m^3_N$, whereas the concentration of NO_X achieved after reduction was $86\,mg/m^3_N$. Thus, the application of SNCR with urea solution can possibly be limited by N_2O emissions.

The best efficiency of nitrogen oxides reduction is achieved by injecting the reagent into the area with a temperature of around 890 °C, which is a lower temperature compared to previous work [5, 19]. This optimal temperature has been found independent of the NSR values. However, to evaluate the effect of temperature on the efficiency of the reduction of NO_X, it would be necessary to keep the other remaining combustion parameters constant, which is not feasible due to the control of the combustion process in a pilot-scale boiler. Therefore, the experiments vary not only in different temperatures in the combustion region but also by the flow rate of the fluidized medium and the ratio of secondary to primary air. These parameters may result in different reagent residence times and different mixing for each series of experiments, and may also affect NO_X reduction efficiency. For lignite combustion, the implementation of air staging increases the concentration of carbon monoxide in the flue gas, which can result in a shift of the temperature window for reagent injection into the lower temperature range [5, 20]. In the case of biomass combustion, only primary air and no air staging was used, and the temperature dependence will be the subject of further studies, but a lower initial level of NO_X can lead to lower reduction efficiency.

5. Conclusion

This paper presents an experimental study of selective non-catalytic reduction of NO_X in a bubbling fluidized bed boiler. Achieving the required temperatures for the reduction reactions was realized by modifying the combustion process by means of high degree of air staging with sub-stoichiometric conditions in the dense bed, which allowed controlling the freeboard temperature in the required range for the SNCR. In several series of experiments in the BFB boiler, efficient application of selective non-catalytic reduction of nitrogen oxides by injecting the urea solution was achieved. During the experiments, it was possible to achieve a nitrogen oxide reduction efficiency of 59.6 % for a normalized stoichiometric excess of reagent 3.0. High values of NSR resulted in a higher ammonia slip in the flue gas. The optimal temperature for the SNCR in this experimental setup was reached at approximately 890 °C, which is a value slightly below the typical optimum reported in the literature. It can be attributed to elevated CO levels in the high-degree air staging operation mode of the combustor. In all experiments, the injection of the reducing agent led to a significant increase in N_2O emissions, which in several cases was up to four times the initial value. The NO_X reduction in the case of biomass combustion was nearly 40 % but due to the different concentrations of urea solution, the results of lignite and biomass combustion are not directly comparable. Further experiments with biomass as fuel will be the subject of continued research, followed by oxy-fuel combustion of lignite and biomass, i.e., combustion with oxygen as an oxidant.

Acknowledgements

This work was supported by the Ministry of Education, Youth and Sports under OP RDE grant number CZ.02.1.01/0.0/0.0/16_019/ 0000753 “Research center for low-carbon energy technologies”.

References

[1] J. E. Johnsson. Formation and reduction of nitrogen oxides in fluidized-bed combustion. *Fuel* **73**(9):1398–1415, 1994. https://doi.org/10.1016/0016-2361(94)90055-8.

[2] P. Skopec, J. Hrdlička, J. Opatřil, J. Štefanica. NO_X emissions from bubbling fluidized bed combustion of lignite coal. *Acta Polytechnica* **55**(4):275–281, 2015. https://doi.org/10.14311/AP.2015.55.0275.

[3] L. Muzio, G. Quartucy. Implementing NOx control: Research to application. *Progress in Energy and Combustion Science* **23**(3):233–266, 1997. https://doi.org/10.1016/S0360-1285(97)00002-6.

[4] C. T. Bowman. Control of combustion-generated nitrogen oxide emissions: Technology driven by regulation. *Symposium (International) on Combustion* **24**(1):859–878, 1992. https://doi.org/10.1016/S0082-0784(06)80104-9.

[5] M. Tayyeb Javed, N. Irfan, B. M. Gibbs. Control of combustion-generated nitrogen oxides by selective non-catalytic reduction. *Journal of Environmental Management* **83**(3):251–289, 2007. https://doi.org/10.1016/j.jenvman.2006.03.006.

[6] C. Mendoza-Covarrubiasr, C. E. Romero, F. Hernandez-Rosales, H. Agarwal. N2O Formation in Selective Non-Catalytic NOx Reduction Processes. *Journal of Environmental Protection,* **2**:1095–1100, 2011. https://doi.org/10.4236/jep.2011.28126.

[7] M. Vodička, K. Michaliková, J. Hrdlička, et al. External bed materials for the oxy-fuel combustion of biomass in a bubbling fluidized bed. *Journal of Cleaner Production* **321**:128882, 2021. https://doi.org/10.1016/j.jclepro.2021.128882.

[8] Y. B. Zeldovich. The oxidation of nitrogen in combustion explosions. *Acta Physiochiochimica USSR* **21**:577–628, 1946.

[9] C. Fenimore. Formation of nitric oxide in premixed hydrocarbon flames. *Symposium (International) on Combustion* **13**(1):373–380, 1971. https://doi.org/10.1016/S0082-0784(71)80040-1.

[10] J. He, K. Chen, J. Xu. *Urban Air Pollution and Control*. 2017. https://doi.org/10.1016/B978-0-12-409548-9.10182-4.

[11] K. Abul Hossain, M. Nazri Mohd Jaafar, A. Mustafa, et al. Application of selective non-catalytic reduction of NOx in small-scale combustion systems. *Atmospheric Environment* **38**(39):6823–6828, 2004. https://doi.org/10.1016/j.atmosenv.2004.09.012.

[12] J. A. Miller, C. T. Bowman. Mechanism and modeling of nitrogen chemistry in combustion. *Progress in Energy and Combustion Science* **15**(4):287–338, 1989. https://doi.org/10.1016/0360-1285(89)90017-8.

[13] M. Mladenović, M. Paprika, A. Marinković. Denitrification techniques for biomass combustion. *Renewable and Sustainable Energy Reviews* **82**:3350–3364, 2018. https://doi.org/10.1016/j.rser.2017.10.054.

[14] M. Vodička, K. Michaliková, J. Hrdlička, et al. Experimental verification of the impact of the air staging on the NO_X production and on the temperature profile in a BFB. *Acta Polytechnica* **62**(3):400–408, 2022. https://doi.org/10.14311/AP.2022.62.0400.

[15] N. Modliński. Numerical simulation of SNCR (selective non-catalytic reduction) process in coal fired grate boiler. *Energy* **92**:67–76, 2015. https://doi.org/10.1016/j.energy.2015.03.124.

[16] J. Krzywański, W. Nowak. Neurocomputing approach for the prediction of NOx emissions from CFBC in air-fired and oxygen-enriched atmospheres. *Journal of Power Technologies* **97**(2):75–84, 2017.

[17] M. Vodička, N. E. Haugen, A. Gruber, J. Hrdlička. NO_X formation in oxy-fuel combustion of lignite in a bubbling fluidized bed - Modelling and experimental verification. *International Journal of Greenhouse Gas Control* **76**:208–214, 2018. https://doi.org/10.1016/j.ijggc.2018.07.007.

[18] M. Lisý, H. Lisá, D. Jecha, et al. Characteristic properties of alternative biomass fuels. *Energies* **13**(6), 2020. https://doi.org/10.3390/en13061448.

[19] S. Daood, M. Javed, B. Gibbs, W. Nimmo. NOx control in coal combustion by combining biomass co-firing, oxygen enrichment and SNCR. *Fuel* **105**:283–292, 2013. https://doi.org/10.1016/j.fuel.2012.06.087.

[20] P. Lodder, J. Lefers. Effect of natural gas, C2H6 and CO on the homogeneous gas phase reduction of NOx by NH3. *The Chemical Engineering Journal* **30**(3):161–167, 1985. https://doi.org/10.1016/0300-9467(85)80026-5.

EXPERIMENTAL AND SIMULATION STUDY OF CO_2 BREAKTHROUGH CURVES IN A FIXED-BED ADSORPTION PROCESS

Marek Nedoma[a,*], Marek Staf[b], Jan Hrdlička[a]

[a] *Czech Technical University in Prague, Faculty of Mechanical Engineering, Department of Energy Engineering, Technická 1902/4, 160 00 Prague 6, Czech Republic*

[b] *University of Chemistry and Technology, Department of Gaseous and Solid Fuels and Air Protection, Technická 5, 166 28 Prague 6, Czech Republic*

[*] corresponding author: marek.nedoma@fs.cvut.cz

Abstract.

This paper focuses on the laboratory experiments of low-temperature adsorption of CO_2 at elevated pressure and on the validation of our mathematical model with the data obtained. The numerical approach uses fitting of adsorption isotherm parameters and sensitivity analysis of parameters influencing the breakthrough curve shape and onset time. We first evaluate the results of breakthrough experiments for zeolite 13X. Then, we use the results obtained to design a dynamic mathematical model to predict the breakthrough curve profile. Experimental results show that zeolite 13X possesses high adsorption capacities (over 10 % of its weight at adsorption temperatures of 293 K and below), as expected. The mathematical simulation was accurate at predicting the breakthrough onset time; however, this prediction accuracy declined with the outlet CO_2 concentration exceeding 75 %, which is discussed. The sensitivity analysis indicated that the choice of different estimates of mass transport and bed porosity, as well as the choice of numerical scheme, can lead to a more accurate prediction, but the same set of parameters is not suitable for all process conditions.

Keywords: Adsorption, breakthrough experiment, CO_2 capture, mathematical modeling, sensitivity analysis.

1. Introduction

A gradual increase in burning fossil fuels emitting primarily CO_2 to the atmosphere has been considered as one of the reasons for steadily warming our planet over the past several decades. Carbon dioxide is a minor contributor to global warming or climate change among greenhouse gases [1], but EU climate policy has unanimously agreed through the Green Deal on targets to reduce CO_2 emissions and to phase out fossil fuels production, while supporting subsidies for non-carbon emitting alternatives [2].

Post-combustion technologies represent a group of non-carbon methods to capture CO_2 from an off-gas downstream of the original plant. Conventional methods are CO_2 scrubbing (e.g., using amine or ammonia solvents), adsorption, and membrane separation [3]. Apart from the principle of CO_2 separation itself, these technologies differ in the field of application where their deployment is the most efficient [4, 5]. Hence, a combination of them is another alternative, however, technically complicated [6]. The amine scrubbing for CO_2 capture is currently operating on a large scale; trade-offs are associated with energy intensive regeneration, toxicity, and instability of solvents [7]. Polymeric membranes generally suffer from expensive materials, laboratory equipment, and manufacturing, which prevents rapid development [8]. The adsorption phenomenon is based on a simple physical principle, however, there are challenges to be overcome, e.g., improvement of adsorption materials, large pressure drops in packed bed, and technical aspects of heat-induced desorption.

1.1. CO_2 capture by adsorption

In the adsorption system, emphasis must be placed on two key aspects: i) the technology and ii) the adsorbent [9].

In terms of technological aspects, the main emphasis should be put on the desorption method and on the bed configuration [10]; the choice of process parameters during adsorption, temperature and pressure can influence the working capacity [11] or the effect of adsorbing water if present in the flue gas [12]. The desorption of the adsorbent can be performed by alternating pressure (pressure- or vacuum-swing cycles), temperature (temperature-swing cycles), or by its combination, i.e., coupling cycles [9]. Pressure-swing systems take place in a fixed-bed reactor, whereas moving-bed, rotary-bed, or fluidised bed reactors are often used in a combination with temperature-swings due to a significantly higher heat transfer rate [10].

The choice of the desorption method and its operating conditions is influenced by the process economy, cycle duration, adsorbent life span (cyclic stability) and working capacity, etc., and by the demands for quality

(purity) and quantity (productivity) of the captured CO_2. The PSA method is well-recognized in industry, for example, in air separation and hydrogen production. However, for the post-combustion CO_2 capture, the atmospheric (desorption) pressure is insufficient to obtain high purity CO_2 and the energy consumption associated with gas pressurisation increases rapidly with volumetric flow. VSA cycles are a method of choice by many, for the simplicity and reliability of fixed-bed operation, and a favourable performance of readily available activated carbon or zeolite-based adsorbents; however, producing high purity CO_2 may require inclusion of a second desorption stage. Fixed-bed column sizing, resulting in large column trains for large flue gas throughput, may be overcome by TSA cycles. These cycles have received increasing attention due to the proliferation of research in alternative bed concepts enabling faster cycling by better heat propagation or processing of larger amounts of gas in a single column, as in the case of rotary adsorbers [3, 13]. Furthermore, temperature swings allow to operate on a wider range of working capacities, for example, of metal-organic frameworks (MOFs) [14]. Generally, adsorbents with higher working capacities are better suited for pressure-swing-based cycles, whereas TSA can exploit the potential of high working capacities better, achieving a lower energy consumption relative to sorbent inventory [15, 16]. Solving the long TSA cycle times decreasing productivity, among other factors, is still a challenge. Therefore, carefully combining pressure- and temperature-swings becomes attractive [13].

An adsorbent is a solid substance (carbonaceous or non-carbonaceous) that should possess high CO_2 sorption capacity, high CO_2 selectivity, good kinetics, mechanical strength, and so on, while being inexpensive to manufacture [17].

The classification of adsorbent usually has to be known prior to the technology. It can be performed experimentally in several ways, most commonly: breakthrough experiments, volumetric analysis, thermogravimetric analysis, or zero-length column technique [18]. The selection of suitable adsorbents is followed by a process analysis. Its performance is evaluated by a theoretical calculation or measurement of CO_2 purity after desorption, adsorbent recovery, CO_2 productivity, and energy consumption of the process. These parameters are typically related to each other [19]. Productivity is related to the management of captured CO_2, e.g., storage or utilisation (in most cases, 95 % purity is required [20]). Energy consumption is of great importance in the industrial sector [21]. An experimental acquisition of these parameters is the most valuable, but generally expensive and time-consuming. The prevailing trend is to use a mathematical simulation to predict the physical properties of certain adsorbents (typically, finely tuned MOFs by so-called "adsorbent screening" [22, 23]), as well as the process performance in a fraction of the time [24]. Once verified by experimental data, the mathematical model can be applied to any system with a similar configuration, allowing to use different parameters or materials.

In this paper, we address an experimental characterisation of CO_2 adsorbents in a fixed bed laboratory apparatus and validation of a mathematical model using the obtained results. The model was designed in accordance with the ongoing process in the apparatus. It is used to predict the shape of the breakthrough curve, obtained from the experiments, and subsequently subjected to a sensitivity analysis.

2. Materials and Methods

2.1. Materials

In this work, we have selected a commercial sample of porous non-polar adsorbent without any further modifications, molecular sieve 13X (*Merck - Sigma-Aldrich*, Germany), for the CO_2 adsorption experiments. The adsorbent particles with homogeneous structure had a regular spherical shape and smooth surface. Their diameter ranged from 1.9 to 2.1 mm with a volume of $2.84 - 3.46$ mm^3; other characteristics are summarised in Table 1.

2.2. Experimental setup

An experimental apparatus for the adsorption experiments was built on the basis of a former high-temperature fluidized bed system [25]. Details are listed in Table 1 and Figure 1.

The apparatus is composed of the gas distribution and flow control systems, the adsorption column and humidifier, the climate chamber with programmable temperature controller, and the analytical terminal. The front and top views (same measuring scale) are shown in Figure 3. Figure 4 shows a glazed chamber after the apparatus is placed inside the climate chamber, which ensures the desired temperature of the entire system.

The core of the adsorption apparatus is a cylindrical stainless steel adsorption column, in which the adsorbent is placed.

The gas mixture simulating the pre-purified flue gas (i.e., undergoing a denitrification, desulphurisation, and eventual drying since it is virtually impossible to separate CO_2 from untreated flue gas with a single layer of adsorbent [26]) is supplied from a gas cylinder. After passing through the flow controller, the gas is split into two streams by a manual ball valve switch, and can be fed directly into the adsorber or into the spectrometer. This principle is used to evaluate the adsorption capacity. Before entering the adsorber, the gas stream is split again. The first path leads to humidifiers capable of achieving a relative humidity (RH) of $70 - 85$ % at a given temperature and pressure. The second path, used in this study, bypasses the humidifier. The gas passes through the adsorber from the top to the bottom. The gas leaving

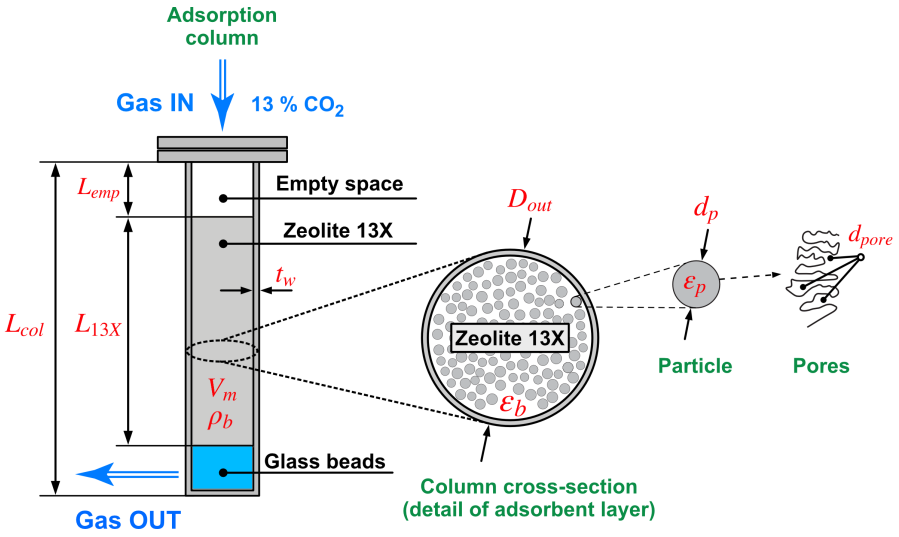

Figure 1. Adsorption column scheme.

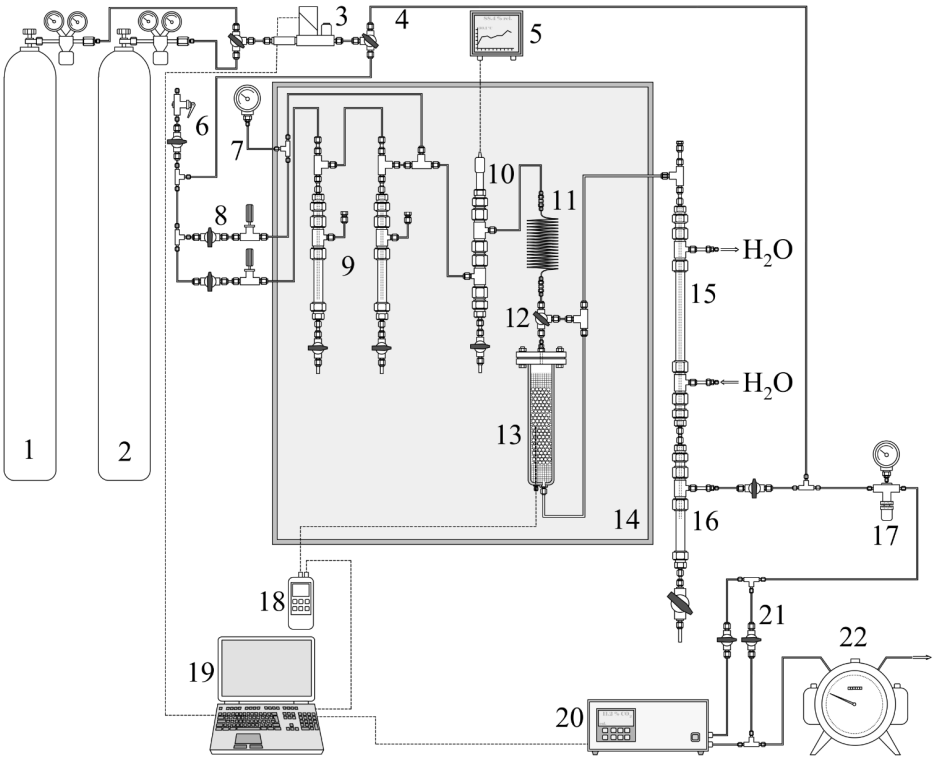

Figure 2. Scheme of the adsorption apparatus: 1, 2 - gas cylinders, 3 - mass flow meter with controller, 4 - three-way valve of the main bypass, 5 - hygrometer display unit, 6 - safety valve, 7 - control manometer, 8 ball and needle valves of humidifier, 9 - pair of humidifiers, 10 - hygrometer pressure sump, 11 - spiral heat exchanger, 12 - three-way valve of the adsorber internal bypass, 13 - adsorber, 14 - climate chamber, 15 - liquid cooler, 16 - condensate sump, 17 - back pressure regulator, 18 - thermometer / data-logger, 19 - PC for data collection and process setting, 20 - infrared spectrometer, 21 - spectrometer bypass setting, 22 - drum-type gas meter.

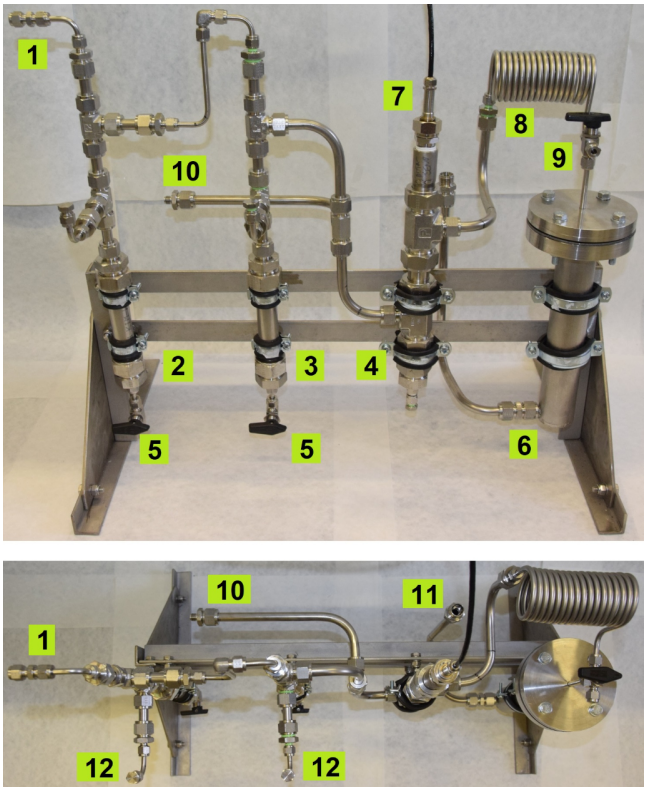

FIGURE 3. Adsorber and humidifier assembly: 1 - gas inlet of the humidifier, 2, 3 - humidifier chambers, 4 - hygrometer pressure sump, 5 - water discharge, 6 - adsorber, 7 - hygrometer probe, 8 - heat exchanger, 9 - three-way valve of the adsorber internal bypass, 10 - dry gas path inlet 11 - adsorber outlet, 12 - water inlet regulator (humidifier wetting).

FIGURE 4. Outside view of the testing apparatus: **A)** 1 - glazed chamber, 2 - adsorber assembly in the climate chamber, 3 - PC (data collection and process control), 4 - side chamber passage of pipes and cables, 5 - liquid cooler, 6 - thermometer with data-logger, 7 - infrared spectrometer, 8 -mass flow meter with controller, 9 - safety valve, 10 - drum-type gas meter, 11 - condensate sump; **B)** climate chamber with the assembled adsorption apparatus.

Adsorption column - Fixed bed	
Material	Stainless Steel
Inner column length, L_{col}	0.26 m
Empty space length, L_{emp}	0.08 m
Inert bed length, L_{gb}	$0.019 - 0.025$ m
Adsorbent bed length, L_{13X}	$0.155 - 0.161$ m
Inner diameter, D_{in}	0.04 m
Wall thickness, t_w	0.002 m
Adsorbent - Zeolite 13X	
Material	Molecular sieve 13X, Sigma Alrich
Material volume, V_m	$195 - 202\,\mathrm{cm}^3$
Material weight, m_m	$0.1425 - 0.1435$ kg
Bulk density, ρ_b	$710 - 730\,\mathrm{kg/m}^3$
Bed porosity, ε_b	0.373^*
Particles shape	Homogenous spheres
Particle diameter, d_p	$1.90 - 2.10$ mm
Particle volume, V_p	$2.84 - 3.46\,\mathrm{mm}^3$

Estimated using Equation 2.

TABLE 1. Apparatus dimensions, physical properties of the adsorbent material (Zeolite 13X) and the fixed-bed.

the adsorber and the climate chamber is cooled in a liquid bath. Any excess moisture is condensed, and the gas pressure is reduced to atmospheric level. At the outlet of the apparatus, the gas enters an infrared (IR) spectrometer *Ultramat 23 IR* and then a drum-type gas meter. Monitoring of the adsorption and desorption is carried out by an online analysis of the gas flowing through the apparatus. The method of sorption rate evaluation is based on the comparison of the adsorptive content in the gas at the adsorption column's inlet and outlet. A view of the apparatus in operation is shown in Figure 4.

2.3. Breakthrough experiments

The breakthrough experiment is performed under dynamic conditions with a constant flow rate at the inlet. The investigated gas mixture contains a known concentration of the adsorptive. From the obtained breakthrough curves, other physical parameters, such as adsorption rate, separation efficiency under given conditions, and specific consumption of sorbent can be evaluated.

The actual measurement of one cycle consisting of adsorption and desorption is performed as follows:

1. **Regeneration**: the adsorbent is first dried to a constant weight and then placed into the adsorber. Nitrogen at a flow rate of 2 dm^3/min is introduced into the adsorber, and the chamber temperature is set to 393 K. After a complete regeneration, indicated by the IC spectrometer, an adsorption step begins.
2. **Adsorption (breakthrough experiment)**: initially, a stream of nitrogen passes through the adsorber, which is set to the working overpressure (2 or 5 bar). The temperature in the chamber is reduced to the desired adsorption temperature, which was set to 283, 293, 303 or 313 K. After the temperature in the adsorbent layer has stabilised, the inert gas is changed to the simulated flue gas. It consists of 13 vol. % of CO_2 balanced by synthetic air. The adsorption phase ends when the CO_2 concentrations at the inlet and outlet of the adsorber are equal. This state indicates an adsorption equilibrium when the adsorption capacity of CO_2 at a given pressure, q_i^* $\left[\mathrm{g}_{\mathrm{CO_2}}/\mathrm{g}_{\mathrm{dry\ adsorbent}}\right]$, is reached. Blank experiments have been carried out using inert material (glass beads of the same total volume as the real sample) prior to CO_2 adsorption. The blank curves are shown in Figure 5.
3. **Desorption**: the desorption was carried out at atmospheric pressure and elevated temperature (i.e., PTSA cycle). Once the CO_2 is released from the solid phase, the column is purified by N_2 or any other non-reactive gas (if CO_2 is used as a purifying gas, which is a common practice in the industry to maintain maximum purity of the product, it is not possible to use the IR spectrometer).

2.4. Mathematical modeling of breakthrough data

The breakthrough experiment was described by a one-dimensional plug-flow mathematical model in a packed-bed with the following assumptions:

1. The gas is a binary mixture of CO_2 and N_2 and behaves according to the ideal gas law (O_2, contained in the synthetic air, has similar adsorption characteristics as N_2, because its affinity towards Zeolite 13X is more-or-less equal to the affinity of N_2, thus both gases adsorb weakly [27]; the literature generally provides expressions for binary diffusion, the

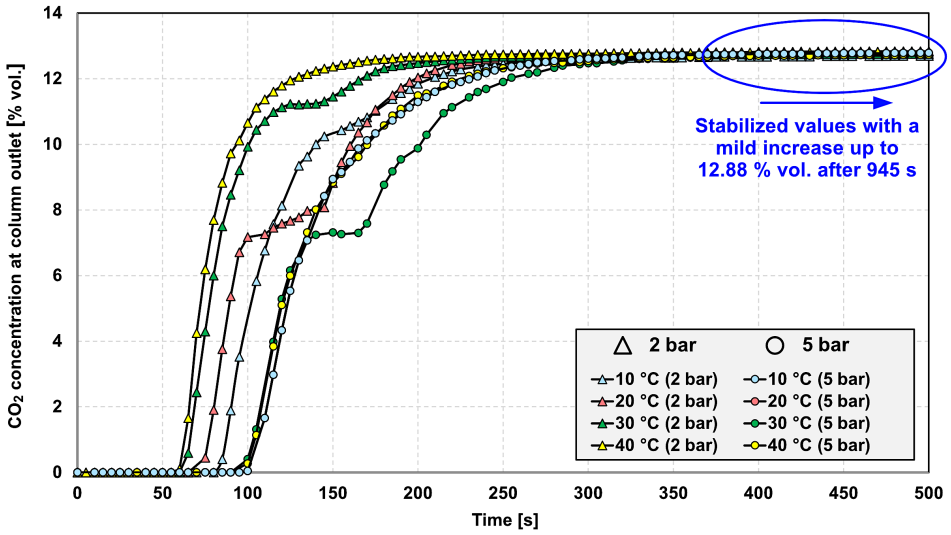

FIGURE 5. Blank experiments performed prior to each measurement; operating conditions: $T = 10$ - $40\,^{\circ}\mathrm{C}$, $P = 2$, 5 bar. The time interval is shortened from about 1800 s to 500 s, when the CO_2 concentrations at the outlet are almost stable.

diffusion of gas mixtures with more components is less accurately predictable [28].).

2. The system is isothermal (without generation of adsorption heat) and adiabatic (heat loss to the outside environment is not considered).
3. The system is radially homogeneous without the occurrence of concentration, diffusion, and temperature radial gradients.
4. The change in kinetic and potential energies is negligible.
5. The physical properties of the gas mixture, such as adsorption enthalpy, density, diffusion coefficients, specific heat capacity, and dynamic viscosity, are constant.
6. The physical properties of the adsorbent as well as the bed porosity are uniform.
7. The mass transfer rate between the solid and gas phases is described by the linear driving force (LDF) model.
8. The adsorbent is fully regenerated at the beginning.
9. The pressure drop is negligible, and the interstitial velocity of the gas is assumed to be constant.

The ongoing adsorption process in our experimental setup differs from the real adsorption systems by the placement of the apparatus and by its configuration. The adsorption column is placed inside a thermally insulated chamber, which makes it possible to reach isothermal conditions after a few minutes from the start of the process. Normally, the temperature varies continuously with respect to the generated adsorption heat and the volumetric flow having a higher overall effect on the adsorption phase such as the propagation of the concentration front. By assuming isothermal conditions (assumption 2), the prediction error is thus reduced; we discuss its effect within the following Section. Assumptions 1, 3, 5, 6 and 7 simplify the phenomena, but their application is proven to be sufficient [29]. Assumption 8 characterizes the breakthrough experiment [30], or the first cycle in the adsorption systems, because subsequent cycles do not allow full adsorbent regeneration after the desorption, leading to a cyclic deterioration of the adsorption capacity. Adsorption of gases causes a different volumetric flow, i.e., velocity of the purified gas at the column outlet. However, due to the nearly constant pressure and the small amount of strongly adsorbable components, this effect is less significant [31]. The change in volumetric flow, which we measured experimentally and which will be discussed later, occurs only when CO_2 is detected at the outlet (adsorbent is, at this time, almost saturated) and dilutes the purified gas, that is, N_2.

Based on the assumptions, the system is described by two governing Equations (1) and (4). The mass balance equation for component i in the gas phase assumes advection-diffusion plug-flow and is defined as follows:

$$\frac{\partial c_i}{\partial t} = \frac{\partial}{\partial z}\left(D_{\mathrm{ax}}\frac{\partial c_i}{\partial z}\right) - u\frac{\partial c_i}{\partial z} - \rho_p\left(\frac{1-\varepsilon_b}{\varepsilon_b}\right)\frac{\partial q_i}{\partial t} \quad (1)$$

Where $c_i = (y_i P)/(RT)$ is the concentration in the gas phase $\left[\mathrm{mol/m^3}\right]$, u is the interstitial velocity [m/s], ρ_p is the adsorbent particle density $\left[\mathrm{kg/m^3}\right]$, and ε_b is the bed porosity. Bed porosity was calculated using a correlation proposed by [32], which takes into account the column dimensions and the mean particle size of the adsorbent d_p [m]:

$$\varepsilon_b \;=\; 0.373 + 0.917 \exp\left(-0.824\,\frac{D_{in}}{d_p}\right) \qquad (2)$$

An alternative would be a comparison of the gas flow rate before the gas enters the adsorbent and of the gas flow rate inside the adsorbent. In the experiments, this measurement was obtained only for a single experimental case, 283 K and 5 bar, and therefore, using an experimentally verified formula is more rigorous. This approach was also used for the determination of interstitial velocity.

The D_{ax} represents the axial dispersion coefficient of the gas mixture $\left[\mathrm{m}^2/\mathrm{s}\right]$, which is dominant in the axial direction at higher Reynolds numbers ($\mathrm{Re_p} > 10$) [33]. Radial gradients are neglected. A correlation of Edwards and Richardson (1970) incorporating Wicke's (1973) approximation of coefficient γ and Bischoff's (1969) expression of coefficient β was used. The calculation of the D_{ax} is described in detail in [30] for a packed-bed adsorption of CO_2:

$$D_{\mathrm{ax}} \;=\; \gamma \cdot D_{M,\,CO_2-N_2} \;+\; \frac{\mathrm{Pe}_\infty^{-1}\,(u \cdot d_p)}{1 \;+\; \dfrac{\beta \cdot \gamma \cdot D_{M,\,CO_2-N_2}}{u \cdot d_p}} \qquad (3)$$

The advantage of this equation is that it accounts for the size of the adsorbent particles by a function of limiting value of Péclet number, Pe_∞, which was calculated by [34] as $Pe_\infty = 6.7\,d_p$ for particle size of the adsorbent lesser than 0.25 cm.

The last term in Equation (1), a source term, represents a mass transfer of the adsorbate in the solid phase and is simplified by the LDF model [35] assuming that the mass accumulation of a component i in the adsorbent is proportional to the difference between the amount adsorbed at equilibrium q_i^* $\left[\mathrm{mol}/\mathrm{m}^3\right]$ (given by the equilibrium adsorption capacity of the adsorbent measured during the breakthrough experiments) and the mean value of the amount adsorbed in the adsorbent particle q_i $\left[\mathrm{mol}/\mathrm{m}^3\right]$:

$$\frac{\partial q_i}{\partial t} \;=\; k_i\,(q_i^* \;-\; q_i) \qquad (4)$$

The mass transfer coefficient of component i, k_i [1/s], is simplified to the resistance of mass transport by diffusion in macropores, which usually dominates in commercial zeolites that are purposely made to minimise micropore diffusion and depends on the r_p^2/d_p ratio. The resistance to gas permeation through the film layer around the adsorbent is usually insignificant [36]:

$$k_i \;=\; \frac{15\,D_{\mathrm{eff}}}{r_p^2} \cdot \frac{c_{\mathrm{in},\,i}}{\rho_p \cdot q^*_{\mathrm{in},\,i}} \qquad (5)$$

Where r_p is the adsorbent particle diameter [m], D_{eff} is an effective value of the diffusion coefficient $\left[\mathrm{m}^2/\mathrm{s}\right]$ and $c_{\mathrm{in},\,i}\,/q^*_{\mathrm{in},\,i}$ represents a dimensionless slope of the adsorption isotherm that must be used for adsorbent particles with homogeneous structure. Effective diffusion depends on the flow regime in the macropores, which is determined from the Knudsen number [37]. The diffusion transport in macropores in zeolites takes place in the transition area, where both mechanisms, Knudsen and molecular diffusions, play an equal role:

$$D_{\mathrm{eff}} \;=\; \frac{\varepsilon_p}{\tau}\left(\frac{1}{D_{M,\,CO_2-N_2}} \;+\; \frac{1}{D_K}\right)^{-1} \qquad (6)$$

A pore geometrical factor τ, tortuosity, ranges from approximately 2 to 3 in packed beds filled with a non-structured zeolite adsorbent [38], but a value of 3 was chosen [30]. The porosity of the adsorbent particle ε_p was calculated using both the estimated (ε_b) and the experimentally measured ($\rho_b,\ V_{\mathrm{pore}}$) values:

$$\varepsilon_p \;=\; \rho_p \cdot V_{\mathrm{pore}}, \qquad (7)$$

where ρ_p is the particle density $\left[\mathrm{kg}/\mathrm{m}^3\right]$ and V_{pore} is the volume of pores $\left[\mathrm{m}^3/\mathrm{kg}\right]$.

There are many correlations that can be applied to estimate the molecular diffusivity. An approximation by Fuller et al. (1969) was used, which, according to [28], provides high accuracy for the binary mixture of $CO_2 - N_2$:

$$D_{M,\,CO_2-N_2} \;=\; \frac{0.00143\,T^{\,1.75}}{P \cdot M_{CO_2-N_2}\left[\left(\sum \nu_{CO_2}\right)^{1/3} + \left(\sum \nu_{N_2}\right)^{1/3}\right]^2} \qquad (8)$$

Where P is the gas pressure [bar], T is the temperature [K], and ν is the molar volume of the gas phase $\left[\mathrm{m}^3/\mathrm{mol}\right]$. The Knudsen diffusivity of component i, D_K $\left[\mathrm{m}^2/\mathrm{s}\right]$, was approximated by the Derjaguin correlation [39]:

$$D_{K,\,i} \;=\; \frac{9}{13}\left(\frac{d_{\mathrm{pore}}}{3}\sqrt{\frac{8\,R\,T}{\pi \cdot M_i}}\right) \qquad (9)$$

Where d_{pore} is the pore diameter [m], R is the universal gas constant [J/(mol.K)] and M_i is the molar weight of component i [kg/mol]. The overall Knudsen diffusion, D_K $\left[\mathrm{m}^2/\mathrm{s}\right]$, of gas mixture was calculated as resistances connected in parallel.

The system of governing equations with fixed initial and boundary conditions was differentiated with respect to the axial axis z and the time t to obtain the concentration of CO_2 and N_2 in the gas phase and the adsorption rate in the solid phase. The adsorption is a dynamic process accompanied by step change of concentration caused by the decomposition of the transport mechanism from purely convective to convection and diffusion once the gas enters the unsaturated empty bed, hence the Danckwers boundary condition $D_{\mathrm{ax}}\left(\partial c_i\,(t,0^+)\,/\partial z\right) = u\left[c_i\,(t,0^+) - c_{i,\,\mathrm{in}}\,(t,0^+)\right]$ [40] for the column inlet was applied. A higher accuracy of approximation was achieved by using a higher

Surface characteristics	
BET surface area, S_{BET}	$511.65\ \mathrm{m^2/g}$
Total pore volume, V_{pore}	$3.317 \times 10^{-4}\ \mathrm{m^3/kg}$
Pore average diameter, d_{pore}	$3.33 \times 10^{-8}\ \mathrm{m}$
Breakthrough experiments	
Adsorption pressure, P	2, 5 bar
Adsorption temperature, T	283, 293, 303, 313 K
Volumetric flow, V	
→ 2 bar	$0.024 - 0.045\ \mathrm{m^3/h}$
→ 5 bar	$0.021 - 0.023\ \mathrm{m^3/h}$
CO_2 molar fraction, y_{CO_2}	0.13
Adsorption capacities, q^*	
→ 2 bar and 283, 293, 303, 313 K	0.1188, 0.1000, 0.0737, 0.0681 $\mathrm{g_{CO_2}/g_{sorbent}}$
→ 5 bar and 283, 293, 303, 313 K	0.1313, 0.1128, 0.0872, 0.0809 $\mathrm{g_{CO_2}/g_{sorbent}}$
Desorption pressure, P	1 bar
Desorption temperature, T	393 K

TABLE 2. Experimental results and model parameters.

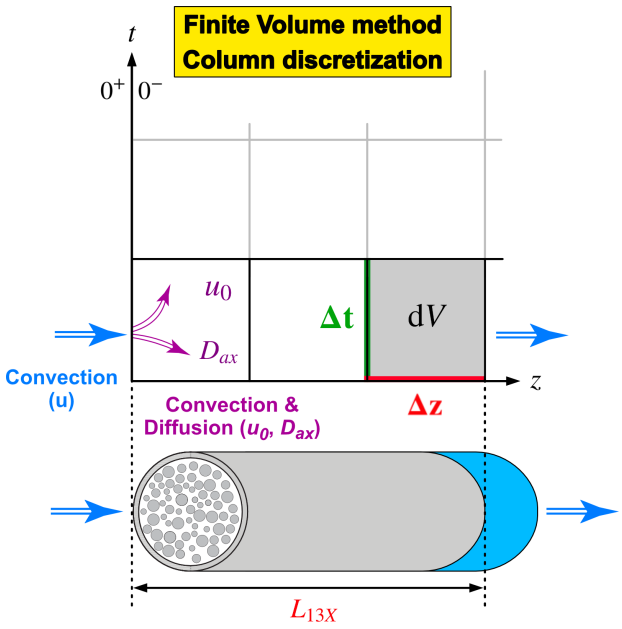

FIGURE 6. Schematic discretisation of the adsorption column using a finite volume method.

schemes with flux limiters recommended by [41] for a lumped kinetic model to ensure stability of the solution. A second-order TVD (total variation diminishing) explicit finite volume scheme was used, and equations were solved in MATLAB for the length step $\Delta z = 0.003\,\mathrm{m}$ and time step $\Delta t = 0.003\,\mathrm{s}$. The column discretisation into a series of control volumes $\mathrm{d}V$ along the axial axis z is shown in Figure 6. additional model parameters, which were obtained experimentally or by parameters estimation are specified in Table 2.

3. Results and discussion

3.1. Breakthrough experiments

The surface characteristics of the Zeolite 13X (BET surface area, S_{BET} $[\mathrm{m^2/kg}]$, and pore size distribution) were analyzed using a Coulter SA 3100 particle size analyzer. The measurement consisted of a pure nitrogen adsorption at 77 K, followed by determination of pore volumes from the obtained absorption isotherms. The results are listed in Table 2, together with the CO_2 adsorption capacities measured in the breakthrough experiments. The pore size distribution is shown in Figure 7.

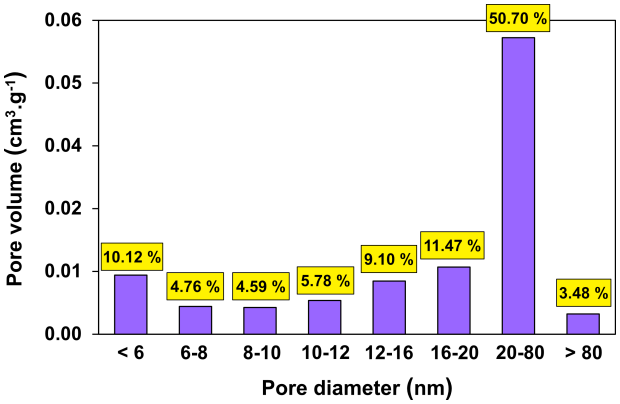

FIGURE 7. Pore size distribution.

BET analysis was also used to calculate the average size of the pores: $d_{\mathrm{pore}} = (4\,V_{\mathrm{pore}})\,/\,S_{\mathrm{BET}}$. Different mechanisms of mass transport in pores (pore size classification by IUPAC [42]) were not considered in diffusivities, and except for macropores ($> 50\,\mathrm{nm}$), all adsorbent pores were considered mesopores.

Each measurement of the breakthrough curve was carried out after 24 hours of desorption by degassing in an insulated reactor at 423 K.

A total of 5 cycles of adsorption and desorption at steady state were made for each temperature and pressure, as described in Section 2.3. The measured equilibrium adsorption capacities were averaged and summarised in the graph shown in Figure 8.

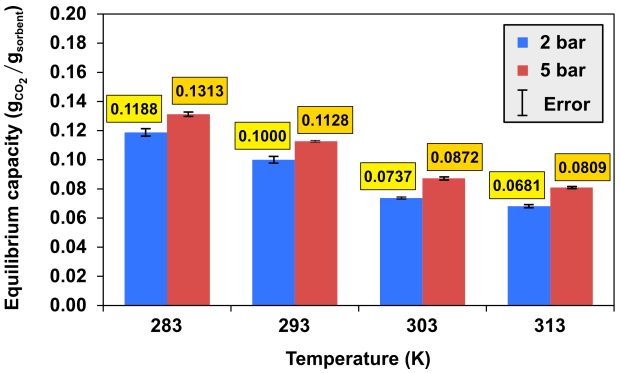

Figure 8. Adsorption capacities averages over cycles in each measurement.

A maximum variation for each individual adsorption pressure ranged from 0.97 % to 2.32 % at 2 bar, and 0.49 % to 1.20 % at 5 bar. The dependence of the magnitude of the error on the measurement conditions did not show a clear trend for adsorption temperature, but the average adsorption capacity varied more between cycles at the lower adsorption pressure, i.e., 2 bar. A possible explanation could be that higher pressures cause faster adsorption, as evidenced by the breakthrough curves measured at 5 bar (Figure 11). The adsorbate is, therefore, attracted by a greater force (van der Waals forces), which may result in a smaller deviation over a shorter period of time.

As expected, the commercial 13X molecular sieve sample showed the highest CO_2 adsorption capacities at high pressure and low temperature, that is, 0.1188 $g_{CO_2}/g_{sorbent}$ at 283 K and 2 bar and 0.1313 $g_{CO_2}/g_{sorbent}$ at 283 K and 5 bar. These conditions can be reached only when the water vapor is removed from the gas, which is a typical demand for zeolite-based adsorbents. In case the water vapor content is negligible or resistant adsorbent is used, lowering the flue gas temperature from 303 K to 293 K would improve the adsorption capacity of CO_2 the most. However, if the temperature of the flue gas containing a high amount of water vapor is around 303 K, it is due to consider adsorption at higher temperature, where the adsorption capacity is no longer significantly reduced, but the need for dehydration may be eliminated.

Once most of the adsorbent is saturated, we observed that the volumetric flow gradually increased appropriately to the amount of non-adsorbed CO_2 present. An almost linear dependence between both curves is not surprising (see Figure 9); however, when comparing the price of a CO_2 sensor and the difficulty of concentration sensing against sensing of a mass-flow rate, it begs the question of whether a similar idea could be interpreted into, for example, multi-column systems where mass-flow meters could serve as indicators of CO_2 concentration at each outlet, detecting the permitted amount of CO_2 in the off-gas. Especially in the industry, the requirement is aimed at process control and management rather than at measuring precision. However, knowing the information about the change in CO_2 concentration at the outlet, one can inversely predict the off-gas volumetric flow-rate and hence its velocity and pressure drop absolute variation. Further use of such information could also be replicated in the simulation to estimate, for example, the growth of axial dispersion in a system without pressure loss. However, the prediction error rate would require a deeper analysis.

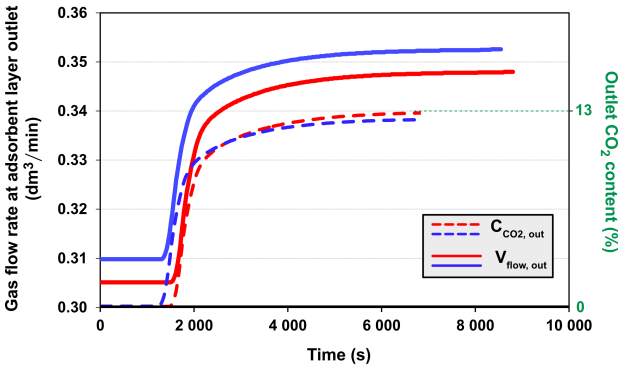

Figure 9. Experimentally measured values of volumetric flow and of CO_2 concentration at the column outlet. The curves shown have the highest deviation of values measured at 283 K and 5 bar.

3.2. Simulation results

The model parameters that were obtained by the adsorbent classification and breakthrough experiments or by using the aforementioned correlations are presented in Table 2, the rest of the input values can be found in Table 1.

The breakthrough curve modelling had to deal with incomplete experimental data, because the CO_2 adsorption isotherm was not measured. Its impact on the breakthrough curve is significant, as it influences the mass transfer rate coefficient representing the magnitude of the adsorption rate and defines the affinity of the adsorbate species towards the adsorbent (maximum adsorption amount at equilibrium was known). Generally, there are fewer experimental data available at higher pressures, and each of them usually differs in the sorbent used (for example, manufacturer, the Si/Al ratio, the framework structure, etc.). The interested reader is referred to, e.g., study by Hefti et al. [43] and summary within, or to the *NIST ARPA-E* [44] database currently containing 35 studies with CO_2 adsorption isotherms up to 5 bar. Due to the aforementioned diversity of adsorbent samples, making it difficult to replicate other data on the 13X sample tested in our study, we decided to follow the approach

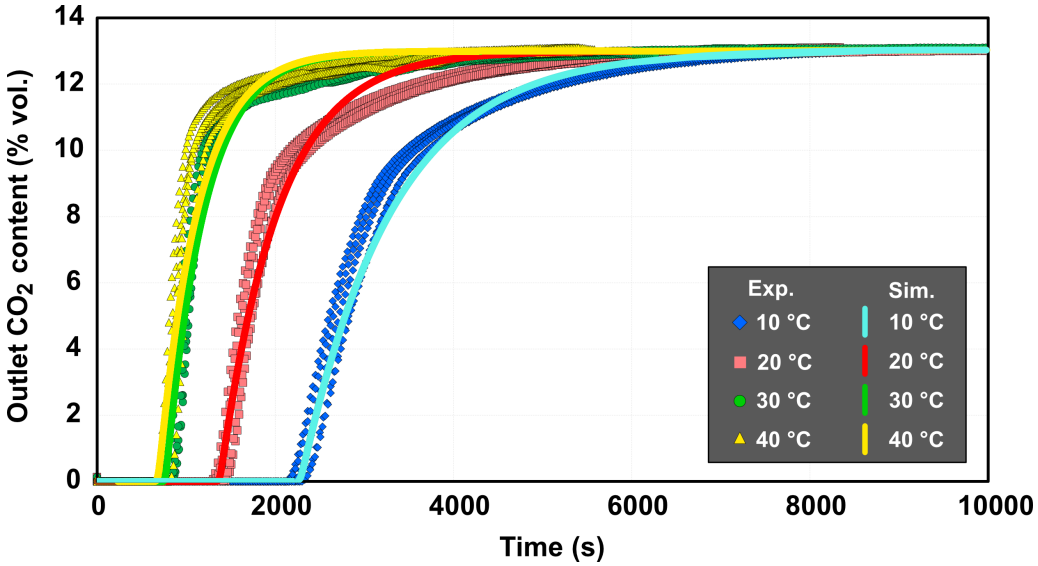

FIGURE 10. Comparison between the experimentally measured breakthrough curves and curves obtained by the simulation at 283, 293, 303 and 313 K, and 2 bar. *Note:* Exp. = Experiment; Sim. = Simulation; the curves obtained by the simulation are ploted in the black, and green, respectively, for the 30 °C.

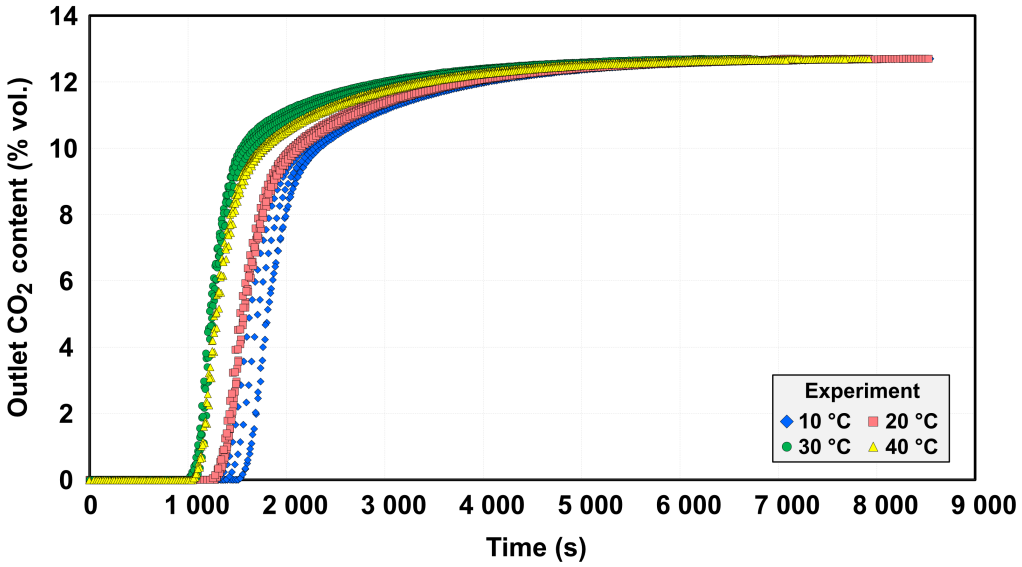

FIGURE 11. Experimentally measured breakthrough curves at 283, 293, 303 and 313 K, and 5 bar.

used by [45] and fit parameters of a single-site Langmuir isotherm:

$$q_i^* = \frac{q_{\text{sat}} \cdot b_i \cdot c_i}{1 + b_{\text{CO}_2} \cdot c_{\text{CO}_2} + b_{\text{N}_2} \cdot c_{\text{N}_2}} \qquad (10)$$

The use of the single-site Langmuir isotherm may look like a simplification because more complex models can better approximate the nonlinearity of CO_2 adsorption. For example, Bekhti et al. [46] compared 8 adsorption isotherm models for CO_2 on NaY zeolite up to 1 bar, and although the dual-site and the multi-site Langmuir isotherms had the smallest error, the single-site Langmuir isotherm was considered sufficient. We wanted to start with a simple model, which turned out to be sufficient even for higher pressures, despite the recommendation of Hefti et al. [43]. Using another model could raise the question of the number of fitting parameters, and therefore uncertainty, which is why we did not investigate other models. Such a comparison with the absence of the actual adsorption isotherm may be an interesting topic for further study.

We used a similar optimisation technique by changing the Langmuir equilibrium constant $b_{0,\,i}$ [m^3/mol], the internal energy ΔU_i [J/mol] (functions of an equilibrium constant b_i [m^3/mol]), while respecting the range of values for CO_2 and N_2 recommended by [45], and the maximum saturation capacity of the monolayer, q_{sat} [mol/kg]. The aim of this optimisation was to predict the breakthrough onset time by one-time adjustment of the adsorption isotherm within

the range of 5 experimentally measured isotherms at each of 4 cycles at 2 bar.

The fitting process was performed in MATLAB for 283 K. The best possible shape of the breakthrough curve was achieved by changing mostly the q_{sat}, $b_{0,\,CO_2}$ (ΔU_i remained constant, because of high sensitivity to the stability of the numerical solution in the region before the breakthrough occurred), and the flux limiter, which showed a high influence on the breakthrough curve slope. the following parameters were used:

$$\text{Fitting constraints} \begin{cases} q_{\mathrm{sat}} = 3.6 - 4.6 \\ b_{0,\,CO_2} = 2 - 2.5 \times 10^{-6} \\ \Delta U_{CO_2} = -35\,000 \\ \Delta U_{N_2} = -10\,000 \\ \text{Flux limiter: van Leer (1974)} \end{cases} \tag{11}$$

The "optimum solution" was obtained for $q_{\mathrm{sat}} = 3.7\,\mathrm{mol/m^3}$ and $b_{0,\,CO_2} = 2.1 \times 10^{-6}\,\mathrm{m^3/mol}$. The Langmuir constant for N_2 had a value of $b_{0,\,N_2} = 1.0 \times 10^{-6}\,\mathrm{m^3/mol}$. More details on calculating the single-site Langmuir adsorption parameters can be found in Pai et al. [45]. The breakthrough onset time correlated with a high degree of accuracy for other adsorption temperatures, 293, 303 and 313 K, while the fitting parameters remained constant. The region where the adsorption rate slows down as a result of high saturation of the adsorbent (the upper end of the curve) was accompanied by the highest deviation across the adsorption temperatures. An improvement was achieved by adapting the flux limiters used in the non-linear schemes, namely, van-Leer (1974) limiter instead of using the QUICK scheme.

Applying this approach, results can be generalised as follows:

- The prediction of the breakthrough onset time can be made with satisfying accuracy with 2 % maximum deviation from the experimental values (averaged over 5 cycles that were tested) across the range of adsorption temperatures. This also includes the area where the amount of 5 to 15 % of the inlet CO_2 concentration appears in the outlet, which would, in a real application, be an indication to terminate the adsorption process. The highest deviation was found for 283 K, where the predicted time for the occurrence of 15 % CO_2 from the inlet CO_2 concentration was 4.3 % (the deviation for 293 K was 0.2 %).
- To accurately predict the adsorbent utilisation efficiency (indicated by the slope of the breakthrough curve across its entire length) requires a deeper analysis of the parameters estimation and of the chosen numerical scheme. There is a relatively long-time interval before the breakthrough curve reaches its peak point because the change in the CO_2 concentration at the outlet decreases after approx. 75 % of the inlet CO_2 concentration. In our simulation, the deviation exceeded 10 % when the total amount of 90.2 % of CO_2 in the simulated gas (about 11.72 vol. % CO_2 relative to synthetic air) appeared at the outlet and the deviation continued to grow moderately. One of the possible explanations may be the negligence of the non-uniform generation of adsorption heat, i.e., exclusion of energy balance by assuming isothermal condition, or performing experiments in a rather small adsorption column (L_{col}/D_{in} ratio of 6.5), for which any change in temperature becomes more apparent relative to the breakthrough curve shape [47]. Results of Sircar (1983) [47] suggest a potentially higher correlation with our experimental data if the energy balance is accounted for (using temperature as a variable affecting both the adsorption rate and the equilibrium capacity results in a flattened curve plateau, i.e., long tail, until the feed concentration reaches the column outlet). Similar differences between isothermal and non-isothermal models using the LDF model for CO_2 adsorption were observed by [48]. On the contrary, Bollinini et al. (2012) [49] found the isothermal model relevant for lower flue gas velocities (higher velocities increase temperature); however, underlined the necessity of an appropriate value of the LDF mass transfer coefficient, k_i. Therefore, a follow-up study will be performed to confirm these claims as the objective of this study was to first verify the accuracy of predicting the breakthrough curve using a simple model.
  Theoretically, the CO_2 concentrations above, for example, 90 %, could be neglected, because they do not bring any significant improvement in the estimation of the adsorbent utilisation efficiency. However, using, e.g., a dimensionless factor π_1 proposed by [50] may be useful in this situation to ensure an "optimal" breakthrough curve steepness from the very beginning (recommended values of other criteria: Bi and π_2, proposed by the same authors, are usually satisfied for the fixed-bed adsorption). Furthermore, in a real process, it is unlikely that a similar amount of CO_2, at which our model showed the highest deviation, is allowed to be released in the atmosphere. Here, the inaccuracy of the isothermal model is significantly less important.

The experimental and simulation breakthrough curves are presented in Figure 10. The application of optimisation at 5 bar would be identical; hence Figure 11 shows only the experimental values.

3.3. Optimisation of the breakthrough curve prediction

Based on the differences between the experimental and simulation results, a sensitivity analysis was carried out to assess the accuracy of the prediction of the breakthrough onset time. Investigating the behaviour of the breakthrough curve in higher CO_2 outlet concentrations would be misleading in the sense that the

findings could not be directly applied to other temperatures as the breakthrough onset time. The approach was to assess parameters that are difficult to measure experimentally by nature, but the literature provides different ways of estimating them. For this purpose, a single breakthrough curve with the highest deviation (about 4 % from the original prediction) at 2 bar and 293 K was chosen, because it could represent a practical scenario in the CO_2 capture from the measured conditions.

First, it should be noted that the highest impact on the breakthrough onset time lies in the dimensions of the column and in the size of the adsorbent packing. For example, if the bed is fully filled with the zeolite 13X, achieving a breakthrough takes 51.6 % longer. Another obvious fact is that the breakthrough onset time decreases (and the curve becomes wider) with increasing volumetric flow. Second, the energy balance was not included in our model (discussed in Section 3.2), which partially limits the methodology of sensitivity analysis performed here. Sensitivity analysis was performed for 4 parameters:

- **Axial dispersion:** if the axial dispersion increases, the mixing of the gas molecules becomes more intensive, which results in an uneven adsorption and the breakthrough curve widens. Several correlations, chosen from [51], for the gas flow through the fixed bed packed with solid spherical particles were investigated. The values obtained were within the range of 3×10^{-5} m/s, and the breakthrough curve showed a negligible slope change. The highest difference was found between the correlations proposed by Edwards and Richardson (1968) and Wen-Fan (1975) with a difference of 1.62 % in the onset time.
- **Bed porosity**: it is proportional to the increase of the interstitial velocity, and therefore influences the axial dispersion. The estimation proposed by Ribeiro et al. [32] was in between the area of validity. Therefore, the calculation suggested by Dixon [52] for packed beds with regular spherical particles and a small ratio of the diameters of the column and the particles was analysed. The increase in the estimate of the bed porosity by approximately 14 % moved the results towards the experimentally obtained onset time by approx. 3.2 % and achieved the highest accuracy for the studied breakthrough curve (0.8 %; considering the average onset time for 2 bar, this change would also provide the best fit).
- **Mass transfer coefficient**: the mass transfer coefficient used in our model accounted for the transport resistance in macropores. As mentioned previously, commercial zeolites are made to minimise micropore diffusion; hence we have investigated whether the film layer slows down the gas penetration to a noticeable degree or whether the effect is negligible as suggested by [36]. An external mass transfer coefficient, k_f [m/s], with the [53] approximation of the Sherwood number, was included in the calculation of the overall mass transfer resistance. The obtained deviation of about 0.3 % confirmed the parameter's insignificance.
- **Molecular diffusion coefficient**: a less sensitive parameter. Any of the well-known expressions, e.g., Fuller et al. (1965), Wilke & Lee (1955) or Chapman-Enskog (1967), all contained in [28], provided almost identical results.

Lastly, the influence of the flux limiters was investigated. For this particular case, van-Leer (1974), Superbee (1986), and Koren (1993) achieved almost the same accuracy of 4 % (the highest of 3.8 % was achieved by the Superbee (1986) flux limiter). The highest difference between the numerical fluxes was observed for the less steep breakthrough curves, where van Leer (1974) provided the best interpretation of the upper end of the curve (Figure 10). The results of the sensitivity analysis of selected parameters are shown in Figure 12 - each case differs from the "original prediction" by only one investigated parameter.

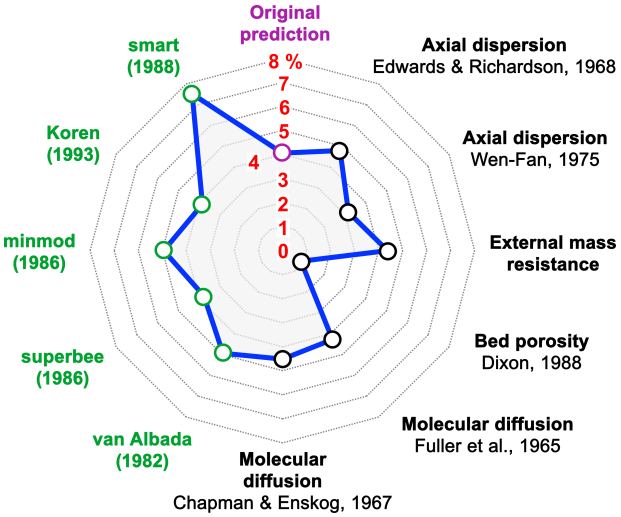

FIGURE 12. A deviation from the breakthrough curve onset time at 293 K and 2 bar. *Note:* Correlations were taken from [28, 34, 36, 41, 51–55].

4. CONCLUSIONS

Two sets of breakthrough experiments were performed at 2 and 5 bar at different temperatures in the laboratory adsorption apparatus, each for 5 cycles. The reported breakthrough curves showed no significant deviation between the cycles at each adsorption temperature, which established a solid ground for the simulation studies. The most prominent feature was the reduction of influence of the adsorption temperature on the amount adsorbed at 5 bar. Hence we can conclude that high-pressure system could provide a solution for processing wet gas stream by adsorbing CO_2 at elevated temperatures, above the dew point of the flue gas, without substantially lowering the amount adsorbed - a further research will be conducted in

this manner. Zeolite 13X possessed a high adsorption capacity at low pressures and temperatures below 293 K, while adsorption at high pressures did not provide significant advantages. The highest adsorption capacity of 0.1313 $\mathrm{g_{CO_2}}/\mathrm{g_{dry\ adsorbent}}$ was measured at 283 K and 5 bar and 0.1188 $\mathrm{g_{CO_2}}/\mathrm{g_{dry\ adsorbent}}$ at 283 K and 2 bar.

A quick assessment of the parameter optimisation makes the simulation a powerful tool that can save time, space, and financial funds once properly tuned with respect to the experiment. It was particularly evident for the breakthrough onset time, where the deviation did not exceed 2 % from the averaged experimental value. The prediction of the breakthrough curve tail, where the outlet CO_2 concentration reaches its plateau, yielded lower accuracy. A possible cause could be the assumption of isothermal conditions, which, in some studies, shortened the time of reaching the plateau of the breakthrough curve (i.e., steepened the breakthrough curve tail). Depending on the temperature rise during the adsorption, this effect appears to be more prominent and will be investigated further. Therefore, this area was not easy to investigate by the sensitivity analysis, which was therefore performed for the breakthrough onset time. The main conclusions can be summarised as follows:

- Column geometry, adsorption temperature and pressure, and volumetric flow are the easiest way to regulate adsorption time, by reducing or postponing the breakthrough onset time.
- The investigated parameters had a mild impact on the breakthrough onset time of up to 3.6 % from the original prediction. The bed porosity, which is defined by the adsorbent particle size and shape, bed configuration, and the type of packing, affects the largest number of parameters, and should always be accounted for.
- Non-linear numerical schemes are preferable for modelling adsorption processes.

Acknowledgements

This work was supported by the project TK03030167 "Low-emission technologies of energy conversion of biomass and alternative fuels" by the Technology Agency of the Czech Republic (TACR), which is gratefully acknowledged.

List of symbols

b, b_0 Langmuir equilibrium constant $[\mathrm{m^3/mol}]$
Bi Biot number [–]
c Concentration in the gas phase $[\mathrm{mol/m^3}]$
d_p Adsorbent particle diameter [m]
d_{pore} Adsorbent pore diameter [m]
D_{ax} Axial dispersion coefficient $[\mathrm{m^2/s}]$
D_{in} Bed inner diameter [m]
D_{eff} Effective diffusion coefficient $[\mathrm{m^2/s}]$
$D_K = \left(y_{CO_2}/D_{K,CO_2} + y_{N_2}/D_{K,N_2}\right)^{-1}$ Overall Knudsen diffusion $[\mathrm{m^2/s}]$
D_M Molecular diffusion coefficient $[\mathrm{m^2/s}]$
k Mass transfer rate [1/s]
$k_f = (\mathrm{Sh}\cdot D_{M,CO_2-N_2})/d_p$ External mass transfer rate [1/s]
L Length [m]
m_m Material weight [kg]
M Molar weight [mol/kg]
P Pressure [Pa, bar]
$\mathrm{Pe}_\infty = 6.7 d_p$ Péclet number (limiting value) [–]
r_p Particle diameter [m]
$R = 8.314$ Universal gas constant $[\mathrm{J/(mol\,K)}]$
$\mathrm{Re_p} = \rho_g\, u_0\, d_p/\mu_g$ Reynolds number for particle [–]
q Concentration in the solid phase $[\mathrm{mol/m^3}$, mol/kg$]$
q^* Adsorbed amount at equilibrium $\left[\mathrm{mol/m^3},\ \mathrm{g_{CO_2}}/\mathrm{g_{dry\ adsorbent}}\right]$
S_{BET} BET surface area $[\mathrm{m^2/kg}]$
Sh Sherwood number [–]
t Time [s]
t_w Column wall thickness, [m]
$u = u_0/\varepsilon_b$ Interstitial velocity [m/s]
u_0 Superficial velocity [m/s]
ΔU Internal adsorption energy [J/mol]
V_{flow} Volumetric flow $[\mathrm{dm^3/min}]$
V_m Material volume, Fig.1 $[\mathrm{m^3}]$
V_p Particle volume $[\mathrm{mm^3}]$
V_{pore} Pore volume $[\mathrm{m^3/kg}]$
$y_i = c_i/c$ Dimensionless concentration in the gas phase [–]
z Axial coordinate of the column [–]

β, γ Coefficients, Eq. 2 [–]
ε_b Bed porosity [–]
ε_p Particle porosity [–]
μ_g Gas dynamic viscosity [Pa S]
ν Molar volume of gas $[\mathrm{m^3/mol}]$
$\pi_1 = (u_0\,\varepsilon_p\, d_p^2\,\varepsilon_b)/[4\,L_{col}\,D_{eff}\,(1-\varepsilon_b)]$ $\Pi - 1$ factor [–]
π_2 $\Pi - 2$ factor [–]
ρ_g Gas density $[\mathrm{kg/m^3}]$
$\rho_p = \rho_b/(\varepsilon_b - 1)$ Particle density $[\mathrm{kg/m^3}]$
τ Tortuosity [–]

0^+ Position right after the column inlet
0^- Position right before the column inlet
$_{13X}$ Adsorbent bed of zeolite 13X
$_{col}$ Column
$_{emp}$ Empty space
$_{gb}$ Inert material (glass beads), Tab 1
$_i$ i-th component
$_{in}$ Column inlet
$_m$ Material
$_p$ Particle
$_{sat}$ State of adsorbent saturation
$_w$ Column wall

References

[1] D. Coe, W. Fabinski, G. Wiegleb. The Impact of CO2, H2O and Other "Greenhouse Gases" on Equilibrium

Earth Temperatures, *International Journal of Atmospheric and Oceanic Sciences* **5**(2):29-40, 2021. https://doi.org/10.11648/j.ijaos.20210502.12.

[2] M. Menner, G. Reichert. *EU Climate Policy in Light of the Corona Crisis*. cepInput. No. 18, 2020. https://www.cep.eu/fileadmin/user_upload/cep.eu/Studien/cepInput_Klima_und_Corona/cepInput_EU_Climate_Policy_in_Light_of_the_Corona_Crisis_01.pdf.

[3] S. E. Zanco, J.-F. Pérez-Calvo, A. Gasós, et al. Postcombustion CO2 Capture: A Comparative Techno-Economic Assessment of Three Technologies Using a Solvent, an Adsorbent, and a Membrane. *ACS Engineering Au* **1**(1):50-72, 2021. https://doi.org/10.1021/acsengineeringau.1c00002.

[4] M. M. F. Hasan, R. C. Baliban, J. A. Elia, et al. Modeling, Simulation, and Optimization of Postcombustion CO2 Capture for Variable Feed Concentration and Flow Rate. 1. Chemical Absorption and Membrane Processes. *Industrial & Engineering Chemistry Research* **51**(48):15642-64, 2012. https://doi.org/10.1021/ie301571d.

[5] M. M. F. Hasan, R. C. Baliban, J. A. Elia, et al. Modeling, Simulation, and Optimization of Postcombustion CO2 Capture for Variable Feed Concentration and Flow Rate. 2. Pressure Swing Adsorption and Vacuum Swing Adsorption Processes. *Industrial & Engineering Chemistry Research* **51**(48):15665-82, 2012. https://doi.org/10.1021/ie301572n.

[6] C. Song, Q. Liu, N. Ji, et al. Alternative pathways for efficient CO2 capture by hybrid processes - A review. *Renewable and Sustainable Energy Reviews* **82**:215-31, 2018. https://doi.org/10.1016/j.rser.2017.09.040.

[7] T. Zarogiannis, A. I. Papadopoulos, P. Seferlis. Systematic selection of amine mixtures as post-combustion CO2 capture solvent candidates. *Journal of Cleaner Production* **136**:159-75, 2016. https://doi.org/10.1016/j.jclepro.2016.04.110.

[8] M. Sheng, S. Dong, Z. Qiao, et al. Large-scale preparation of multilayer composite membranes for post-combustion CO2 capture. *Journal of Membrane Science* **636**, 2021. https://doi.org/10.1016/j.memsci.2021.119595.

[9] N. Fouladi, M. A. Makarem, M. A. Sedghamiz, et al. CO2 adsorption by swing technologies and challenges on industrialization. In *Advances in Carbon Capture*, p. 241-67. 2020. https://doi.org/10.1016/b978-0-12-819657-1.00011-6.

[10] C. Dhoke, A. Zaabout, S. Cloete, et al. Review on Reactor Configurations for Adsorption-Based CO2 Capture. *Industrial & Engineering Chemistry Research* **60**(10):3779-98, 2021. https://doi.org/10.1021/acs.iecr.0c04547.

[11] F. Raganati, R. Chirone, P. Ammendola. CO2 Capture by Temperature Swing Adsorption: Working Capacity As Affected by Temperature and CO2 Partial Pressure. *Industrial & Engineering Chemistry Research* **59**(8):3593-605, 2020. https://doi.org/10.1021/acs.iecr.9b04901.

[12] K. N. Son, T.-M. J. Richardson, G. E. Cmarik. Equilibrium Adsorption Isotherms for H2O on Zeolite 13X. *Journal of Chemical & Engineering Data* **64**(3):1063-71, 2019. https://doi.org/10.1021/acs.jced.8b00961.

[13] F. Raganati, F. Miccio, P. Ammendola. Adsorption of Carbon Dioxide for Post-combustion Capture: A Review. *Energy & Fuels* **35**(16):12845-68, 2021. https://doi.org/10.1021/acs.energyfuels.1c01618.

[14] D. Danaci, M. Bui, N. Mac Dowell, et al. Exploring the limits of adsorption-based CO2 capture using MOFs with PVSA - from molecular design to process economics. *Molecular Systems Design & Engineering* **5**(1):212-31, 2020. https://doi.org/10.1039/c9me00102f.

[15] P. Ammendola, F. Raganati, R. Chirone, et al. Fixed bed adsorption as affected by thermodynamics and kinetics: Yellow tuff for CO2 capture. *Powder Technology* **373**:446-58, 2020. https://doi.org/10.1016/j.powtec.2020.06.075.

[16] D. Bahamon, A. Díaz-Márquez, P. Gamallo, et al. Energetic evaluation of swing adsorption processes for CO 2 capture in selected MOFs and zeolites: Effect of impurities. *Chemical Engineering Journal* **342**:458-73, 2018. https://doi.org/10.1016/j.cej.2018.02.094.

[17] A. A. Abd, S. Z. Naji, A. S. Hashim, et al. Carbon dioxide removal through physical adsorption using carbonaceous and non-carbonaceous adsorbents: A review. *Journal of Environmental Chemical Engineering* **8**(5), 2020. https://doi.org/10.1016/j.jece.2020.104142.

[18] J. A. A. Gibson, E. Mangano, E. Shiko, et al. Adsorption Materials and Processes for Carbon Capture from Gas-Fired Power Plants: AMPGas. *Industrial & Engineering Chemistry Research* **55**(13):3840-51, 2016. https://doi.org/10.1021/acs.iecr.5b05015.

[19] M. Xu, S. Chen, D.-K. Seo, et al. Evaluation and optimization of VPSA processes with nanostructured zeolite NaX for post-combustion CO2 capture. *Chemical Engineering Journal* **371**:693-705, 2019. https://doi.org/10.1016/j.cej.2019.03.275.

[20] D. Sachde, R. McKaskle, J. Lundeen, et al. Review of Technical Challenges, Risks, Path Forward, and Economics of Offshore CO2 Transportation and Infrastructure. *Offshore Technology Conference, Houston, Texas, USA, 6 - 9 May 2019*, 2019. https://doi.org/10.4043/29253-MS.

[21] S. G. Subraveti, S. Roussanaly, R. Anantharaman, et al. Techno-economic assessment of optimised vacuum swing adsorption for post-combustion CO2 capture from steam-methane reformer flue gas. *Separation and Purification Technology* **256**, 2021. https://doi.org/10.1016/j.seppur.2020.117832.

[22] M. Nait Amar, H. Ouaer, M. Abdelfetah Ghriga. Robust smart schemes for modeling carbon dioxide uptake in metal-organic frameworks. *Fuel* **311**, 2022. https://doi.org/10.1016/j.fuel.2021.122545.

[23] A. H. Farmahini, S. Krishnamurthy, D. Friedrich, et al. Performance-Based Screening of Porous Materials for Carbon Capture. *Chemical Reviews* **121**(17):10666-741, 2021. https://doi.org/10.1021/acs.chemrev.0c01266.

[24] S. Li, S. Deng, L. Zhao, et al. Mathematical modeling and numerical investigation of carbon capture by adsorption: Literature review and case study. *Applied Energy* **221**:437-49, 2018. https://doi.org/10.1016/j.apenergy.2018.03.093.

[25] B. Miklová, M. Staf, V. Kyselová. Influence of ash composition on high temperature CO2 sorption. *Journal of Environmental Chemical Engineering* **7**(2), 2019. https://doi.org/10.1016/j.jece.2019.103017.

[26] J. Zhang, P. Xiao, G. Li, et al. Effect of flue gas impurities on CO2 capture performance from flue gas at coal-fired power stations by vacuum swing adsorption. *Energy Procedia* **1**(1):1115-22, 2009. https://doi.org/10.1016/j.egypro.2009.01.147.

[27] P. Xiao, J. Zhang, P. Webley, et al. Capture of CO2 from flue gas streams with zeolite 13X by vacuum-pressure swing adsorption. *Adsorption* **14**(4-5):575-82, 2008. https://doi.org/10.1007/s10450-008-9128-7 .

[28] B. E. Poling, J. M. Prausnitz, J. P. O'Connell. *The Properties of Gases and Liquids, 5th ed.* McGraw-Hill Education, 768 p, 2001. ISBN 9780071499996.

[29] M. S. Shafeeyan, W. M. A. Wan Daud, A. Shamiri. A review of mathematical modeling of fixed-bed columns for carbon dioxide adsorption. *Chemical Engineering Research and Design* **92**(5):961-88, 2014. https://doi.org/10.1016/j.cherd.2013.08.018.

[30] N. S. Wilkins, A. Rajendran, S. Farooq. Dynamic column breakthrough experiments for measurement of adsorption equilibrium and kinetics *Adsorption* **27**(3):397-422, 2020. https://doi.org/10.1007/s10450-020-00269-6.

[31] A. Malek, S. Farooq, M. N. Rathor, et al. Effect of velocity variation due to adsorption-desorption on equilibrium data from breakthrough experiments. *Chemical Engineering Science* **50**(4):737-40, 1995. https://doi.org/10.1016/0009-2509(94)00245-m.

[32] A. Ribeiro, P. Neto, C. Pinho. Mean porosity and pressure drop measurements in packed beds of monosized spheres: side wall effects. *International Review of Chemical Engineering*, **2**(1):40-46, 2010.

[33] J. M. P. Q. Delgado. Longitudinal and Transverse Dispersion in Porous Media. *Chemical Engineering Research and Design* **85**(9):1245-52, 2007. https://doi.org/10.1205/cherd07017.

[34] G. Langer, A. Roethe, K. P. Roethe, et al. Heat and mass transfer in packed beds-III. Axial mass dispersion. *International Journal of Heat and Mass Transfer* **21**(6):751-9, 1978. https://doi.org/10.1016/0017-9310(78)90037-6.

[35] E. Glueckauf, J. I. Coates. 241. Theory of chromatography. Part IV. The influence of incomplete equilibrium on the front boundary of chromatograms and on the effectiveness of separation. *Journal of the Chemical Society (Resumed)*, 1947. https://doi.org/10.1039/jr9470001315.

[36] D. M. Ruthven, M. F. M. Post. Chapter 12 Diffusion in zeolite molecular sieves. In *Introduction to Zeolite Science and Practice*, Studies in Surface Science and Catalysis, p. 525-77. 2001. https://doi.org/10.1016/s0167-2991(01)80254-8.

[37] K. Ciahotný, A. Vagenknechtová, M. Netušil, et al. Adsorption Drying of Natural Gas Under High Pressure. *Oil Gas European Magazine*, **40**(2):91-95, 2014.

[38] X. Hu, E. Mangano, D. Friedrich, et al. Diffusion mechanism of CO2 in 13X zeolite beads. *Adsorption* **20**(1):121-35, 2013. https://doi.org/10.1007/s10450-013-9554-z.

[39] S. Krishnamurthy, R. Blom, M. C. Ferrari, et al. Adsorption and diffusion of CO2 in CPO-27-Ni beads. *Adsorption* **26**(5):711-21, 2019. https://doi.org/10.1007/s10450-019-00162-x.

[40] P. V. Danckwerts. Continuous flow systems. *Chemical Engineering Science* **2**(1):1-13, 1953. https://doi.org/10.1016/0009-2509(53)80001-1.

[41] S. Javeed, S. Qamar, W. Ashraf, et al. Analysis and numerical investigation of two dynamic models for liquid chromatography. *Chemical Engineering Science* **90**:17-31, 2013. https://doi.org/10.1016/j.ces.2012.12.014.

[42] M. Thommes, K. Kaneko, A. V. Neimark, et al. Physisorption of gases, with special reference to the evaluation of surface area and pore size distribution (IUPAC Technical Report). *Pure and Applied Chemistry* **87**(9-10):1051-69, 2015. https://doi.org/10.1515/pac-2014-1117.

[43] M. Hefti, D. Marx, L. Joss, et al. Adsorption equilibrium of binary mixtures of carbon dioxide and nitrogen on zeolites ZSM-5 and 13X. *Microporous and Mesoporous Materials* **215**:215-28, 2015. https://doi.org/10.1016/j.micromeso.2015.05.044.

[44] D. W. Siderius, V. K. Shen, R. D. Johnson, et al. *NIST/ARPA-E Database of Novel and Emerging Adsorbent Materials*. National Institute of Standards and Technology, 2020. (Accessed 2022-05-06) https://doi.org/10.18434/T43882.

[45] K. N. Pai, V. Prasad, A. Rajendran. Practically Achievable Process Performance Limits for Pressure-Vacuum Swing Adsorption-Based Postcombustion CO2 Capture. *ACS Sustainable Chemistry & Engineering* **9**(10):3838-49, 2021. https://doi.org/10.1021/acssuschemeng.0c08933.

[46] H. Bekhti, H. Bouchafaa, R. Melouki, et al. Adsorption of CO2 over MgO-Impregnated NaY zeolites and modeling study. *Microporous and Mesoporous Materials* **294**, 2020. https://doi.org/10.1016/j.micromeso.2019.109866.

[47] S. Sircar, R. Kumar, K. J. Anselmo. Effects of column nonisothermality or nonadiabaticity on the adsorption breakthrough curves. *Industrial & Engineering Chemistry Process Design and Development* **22**(1):10-5, 2002. https://doi.org/10.1021/i200020a002.

[48] B. Berdenova, A. Pal, B. B. Saha, et al. Non-isothermal pore change model predicting CO2 adsorption onto consolidated activated carbon. *International Journal of Heat and Mass Transfer* **177**, 2021. https://doi.org/10.1016/j.ijheatmasstransfer.2021.121480.

[49] P. Bollini, N. A. Brunelli, S. A. Didas, et al. Dynamics of CO2 Adsorption on Amine Adsorbents. 1. Impact of Heat Effects. *Industrial & Engineering Chemistry Research* **51**(46):15145-52, 2012. https://doi.org/10.1021/ie301790a.

[50] I. Roušar, P. Ditl. Numerical Simulation of Multicomponent Isobaric Adsorption in Fixed Bed Columns. *Adsorption Science & Technology* **3**(2):49-59, 1986. https://doi.org/10.1177/026361748600300201.

[51] J. M. P. Q. Delgado. A critical review of dispersion in packed beds. Heat and Mass Transfer, 2005, 42(4), 279-310, https://doi.org/10.1007/s00231-005-0019-0.

[52] A. G. Dixon. Correlations for wall and particle shape effects on fixed bed bulk voidage. *The Canadian Journal of Chemical Engineering* **66**(5):705-8, 1988. https://doi.org/10.1002/cjce.5450660501.

[53] N. Wakao, T. Funazkri. Effect of fluid dispersion coefficients on particle-to-fluid mass transfer coefficients in packed beds. *Chemical Engineering Science* **33**(10):1375-84, 1978. https://doi.org/10.1016/0009-2509(78)85120-3.

[54] Ch. Tien. *Introduction to Adsorption*. Elsevier (S&T), 2019. ISBN 978-0-12-816446-4.

[55] G. D. Silcox, J. J. Noble, A. F. Saforim et al. Heat & Mass Transfer. In: *Don W. Green, Marylee Z. Southard. Perry's Chemical Engineers' Handbook, 9th Edition.* McGraw-Hill Education, p. 510-583, 2019. ISBN 978-0-07-183409-4.

ANALYSIS OF PARAMETERS IMPORTANT FOR INDIRECT DRYING OF BIOMASS FUEL

Michel Sabatini*, Jan Havlík, Tomáš Dlouhý

Czech Technical University in Prague, Faculty of Mechanical Engineering, Department of Energy Engineering, Technická 4, 166 07 Prague 6, Czech Republic

* corresponding author: michel.sabatini@fs.cvut.cz

Abstract. This paper focuses on biomass drying for the design and operation of an indirect dryer used in a biomass power plant. Indirect biomass drying is not as well described process as direct drying, especially when used for the preparation of biomass in energy processes, such as combustion or gasification. Therefore, it is necessary to choose a suitable model describing the drying process and evaluate its applicability for this purpose. The aim of this paper is to identify parameters that most significantly affect the indirect drying process of biomass for precise targeting of future experiments. For this purpose, the penetration model was chosen. The penetration model describes indirect drying through 21 parameters. To run a series of experiments focused on all parameters would be time consuming. Therefore, the easier way is to select the most important parameters through a sensitivity analysis, and then perform experiments focused only on the significant parameters The parameters evaluated as significant are the temperature of the heated wall, operating pressure in the drying chamber, surface coverage factor, emissivity of the heated wall, emissivity of the bed, diameter of the particle, and particle surface roughness. Due to the presumption of perfect mixing of the material being dried, stirrer speed is added into important parameters. Based on these findings, it will be possible to reduce the scope of experiments necessary to verify the applicability of the penetration model for the description of indirect biomass drying and the design of dryers for a practical use.

Keywords: Contact drying, indirect drying, penetration model, drying rate.

1. Introduction

Biomass as an energy source is an important component of the energy mix with respect to the departure from coal combustion and the established trend of using renewable energy sources. However, many kinds of biomass, e.g., wood chips, bark, or some agricultural residues, have a high moisture content that affects their energy use. The energy consumption for drying the biomass is significant. Therefore, it is important to dry biomass with the lowest possible energy intensity.

Biomass drying for power generation is commonly done in convective dryers, which are less energy-effective than indirect dryers. Therefore, replacing a convective dryer with an indirect dryer should result in energy savings. The difference between indirect (contact, conductive) and convective dryers is in the way how the heating medium supplies its heat to the material. In the case of direct dryers, the material being dried comes into a direct contact with the flow of the heating medium, which is most often air or flue gas. In the case of indirect dryers, a heating medium does not come into contact with the material being dried and the heat is transferred to the material through a heated wall of the dryer [1].

Indirect dryers are more energy effective because a lesser heat loss in the heating medium can be achieved. Moreover, any form of heat (e.g. waste heat) can be used for drying, which is particularly noticeable when using steam heating. In addition, the heat in water vapour produced during the drying can be recovered, for example, in the previous operation for pre-drying, and reduce the overall energy consumption of drying. The average energy consumption of indirect dryers is reported to be in the range of 2800–3600 kJ/kg while direct dryer's consumption is in the range of 4000–6000 kJ/kg [2, 3].

Many papers have been written on the subject of indirect drying for very specific materials and dryers. Based on these papers, there are two main models used for a description of indirect drying. The first of them is based on simultaneous heat, mass and momentum transfer in porous media given by Whitaker in [4, 5]. This model was used to investigate pharmaceutical materials dried in a laboratory vacuum dryer or in the Nutsche filter dryer in [6–11]. The second model is called the penetration model, the heat transfer of this model was described in [12] and then extended to be applicable for indirect drying in a pure vapour atmosphere in [13]. The following authors improved the penetration model for both the specific properties of the material and the specific drying conditions: for multigranular beds [14], for materials with hygroscopic behaviour [15–17], for granular beds wetted with a binary mixture [18], for indirect drying in the presence of an inert gas [17, 19]. In the paper [20], authors were taking into account the local kinetics of grain dehydration or the diffusion of vapour inside the bed to improve the model. Most of the previous

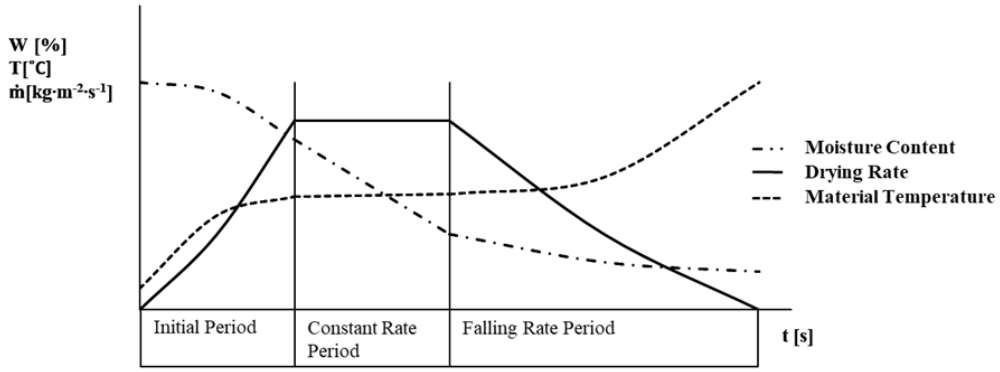

FIGURE 1. Schematic illustration of moisture content, drying rate, and material temperature.

articles were focused on the materials with a spherical shape. There are few other studies focused on different materials. Paste materials dried in LIST-type kneader dryer were examined in [21]. Drying of sewage sludge was studied in [22, 23]. Crystalline powders were the focus of studies [24, 25], and other types of powders in [26]. A comparison of the penetration model with the discrete modelling was done in [27]. Recent articles on indirect drying of biomass can be found in [28–30].

None of these studies aimed to describe the drying of biomass fuel in an indirect dryer using the penetration model. The novelty of the research is the modification and subsequent use of this model, because the model is derived and verified for materials with uniform shape and size and for conditions that are different from biomass, which has very inhomogeneous physical properties. The aim of this paper is to analyse the theoretical description of the biomass indirect drying process and to evaluate its applicability in the design of an indirect dryer for a biomass power plant. For a theoretical description of the indirect drying process, the penetration model can be used. To experimentally verify the model for the material and conditions corresponding to indirect drying of biomass, due to the large number of parameters that can influence the drying, many experiments would have to be done to determine the impact of each parameter on the drying process. Therefore, reducing the number of necessary experiments, through the sensitivity analysis of the drying process to changes in individual parameters was evaluated using the penetration model. The parameters with the greatest influence on the process were determined.

2. Materials and methods

2.1. Drying kinetics

The drying process consists of three main periods shown in Figure 1. In the initial period, both the temperature of the material and the drying rate rise rapidly. For the second period, a constant drying rate is typical. The temperature of the material rises very slowly and the moisture content decreases linearly. In the third period, the drying rate steadily decreases and the temperature of the material begins to increase fast. Biomass, as fuel, is usually being dried from a high moisture content to the level optimal for combustion, which is around $0.4\,\mathrm{kg_w\,kg_{dry}^{-1}}$. Drying of fuel takes place primarily in the initial and constant rate period. The initial period is usually short compared to the constant rate period, and it can be neglected. Moisture content is defined by equation (1).

$$X = \frac{m_w}{m_{dry}}, \tag{1}$$

where m_w [kg] is the weight of water and m_{dry} [kg] is the weight of dry matter.

2.2. Specifics of biomass fuel drying

Typical types of waste biomass used for a combustion are fresh wood chips and bark. Drying of wood chips or bark has some specifics. The material is usually very moist, the optimal target remaining moisture content after drying is about $0.4\,\mathrm{kg_w\,kg_{dry}^{-1}}$. Therefore, drying mostly takes place in the constant drying rate period. In this period, some of the parameters from the penetration model do not significantly affect its results, their influence increases only in the falling rate period. The identification of these negligible parameters can be done by a sensitivity analysis. Excluding them will reduce the scope of experiments required for the verification of the penetration model and evaluate its applicability for the description of contact drying of biomass.

2.3. Penetration model

The penetration model describes the heat and mass transfer during indirect drying. Thus, for specific conditions of the drying process, it is possible to theoretically calculate the heat transfer coefficient between the heated surface of the dryer and the material being dried, and subsequently determine the drying rate. The drying model was proposed by Schlünder and Mollekopf in [13]. The model is developed for drying mechanically agitated particulate materials in a pure

vapour atmosphere. The steady mixing process is substituted by a sequence of steps in which the material is stagnant for a fictitious period of time t_R and at the end of this period, the material is instantaneously and perfectly mixed. In the rest of the chapter, the model is briefly explained. A detailed explanation of the model can be found in the listed citation [12, 13]. The contact heat transfer coefficient can be calculated according to Schlünder [12]:

$$\alpha_{WS} = \varphi\alpha_{WP} + \alpha_{rad}, \tag{2}$$

where φ is the surface coverage factor (the heated surface which is in direct contact with the material), α_{WP} is the wall-particle heat transfer coefficient, α_{rad} is the heat transfer coefficient by radiation.

$$\alpha_{WP} = \frac{4\lambda_g}{d_{equiv}}\left[\left(1+\frac{2(l+\delta)}{d_{equiv}}\right)\cdot\ln\left(1+\frac{d_{equiv}}{2(l+\delta)}\right)-1\right], \tag{3}$$

where d_{equiv} [m] is the equivalent diameter of the particle:

$$d_{equiv} = \sqrt[3]{\frac{6V}{\pi}}, \tag{4}$$

where V [m^3] is the volume of the particle, λ_g is the thermal conductivity of the gas, and δ is the roughness of the particle surface.

$$\alpha_{rad} = 4\cdot C_{W,bed}\cdot T^3, \tag{5}$$

where T is the mean temperature, and $C_{W,bed}$ is the overall radiation coefficient calculated by:

$$C_{W,bed} = \frac{\sigma}{\left(\frac{1}{\varepsilon_W}+\frac{1}{\varepsilon_{bed}}-1\right)}, \tag{6}$$

where σ is the Stefan–Boltzmann constant, ε_W is the emissivity of the heated wall, and ε_{bed} is the emissivity of the bed.

The modified mean free path of the gas molecules l is defined as follows:

$$l = 2\cdot\frac{2-\gamma}{\gamma}\sqrt{\frac{2\pi\tilde{R}T}{\tilde{M}}}\frac{\lambda_g}{p\left(2c_{p,g}-\frac{\tilde{R}}{\tilde{M}}\right)}, \tag{7}$$

where γ is the accommodation coefficient, $\tilde{R}$ is the ideal gas constant, $\tilde{M}$ is the molecular weight of the gas, p is the operating pressure, and $c_{p,g}$ is the specific heat of the gas.

The penetration heat transfer coefficient of a dry bed can be expressed as:

$$\alpha_{bed,dry} = \frac{2}{\sqrt{\pi}}\frac{\sqrt{(p\lambda c)_{bed,dry}}}{\sqrt{t_R}}, \tag{8}$$

and of a wet bed as:

$$\alpha_{bed,wet} = \frac{\alpha_{bed,dry}}{\operatorname{erf}\zeta} = \frac{2}{\sqrt{\pi}}\frac{\sqrt{(p\lambda c)_{bed,dry}}}{\sqrt{t_R}}\frac{1}{\operatorname{erf}\zeta}, \tag{9}$$

where:

$$t_R = \frac{N_{mix}}{n}, \tag{10}$$

where for a paddle dryer, N_{mix} is calculated:

$$N_{mix} = 9\cdot Fr^{0.05}, \tag{11}$$

and Fr Froude number obtained from:

$$Fr = \frac{(2\pi n)^2\cdot D}{2g}, \tag{12}$$

where n is the stirrer speed, D is the diameter of the vessel, and g is the gravitational acceleration.

The reduced instantaneous position of the drying front ζ can be calculated from:

$$\zeta = \frac{z_T}{2\sqrt{\kappa_{bed,dry}t}}, \tag{13}$$

where $\kappa_{bed,dry}$ is the overall thermal diffusivity of the dry bed:

$$\kappa_{bed,dry} = \frac{\lambda_{bed,dry}}{(\rho c)_{bed,dry}}, \tag{14}$$

and ζ is determined from the relationship:

$$\sqrt{\pi}\cdot\zeta\cdot\exp\left(\zeta^2\right)\left[\left(\frac{\alpha_{WS}}{\alpha_{dry}}-1\right)\cdot\operatorname{erf}\zeta+1\right] = \frac{1}{\xi}\left(\frac{\alpha_{WS}}{\alpha_{dry}}-1\right), \tag{15}$$

where ξ is the reduced average moisture content of the bed:

$$\xi = \frac{X\Delta h_\nu}{c_{bed,dry}\cdot(T_W - T_{bed})}. \tag{16}$$

The overall heat transfer coefficient of a dry bed can be determined from the relation:

$$\frac{1}{\alpha_{dry}} = \frac{1}{\alpha_{WS}} + \frac{1}{\alpha_{bed,dry}}, \tag{17}$$

and of a wet bed from:

$$\frac{1}{\alpha} = \frac{1}{\alpha_{WS}} + \frac{1}{\alpha_{bed,wet}}. \tag{18}$$

The overall heat transfer coefficient α is expressed as follows:

$$\alpha = \frac{\alpha_{WS}}{1+\left(\frac{\alpha_{WS}}{\alpha_{dry}}-1\right)\cdot\operatorname{erf}\zeta}. \tag{19}$$

The flux at the hot surface:

$$\dot{q}_0 = \alpha(T_W - T_{bed}), \tag{20}$$

and the heat flux at the drying front:

$$\dot{q}_{lat} = \alpha(T_W - T_{bed})\cdot\exp\left(-\zeta^2\right) \tag{21}$$

The drying rate is obtained from:

$$\dot{m} = \frac{\dot{q}_{lat}}{\Delta h_\nu}. \tag{22}$$

The results of this step are differences in both the moisture content and the bed temperature (equations (23) and (24)), which serve to determine the new moisture content and the new bed temperature (equations (25) and (26)), which are inputs for the next step.

$$\Delta X = \frac{\dot{m} t_R A}{m_{dry}}, \tag{23}$$

where A is the covered surface of the heating wall depending mainly on the geometry of the dryer and the filling ratio.

$$\Delta T_{bed} = \Delta X \frac{\Delta h_\nu}{c_{bed,dry} + c_L X} \cdot [\exp / \zeta^2) - 1], \tag{24}$$

$$X_{i+1} = X_i + \Delta X_i, \tag{25}$$

$$T_{bed,i+1} = T_{bed,i} + \Delta T_{bed,i}. \tag{26}$$

The penetration model allows us to calculate the drying rate and the heat transfer coefficient, which are the main parameters needed for the design of an indirect dryer. Furthermore, the penetration model can predict the temperature of the material, which is important for drying temperature-sensitive materials.

2.4. Sensitivity analysis using penetration model for indirect drying of biomass

The aim of the sensitivity analysis of the penetration model is to determine the effect of the change in the v of individual input parameters on its overall heat transfer coefficient and drying rate. A large number of parameters enter into the calculation. For a practical use, under specific conditions, these parameters must be determined experimentally, often by very complex methods. Therefore, it is desirable to select parameters whose change has little effect on the results of the model, and their value can be determined in a simplified way or by estimation. High-sensitivity parameters can cause large variations in results even with a small change, so great care must be taken to determine their exact value. Based on the conclusions of the sensitivity analysis, it is possible to propose a precise plan for experiments for the model validation.

All parameters used in the penetration model for drying in a pure steam atmosphere were identified. In general, these parameters can be divided into three basic categories that describe the properties of the material, evaporated substance, and equipment.

Material properties: bed temperature, dry bed density, dry bed thermal conductivity, dry bed specific heat capacity, diameter of the particle, surface roughness of particles, bed emissivity, and moisture content.

Properties of evaporated substance: thermal conductivity, molar mass, operating pressure, specific heat capacity, latent heat, and accommodation coefficient.

Equipment properties: heated wall temperature, heated wall emissivity, surface coverage factor, stirrer speed, dryer diameter, and constants C and x.

Selection of analysed parameters: Some of the above parameters are defined for a specific material or device and usually cannot be changed, or their change depends on a change of other parameters, such as temperature or operating pressure. These parameters include the density of the dry bed of material, thermal conductivity of the dry bed, specific heat capacity of the dry bed, surface roughness of particles, thermal conductivity of the evaporated substance, molar mass of the evaporated substance, specific heat capacity of the evaporated substance and accommodation coefficient, emissivity of the heated wall, emissivity of the bed, surface coverage factor, diameter and length of the vessel, and moisture content. The moisture content of the material is usually specified and for this reason, it is also considered as an input parameter that cannot be changed. The parameters of the evaporated substance (in this case water) are determined from the steam tables.

However, the temperature of the heated wall, stirrer speed, operating pressure (if vacuum drying is applied), and associated temperature of the bed, and in some cases, also the diameter of the particle can be changed within a certain range according to the technological requirements. The constants C and x were determined by the authors of the model, and they are empirically determined parameters, for the purpose of this analysis, they are considered constant. However, the literature review showed that even these values are modified by some authors for more accurate results and therefore, it is possible to adjust them for specific equipment and materials [22].

Although it is not possible to change some of the parameters of the model, it is important to identify their influence and thus the importance of their exact determination. These parameters include the density of the dry bed, thermal conductivity of the dry bed, specific heat capacity of the dry bed, surface roughness of particles, emissivities of the heated wall and bed, surface coverage factor, and accommodation coefficient.

The sensitivity analysis is performed for the expected reference value of the parameter, and its value is usually changed in the range of ±50 %. In some cases, when an assumed change of a given parameter could make a difference, the range of the analysis is adjusted to cover probable conditions. A value of 100 % represents the reference case.

2.5. Reference case of indirect drying of biomass

The reference values of the parameters used in the sensitivity analysis are in Table 1. A horizontal paddle dryer is used, and the substance being evaporated is water. The chosen conditions represent both the material and the dryer, which will be used for future experiments and for validating the model for the purpose of biomass fuel drying. The drying of biomass fuel usually takes place under nearly atmospheric con-

Parameter		Unit	Value
diameter of the vessel	D	mm	256
length of the vessel	L	mm	1000
constant C	C	-	9
constant x	x	-	0.05
emissivity of the heated wall	ε_w	-	0.8
temperature of the heated wall	T_w	°C	130
operating pressure	p	bar	1.01325
stirrer speed	n	RPM	17
equivalent particle diameter	d_{equiv}	mm	10
density of the bed	ρ_{bed}	$\mathrm{kg\,m^{-3}}$	450
specific heat capacity of the bed	c_{bed}	$\mathrm{J\,kg^{-1}\,K^{-1}}$	1500
thermal conductivity of the bed	λ_{bed}	$\mathrm{W\,m^{-1}\,K^{-1}}$	0.18
emissivity of the bed	ε_{bed}	-	0.94
moisture content	X_0	$\mathrm{kg_w\,kg_{dry}^{-1}}$	1
accommodation coefficient	γ	-	0.8
surface coverage factor	φ	-	0.3
amount of dry matter	m_{dry}	kg	2.19
surface roughness of particles	δ	µm	500

Table 1. Reference case.

ditions. For the purpose of the analysis, drying at a lower pressure was also considered, which would increase the drying rate. Vacuum conditions allow using low-potential waste heat for drying, which would be otherwise lost. The benefit of using waste heat may overcome the energy required to run the vacuum pump.

3. Results and discussion

Results of the sensitivity analysis allow us to divide the input parameters of the model into significant and negligible according to how strongly they affect the drying process. The effect of changing the parameter on the size of the heat transfer coefficient from the heated wall to the material being dried and on the drying rate, which are the two most important parameters for the dryer design, was evaluated. The parameter was classified as significant if the change in the heat transfer coefficient or drying rate was greater than 3 % in the analysed range.

Low impact parameters According to Figure 2 and Figure 3, the parameters with little influence on both the heat transfer coefficient and the drying rate are usually material properties, such as the thermal conductivity of the material bed, heat capacity of the material bed, density of the material bed, and the accommodation coefficient, i.e., the parameter related to the properties of the evaporated substance. Changing these parameters has a negligible influence on the result of drying in the constant drying rate period. The last parameter is the stirrer speed, this parameter still needs to be verified experimentally, because one of the assumptions of the model is to achieve perfect mixing of the material, therefore, it is possible that the allowed speed range will be limited.

Strong impact parameters The following two figures show the strong influence of other parameters on the change of the heat transfer coefficient α and the drying rate. These parameters include temperature, operating pressure, diameter of the particle, emissivity of the heated wall, emissivity of the bed, surface roughness of particles, and surface coverage factor of the dryer. The greater the slope of the curve, the stronger the influence of the parameter. From the graph in Figure 4, it can be seen that the value of the heat transfer coefficient is most influenced by the surface coverage factor, temperature, emissivity, diameter of the particle, and surface roughness of particles. All of these parameters have a similar effect on the heat transfer coefficient. The influence of parameters on the change in drying rate is slightly different. Figure 5 shows the dominant effect of temperature. A smaller effect can be observed for the coverage, emissivity coefficients, and operating pressure. Lowering the pressure has a negative impact on the heat transfer coefficient, but a positive impact on the drying rate. The effect of roughness and particle diameter on the drying rate is weaker.

Overall evaluation The penetration model used to describe the heat transfer coefficient and the drying rate of contact drying works with 21 parameters. Ten of these parameters are related to the type of dryer and the evaporated substance, their value is determined by the specific circumstances of the case and cannot be easily changed. The remaining 11 parameters determine the properties of the material being dried and the conditions of the process that may be

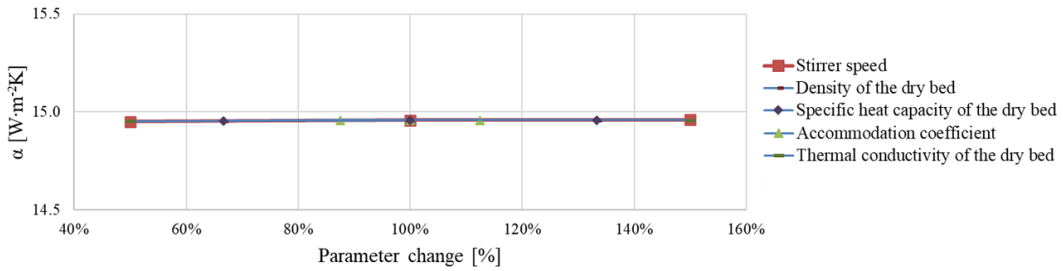

FIGURE 2. Parameters with low impact on the heat transfer coefficient.

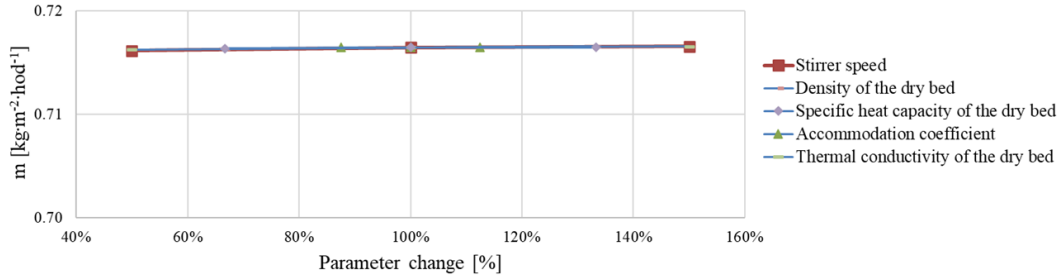

FIGURE 3. Parameters with low impact on the drying rate.

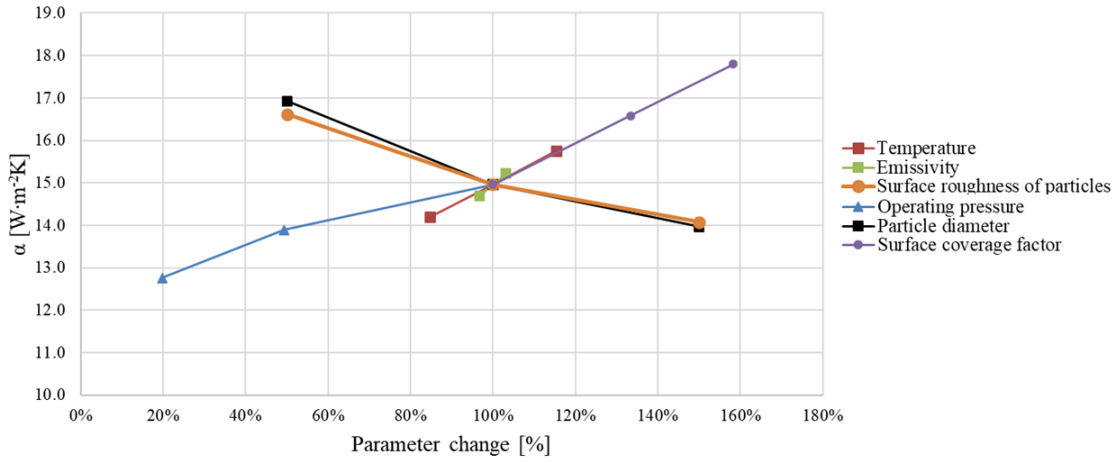

FIGURE 4. Parameters with strong impact on the heat transfer coefficient.

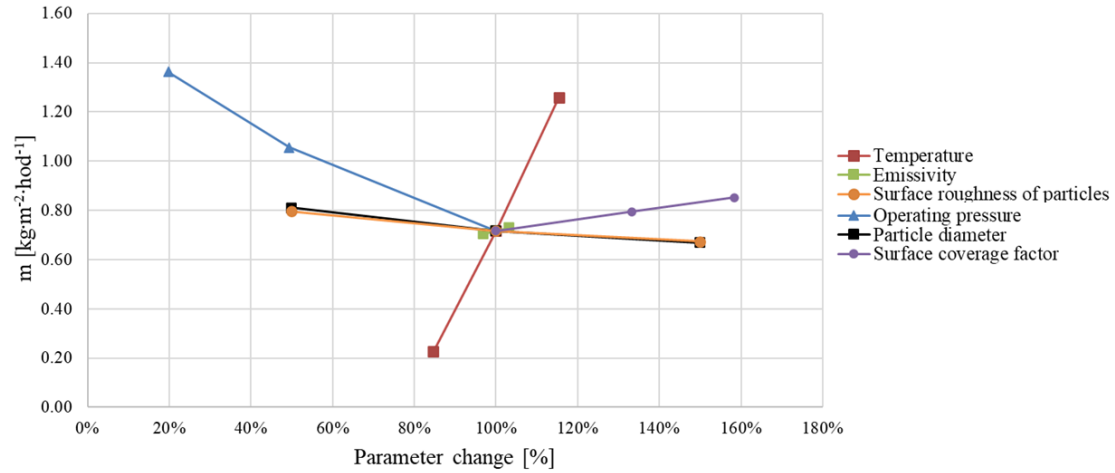

FIGURE 5. Parameters with strong impact on the drying rate.

variable or might be important for the drying. According to the results of the sensitivity analysis, only 7 of these parameters can significantly affect the drying process in the constant drying rate period. These parameters are – temperature of the heated wall, operating pressure, diameter of the particle, and other parameters that are important and it is necessary to determine them accurately. These parameters include the emissivity of the heated wall, emissivity of the bed of the material, surface coverage factor, and surface roughness of the particles. The penetration model assumes perfect mixing of the bed of material, therefore, it is desirable to also include stirrer speed among the important parameters and into a scheme of verification experiments. The influence of stirrer speed will probably be noticeable only at very low speeds.

4. Conclusion

The sensitivity analysis of the penetration model describing the heat transfer process in indirect dryers for the purpose of fuel drying has been done. For the drying process in the constant rate period, the most important parameters were identified. Changing them will be reflected in a significant change in the results of the model. In the case of using the penetration model to design a real biomass dryer, these parameters must be precisely determined within specific ranges that will correspond to the properties of the fuel and the required drying conditions. These parameters are the temperature of the heated wall, operating pressure, surface coverage factor, diameter of the particle, emissivity of the heated wall, emissivity of the bed, and surface roughness of particles. Moreover, it is recommended to include stirrer speed in a set of important parameters, especially at low stirrer speeds.

Future research will focus on the experimental verification of the use of the penetration model to describe the drying of biomass in an indirect dryer in order to validate its applicability for the design of real equipment.

List of symbols

A covered surface of the heating wall [m^2]
C constant [–]
c specific heat capacity [$\mathrm{J\,kg^{-1}\,K^{-1}}$]
$C_{W,bed}$ overall radiation coefficient [–]
c_p specific heat capacity at constant pressure [$\mathrm{J\,kg^{-1}\,K^{-1}}$]
D diamater of the vessel [m]
d_{equiv} equivalent particle diameter [m]
Fr Froude number [–]
g gravitational accelaration [$\mathrm{m\,s^{-2}}$]
Δh_ν latent heat of evaporation [$\mathrm{J\,kg^{-1}}$]
L lenght of the vessel [m]
m weight [kg]
$\dot{m}$ drying rate [$\mathrm{kg\,m^{-2}\,s^{-1}}$]
$\tilde{M}$ molar mass [$\mathrm{kg\,mol^{-1}}$]
n stirrer speed [RPM]
N_{mix} mixing number [–]
p operating pressure [Pa]
$\dot{q}$ heat flux [$\mathrm{W\,m^{-2}}$]
$\tilde{R}$ universal gas constant [$\mathrm{J\,mol^{-1}\,K^{-1}}$]
T temperature [K]
t_R contact time [s]
V volume of the particle [m^3]
X moisture content [$\mathrm{kg_w\,kg_d^{-1}ry}$]
x constant [–]
z_T position of the drying front [m]

Greek symbols

α heat transfer coefficient [$\mathrm{W\,m^{-2}\,K^{-1}}$]
γ accommodation coefficient [–]
δ surface roughness of particles [m]
ϵ emissivity [–]
ζ dimensionless position of phase change front [–]
l modified mean free path of gas molecules [m]
κ thermal diffusivity [$\mathrm{m^2\,s^{-1}}$]
λ thermal conductivity [$\mathrm{W\,m^{-1}\,K^{-1}}$]
ξ reduced average moisture content [–]
ρ density [$\mathrm{kg\,m^{-3}}$]
σ Stefan-Boltzmann constant [$\mathrm{W\,m^{-2}\,K^{-4}}$]
φ surface coverage factor [–]

Subscripts

$_0$ initial
$_{bed}$ bed of the material
$_{dry}$ dry matter
$_g$ gas
$_L$ liquid
$_{rad}$ radiation
$_W$ heated wall
$_w$ water
$_{wet}$ wet matter
$_{WP}$ wall-particle
$_{WS}$ contact

Acknowledgements

This work was supported by the project from Research Center for Low Carbon Energy Technologies, CZ.02.1.01/0.0/0.0/16_019/0000753. We gratefully acknowledge support from this grant.

References

[1] C. W. Hall. *Dictionary of drying.* Marcel Dekker, 1979. ISBN 9780824766528.

[2] A. S. Mujumdar. *Handbook of industrial drying.* CRC Press, 4th edn., 2014. https://doi.org/10.1201/b17208.

[3] M. Lattman, R. Laible. Batch drying: The "indirect" solution to sensitive drying problems. *Chemical Engineering (New York)* **112**(11):34–39, 2005.

[4] S. Whitaker. Simultaneous heat, mass, and momentum transfer in porous media: A theory of drying. In J. P. Hartnett, T. F. Irvine (eds.), *Advances in Heat Transfer*, vol. 13, pp. 119–203. Elsevier, 1977. https://doi.org/10.1016/S0065-2717(08)70223-5.

[5] S. Whitaker. Heat and mass transfer in granular porous media. In A. S. Mujumdar (ed.), *Advances in drying, vol. 1*, pp. 23–61. Hemisphere Publishing, New York, 1980.

[6] M. Kohout, A. P. Collier, F. Stepanek. Vacuum contact drying of crystals: Multi-scale modelling and experiments. In A. Barbosa-Póvoa, H. Matos (eds.), *Computer Aided Chemical Engineering*, vol. 18, pp. 1075–1080. Elsevier, 2004. https://doi.org/10.1016/S1570-7946(04)80245-1.

[7] M. Kohout, A. P. Collier, F. Stepanek. Vacuum contact drying kinetics: An experimental parametric study. *Drying Technology* **23**(9-11):1825–1839, 2005. https://doi.org/10.1080/07373930500209954.

[8] M. Kohout, A. Collier, F. Štěpánek. Microstructure and transport properties of wet poly-disperse particle assemblies. *Powder Technology* **156**(2-3):120–128, 2005. https://doi.org/10.1016/j.powtec.2005.04.007.

[9] M. Kohout, A. P. Collier, F. Štěpánek. Mathematical modelling of solvent drying from a static particle bed. *Chemical Engineering Science* **61**(11):3674–3685, 2006. https://doi.org/10.1016/j.ces.2005.12.036.

[10] M. Kohout, F. Stepanek. Multi-scale analysis of vacuum contact drying. *Drying Technology* **25**(7-8):1265–1273, 2007. https://doi.org/10.1080/07373930701438741.

[11] M. Murru, G. Giorgio, S. Montomoli, et al. Model-based scale-up of vacuum contact drying of pharmaceutical compounds. *Chemical Engineering Science* **66**(21):5045–5054, 2011. https://doi.org/10.1016/j.ces.2011.06.059.

[12] E. Schlünder. Heat transfer to packed and stirred beds from the surface of immersed bodies. *Chemical Engineering and Processing: Process Intensification* **18**(1):31–53, 1984. https://doi.org/10.1016/0255-2701(84)85007-2.

[13] E. Schlünder, N. Mollekopf. Vacuum contact drying of free flowing mechanically agitated particulate material. *Chemical Engineering and Processing: Process Intensification* **18**(2):93–111, 1984. https://doi.org/10.1016/0255-2701(84)85012-6.

[14] E. Tsotsas, E. Schlünder. Vacuum contact drying of free flowing mechanically agitated multigranular packings. *Chemical Engineering and Processing: Process Intensification* **20**(6):339–349, 1986. https://doi.org/10.1016/0255-2701(86)80012-5.

[15] E. Tsotsas, E. Schlünder. Vacuum contact drying of mechanically agitated beds: The influence of hygroscopic behaviour on the drying rate curve. *Chemical Engineering and Processing: Process Intensification* **21**(4):199–208, 1987. https://doi.org/10.1016/0255-2701(87)80017-X.

[16] R. Forbert, F. Heimann. Vacuum contact drying of mechanically agitated, coarse, hygroscopic bulk material. *Chemical Engineering and Processing: Process Intensification* **26**(3):225–235, 1989. https://doi.org/10.1016/0255-2701(89)80021-2.

[17] A. Gevaudan, J. Andrieu. Contact drying modelling of agitated porous alumina beads. *Chemical Engineering and Processing: Process Intensification* **30**(1):31–37, 1991. https://doi.org/10.1016/0255-2701(91)80006-B.

[18] F. Heimann, E. Schlünder. Vacuum contact drying of mechanically agitated granular beds wetted with a binary mixture. *Chemical Engineering and Processing: Process Intensification* **24**(2):75–91, 1988. https://doi.org/10.1016/0255-2701(88)87016-8.

[19] E. Tsotsas, E. Schlünder. Contact drying of mechanically agitated particulate material in the presence of inert gas. *Chemical Engineering and Processing: Process Intensification* **20**(5):277–285, 1986. https://doi.org/10.1016/0255-2701(86)80021-6.

[20] D. Farges, M. Hemati, C. Laguérie, et al. A new approach to contact drying modelling. *Drying Technology* **13**(5-7):1317–1329, 1995. https://doi.org/10.1080/07373939508917024.

[21] A. Dittler, T. Bamberger, D. Gehrmann, Ernst-Ulrich Schlünder. Measurement and simulation of the vacuum contact drying of pastes in a LIST-type kneader drier. *Chemical Engineering and Processing: Process Intensification* **36**(4):301–308, 1997. https://doi.org/10.1016/S0255-2701(97)00004-4.

[22] P. Arlabosse, T. Chitu. Identification of the limiting mechanism in contact drying of agitated sewage sludge. *Drying Technology* **25**(4):557–567, 2007. https://doi.org/10.1080/07373930701226955.

[23] J.-H. Yan, W.-Y. Deng, X.-D. Li, et al. Experimental and theoretical study of agitated contact drying of sewage sludge under partial vacuum conditions. *Drying Technology* **27**(6):787–796, 2009. https://doi.org/10.1080/07373930902900911.

[24] A. Michaud, R. Peczalski, J. Andrieu. Experimental study and modeling of crystalline powders vacuum contact drying with intermittent stirring. *Drying Technology* **25**(7-8):1163–1173, 2007. https://doi.org/10.1080/07373930701438501.

[25] A. Michaud, R. Peczalski, J. Andrieu. Modeling of vacuum contact drying of crystalline powders packed beds. *Chemical Engineering and Processing: Process Intensification* **47**(4):722–730, 2008. https://doi.org/10.1016/j.cep.2006.12.009.

[26] M. Intelvi, A. Picado, J. Martínez. Contact drying simulation of particulate materials: A comprehensive approach. In *7th International Conference on Chemical Engineering (ICCE 2011)*, vol. 59, pp. 1669–1676. 2011. https://doi.org/10.13140/RG.2.1.2632.6008.

[27] E. Tsotsas, M. Kwapinska, G. Saage. Modeling of contact dryers. *Drying Technology* **25**(7-8):1377–1391, 2007. https://doi.org/10.1080/07373930701439079.

[28] J. Havlík, T. Dlouhý, M. Sabatini. The effect of the filling ratio on the operating characteristics of an indirect drum dryer. *Acta Polytechnica* **60**(1):49–55, 2020. https://doi.org/10.14311/AP.2020.60.0049.

[29] M. Sabatini, J. Havlík, T. Dlouhý. Improving the efficiency of a steam power plant cycle by integrating a rotary indirect dryer. *Acta Polytechnica* **61**(3):448–455, 2021. https://doi.org/10.14311/AP.2021.61.0448.

[30] J. Havlík, T. Dlouhý. Indirect dryers for biomass drying—comparison of experimental characteristics for drum and rotary configurations. *ChemEngineering* **4**(1):1–11, 2020. https://doi.org/10.3390/chemengineering4010018.

EFFECT OF MEMBRANE SEPARATION PROCESS CONDITIONS ON THE RECOVERY OF SYNGAS COMPONENTS

Petr Seghman*, Lukáš Krátký, Tomáš Jirout

Czech Technical University, Faculty of Mechanical Engineering, Department of Process Engineering, Technická 4, Prague 6, 160 00, Czech Republic

* corresponding author: petr.seghman@fs.cvut.cz

Abstract. The presented study focuses on inspecting the dependency between process conditions, especially permeate and retentate pressure and component recovery of H_2, CO, and CO_2 during a membrane separation of model syngas. Experiments with both pure components and a model mixture were performed using a laboratory membrane unit Ralex GSU-LAB-200 with a polyimide hollow fibre module with 3000 hollow fibres. Permeability values were established at 1380 Barrer for H_2, 23 Barrer for CO, and 343 Barrer for CO_2. The measured selectivities differ from the ideal ones: the ideal H_2/CO_2 selectivity is 3.21, while the experimental values range from over 4 to as low as 1.2 (this implies that an interaction between the components occurs). Then, the model syngas, comprised of 16 % H_2, 34 % CO, and 50 % CO_2, was tested. The recovery of each component decreases with an increasing permeate pressure. At a pressure difference of 2 bar, the recovery rate for H_2, for a permeate pressure of 1.2 bar, is around 68 %, for 2.5 bar, the values drop to 51 %, and for 4 bar, the values reach 40 % only. A similar trend was observed for CO_2, with recovery values of 59 %, 47 % and 37 % for permeate pressures of 1.2 bar, 2.5 bar and 4 bar, respectively.

Keywords: Membrane separation, syngas improvement, components recovery, hollow fibre module.

1. Introduction

One of the main challenges for scientific teams in the past years has been finding a solution to mitigate climate change and decrease the production of CO_2 and greenhouse gases. In addition to other approaches, waste utilization is one of the most promising ways. Specifically, for biomass, gasification offers a suitable solution for the biomass-to-fuels and biomass-to-chemicals conversion. Many studies have shown that the product of gasification can be used as a feed for various downstream technologies, including Fischer-Tropsch synthesis, methanol production, and other processes that have been used for coal-gasification-produced syngas [1]. Taking into account the environment, many scientific teams have published innovative approaches, including syngas fermentation using specific bacteria [2]. As biosyngas (biomass gasification-produced syngas) contains H_2, CO, CO_2, and minor amounts of CH_4 and other components, it is necessary to adjust its composition and eventually remove the impurities before using it as feedstock for the mentioned technologies. Membrane operations are one of the possible solutions for such adjustments. To implement membrane operations in the technology process, it is necessary to describe the processes.

Currently, the focus of scientific teams researching membrane operations is on the separation of two components. Several studies have been published describing a two-component separation. Choi et al. [3] studied H_2/CO separation – the effect of the operating pressure was described for H_2:CO ratios of 3:1, 5:1 and 7:1 and showed that permeance increased with a higher H_2 concentration. The effects of increasing flow rate and operating pressure on separation factors and permeance. A study presented by Huang et al. [4] focuses on H_2 and CO_2 recovery and describes the dependency between the recovery of components and the area of the module. The article presents that it is necessary to increase the area near exponentially to achieve a lower CO_2 concentration in the retentate.

Besides the two-component separation, the scientific field of interest is the numerical simulation and the solution of multicomponent separation. A study published by Lee et al. [5] proposes a numerical model of multicomponent membrane separation for CO_2 containing mixtures in counter-current hollow fibre modules based on the Newton-Raphson method. The numerical solution was compared with the experimental data using a gaseous mixture consisting of 14 % CO_2, 6 % O_2, and 80 % N_2. Another approach to numerical modelling of membrane separation was presented by Qadir et al. [6] and involved fluid dynamics within CFD simulations. The study reflects different process parameters in the simulation; however, mainly binary mixtures were studied. Another similar paper on numerical modelling was presented by Alkhamis et al. [7], who proposed the dependence of Reynolds (Re) and Sherwood (Sh) numbers on the separation parameters during the CO_2 and CH_4 separation. Based on simulations, applications of the spacers in the inter-fibre space was recommended to increase the CO_2 separation efficiency. However, neither of the mentioned approaches offers an effective enough description of the processes. Also, there is not much data on the

membrane separation of H_2-CO-CO_2 and ev. CH_4 mixtures (syngas), and not many studies have been published. Therefore, our studies are focused on the syngas membrane separation and a further description of the processes.

The study's primary goal is to inspect the dependency between process conditions (specifically permeate and retentate pressure combination) and the separation process results represented by component recovery and or permeate and retentate concentrations. Experimental data for the H_2-CO-CO_2 mixture are published along with several observations and dependency descriptions for permeate composition dependency on stage cut and component recovery dependency on pressure conditions.

2. Materials and methods

All experiments were performed using the experimental setup, the defined model syngas mixture and the following equations for computation described further below.

2.1. Experimental equipment

Measurements were made using a laboratory membrane unit Ralex GSU-LAB-200 manufactured by MemBrain that allows a module exchange. The unit operates with pressures ranging from 1 to 10 bar in the retentate (and feed) branch, 1 to 5 bar in the permeate bar and is equipped with a temperature-regulating circuit that can maintain module temperature between room temperature and 60 °C. The measured values are pressure p_i, temperature T_i, and mass flow m_i in each branch (feed – F, retentate – R, permeate – P), and the temperature of the module coating T_S. The composition of each flow is measured using a gas analyser that switches between flows following a user-defined scheme. Figure 1 below shows a simple scheme of the measurement.

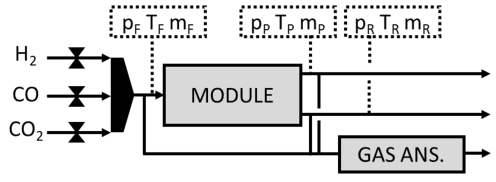

Figure 1. Scheme of measurement with indicated measured values. "Gas Ans." stands for the Gas analyser.

The module used in the study is a polyimide-polyetherimide hollow fibre module (manufactured by MemBrain, the exact mixture being kept a secret) consisting of 3000 hollow fibres with a diameter $D_e = 0.3$ mm, the thickness of the wall $W = 6$ µm and an active length of $L = 290$ mm, defining the total area of the module $S = 0.514\,\mathrm{m}^2$. The feed enters into the fibres; the retentate is collected from the end of the fibres, and the permeate from the inter-fibre space. The whole bundle of fibres is covered in a tube and equipped with flanges on both ends.

The laboratory unit is connected to the supply of pure gases, including H_2, CO, CO_2, and N_2 (used for washing before and after each measurement to maximize the measurement reliability).

2.2. Model gas and measurement conditions

For the experiments with pure gases, gas sources for hydrogen H_2 of 5.0 gas purity, carbon monoxide CO of 4.7 gas purity, and carbon dioxide CO_2 of 4.0 gas purity, were used. The model mixture representing the biomass-gasification-produced syngas was defined to contain 16 %mol H_2, 34 %mol CO and 50 %mol CO_2. The concentration of each component in the feed flow is defined by the feed molar flows for each gas directly using the membrane unit interface.

Based on the extensive literature study, the composition was chosen: The values represent the oxygen (or air) gasification from wood biomass. Biomass gasification using air as the agent and wood as feedstock produces syngas with composition varying in 10–20 %mol for H_2, 30–45 %mol for CO and 35–55 %mol for CO_2.

The model mixture was tested at approximately constant temperature $T_M = 22$ °C (with a deviation smaller than 1 °C). The feed gas flow rate was maintained at $100\,\mathrm{NL\,h^{-1}}$ ($4.464\,\mathrm{mol\,h^{-1}}$). The pressure conditions were defined by the permeate pressure varying at levels $p_P = 1$ bar, $p_P = 2.5$ bar and $p_P = 4$ bar. The total pressure difference ranged from 0.45 to 8 bar. (The lowest pressure difference was defined by the unit's limits and the module and was different for each pressure level.) The pressure conditions (permeate and retentate pressure) are defined within the unit interface and are maintained constant using an integrated regulation system.

2.3. Methods of data evaluation

The ideal gas behaviour was considered for all measurements (incl. pure component measurements). The ideal behaviour's deviation was estimated in the previous study and reached values smaller than 2 %, with an average below 1 % for all three components (H_2, CO and CO_2) and their mixtures.

Values acquired from experiments consist of pressure for each branch (permeate p_P, retentate p_R, feed p_F), mass flows of each branch, and composition of the flows (represented by the concentration of the components in %mol) and temperatures of the flows.

The value used to describe the ability to let the gases go through the membrane is the permeability P_i of each gas. The permeability is defined as the molar flow rate of gas permeating through a unit of area of the module per second caused by a unit of partial pressure difference of the module and can be described by the following equation (1):

$$P_i = \frac{n_i}{S \cdot \Delta p_i} W, \tag{1}$$

where P_i is the permeability of the component in $[\mathrm{mol\,m^{-1}\,s^{-1}\,bar^{-1}}]$, n_i is the molar flow in $[\mathrm{mol\,s^{-1}}]$, W is the thickness of the module wall in [m], S is the total surface of the fibres of the module in $[\mathrm{m^2}]$, and Δp_i is the partial pressure difference in [bar] (for pure components, the partial pressure difference is equal to the total pressure difference). The pressure difference is defined as the difference between the retentate and permeate pressure (resp. the i-th component's partial pressure). The commonly used unit for permeability is 1 Barrer, which is defined as follows:

$$1\,\mathrm{Barrer} = 3.35 \times 10^{-11}\,\mathrm{mol\,m^{-1}\,s^{-1}\,bar^{-1}}. \quad (2)$$

To calculate the molar flow of component i, the total molar flow in a stream must be calculated from the mass flow and the concentrations. Taking the ideal gas behaviour into consideration, the following equation can be used:

$$n_x = \frac{m_x}{\sum c_i \cdot M_i}, \quad (3)$$

where n_x is the total molar flow in branch x in $[\mathrm{mol\,s^{-1}}]$, m_x is the mass flow measured in branch x in $[\mathrm{g\,s^{-1}}]$, c_i is the molar fraction of component i [–], and M_i is the molar weight of component i in $[\mathrm{g\,mol^{-1}}]$.

To obtain the amount of i-th component in a given flow, the following equation can be used:

$$n_{i,x} = c_i \cdot n_x, \quad (4)$$

where c_i is the measured (molar) fraction of the i component and n_x is the total molar flow (where x can be P for permeate and R for retentate) in $[\mathrm{mol\,s^{-1}}]$.

For a better comparison with the literature, stage cut θ is defined to describe the module's properties and the process. Stage cut is defined as a ratio between molar flow in permeate and feed flows. In some papers, mass-based stage cut can also be defined, but since most scientific papers use the molar version, so does this paper. The definition of stage cut is as follows:

$$\theta = \frac{n_P}{n_F} = \frac{n_P}{n_P + n_R}, \quad (5)$$

where n_x is the molar flow in a given flow (index P for permeate, F for feed, R for retentate) in $[\mathrm{mol\,s^{-1}}]$.

To inspect the interaction between components, the ideal and actual selectivities are compared. The selectivity is expressed as:

$$\alpha_{i,j} = \frac{P_i}{P_j}, \quad (6)$$

where $\alpha_{i,j}$ is the selectivity of the component i over j (further in the text labelled $\alpha(i,j)$, to improve readability) and P_i and P_j are the permeabilities of the components i, j. The ideal selectivity is computed from pure component permeability and actual selectivity from the measurement with mixtures.

The primary quantity used in the study is component recovery R_i. Recovery was selected because it can be compared between different module types and process conditions and provides useful information for a possible implementation. Component recovery is defined as:

$$R_i = \frac{n_{i,P}}{n_{i,P} + n_{i,R}}, \quad (7)$$

where $n_{i,P}$ is the molar flow of component i in the permeate in $[\mathrm{mol\,s^{-1}}]$ and $n_{i,R}$ is the molar flow of component i in the retentate in $[\mathrm{mol\,s^{-1}}]$.

3. Results and discussion

First, the permeabilities of pure components were obtained to describe the properties of the module for the separation of H_2, CO and CO_2.

3.1. Pure component permeability

As mentioned above, the permeabilities Pi of pure components were measured. The values were averaged across all process conditions involved in the study (molar flow equal to $4.464\,\mathrm{mol\,h^{-1}}$, pressure differences ranging from 1 to 10 bar, permeate pressure from 1 to 4 bar, and temperature around 20–22 °C). Table 1 shows the measured permeability values for H_2, CO and CO_2.

Components	H_2	CO	CO_2
Permeability (Barrer)	1380 ± 62	23 ± 1	343 ± 11

Table 1. Permeabilities of pure components H_2, CO and CO_2 for given polyimide module.

To compare the values with similar modules in the literature, the permeance $(P/W)_i$ must be evaluated. Permeance is obtained by dividing the permeability by the thickness of the wall. The values of two different studies with hollow polyimide fibre modules published by Sharifian et al. [8] and Huang et al. [9], along with the permeance values of our study, are shown in Table 2.

Components	**P/W$_i$ measured**	**P/W$_i$ [4]**	**P/W$_i$ [8]**
H_2	61.40 ± 2.80	241.0	97.10
CO	1.00 ± 0.03	8.7	1.28
CO_2	15.20 ± 0.50	67.0	31.10

Table 2. Permeance values obtained in this study compared to values published in other articles by Huang et al. [4] for polyimide membrane, temperature between 25–75 °C, and Sharifian et al. [8] for similar conditions. Values in $[\mathrm{nmol\,s^{-1}\,m^{-2}\,Pa^{-1}}]$.

Two main observations can be made in the two tables above: First, Table 1 shows that polyimide

membranes can be suitable for separating H_2 from the mixture and for adjusting the ratio (increasing CO concentration in the retentate). Second, Table 2 shows that the results presented in this article are consistent with the data available in the literature. The exact composition of the membranes can cause the difference: the module used for the study contains polyetherimide in addition to pure polyimide fibres, and the structure of the polymers can also vary between modules.

3.2. Gas mixture

To demonstrate the interaction of components during the membrane separation, we compared the ideal selectivity with the measured selectivity in each case. Then, the composition of the retentate flow and the component recovery were studied.

3.2.1. Selectivity comparison

To prove the mutual interaction of components during a multicomponent membrane separation, ideal and actual selectivities were compared. Figure 2 and 3 show H_2/CO_2 and CO_2/CO selectivities. As seen in the figures below, with increasing stage cut, the measured selectivities decrease both for H_2/CO_2 and CO_2/CO.

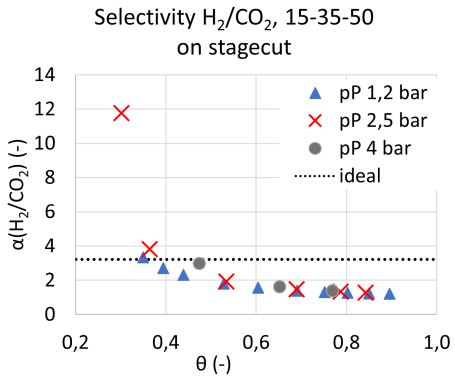

Figure 2. Ideal and measured selectivity for H_2/CO_2.

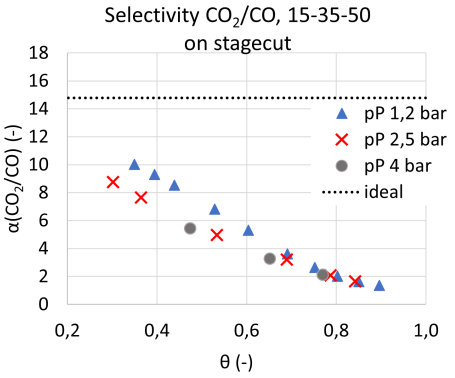

Figure 3. Ideal and measured selectivity for CO_2/CO

This phenomenon was also reported by Z. He and K. Wang [9], who tested the ideal and "true" selectivity for a mixture of He and CO_2. This case can be well compared with our case. The mentioned paper states that the true selectivity drops from 3.14 to 1.64 for the 1:1 mixture, from 3.35 to 0.94 for the 2:1 (CO_2:He) mixture and from 3.58 to 0.49 for the 3:1 (CO_2:He) mixture. This decrease is similar to the decreases observed in our study. Similarity can also be found in the size and type of the involved molecules – the ratios of ideal and measured (or "true") selectivities for H_2:CO_2 in our study (ratio 16:50 ~ 1:3) correspond very well to the data presented for He:CO_2 in a ratio of 1:3.

3.2.2. Permeate composition

As can be seen in Figure 4 and 5, with increasing stage cut, the concentrations of the high permeable components (H_2, CO_2) decrease. However, for CO_2, a slight maximum can be seen around stage cut $\theta = 0.40$ for $p_P = 1.2$ bar, of approximately 66 %mol, around stage cut $\theta = 0.45$ for $p_P = 2.5$ bar of approximately 62.5 %mol, and around stage cut $\theta = 0.5$ for $p_P = 4$ bar, of approximately 60.5 %mol. This observation implies that the CO_2 concentration in the permeate flow decreases with increasing permeate pressure.

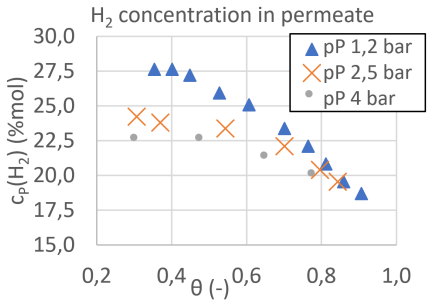

Figure 4. H_2 concentration in the permeate flow at stage cut.

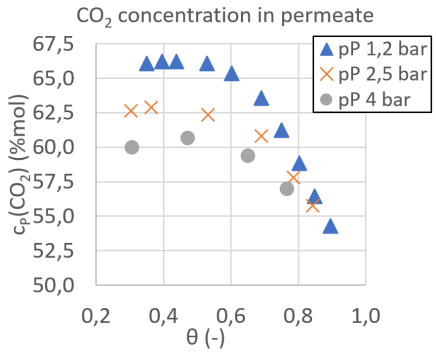

Figure 5. CO_2 concentration in the permeate flow at stage cut.

A similar trend of decreasing H_2 and CO_2 concentrations when separating a ternary gas mixture containing 45 %mol H_2, 40 %mol CO_2, 15 %mol CH_4 using two different modules (dual membrane module and polyimide module) was reported by W. Xiao et al. [9]. Their experiments were performed with

stage cut ranging from 0.1 to over 0.4, and the concentration (mole fraction in the original paper) decreased from 68 %mol to 60 %mol for CO_2 and from 41 %mol to 32 %mol for H_2 when using the polyimide hollow-fibre module.

3.2.3. Components recovery

One of the dependencies that appear when inspecting multicomponent gas membrane separation is that the recovery of the component achieved at a certain pressure is dependent on the permeability of the component. The component with the highest permeability (H_2) reaches the highest recovery among the components at any pressure difference. However, the recovery does not increase proportionally with the permeability of the pure component – the permeability of H_2 is four times higher than the permeability of CO_2. Figure 6 shows data for all three components (H_2, CO, and CO_2) for permeate pressure $p_P = 2.5$ bar. The described dependencies can be observed.

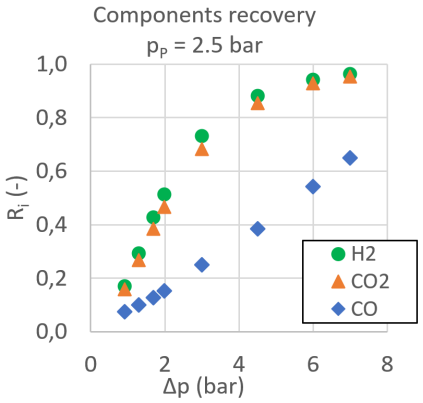

Figure 6. Component recovery for H_2, CO and CO_2 for permeate pressure $p_P = 2.5$ bar.

Another observed effect is the effect of the permeate pressure. The two more permeable components, H_2 and CO_2, reach lower values of component recovery with an increasing permeate pressure. The recovery for CO increases with pressure difference; however, it does not depend on the permeate pressure within the range of the statistical uncertainty. This implies that the differences between recoveries for different permeate pressures increase with increasing permeability of the pure component. Figure 7–9 show the recoveries for the three components.

W. Xiao et al. [9] have reported similar trends for component recovery concerning the CO_2 in the ternary mixture of H_2:CO_2:CO (in ratio 45:40:15, respectively) as the published data follow the trend. However, the data for H_2 seem to differ as the recovery seems to reach its limit below 0.4. This difference can be caused by the nature of the module. To describe the dependency of recovery on the total pressure drop and other process parameters, it is necessary to test model mixtures of different compositions (same components, different concentrations).

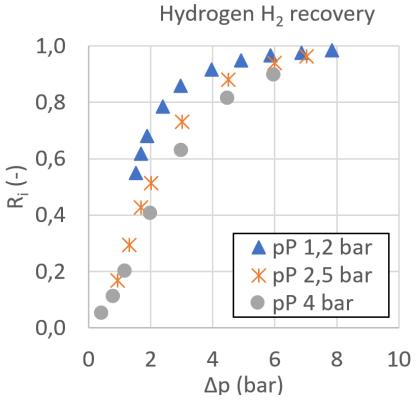

Figure 7. Hydrogen recovery on total pressure drop.

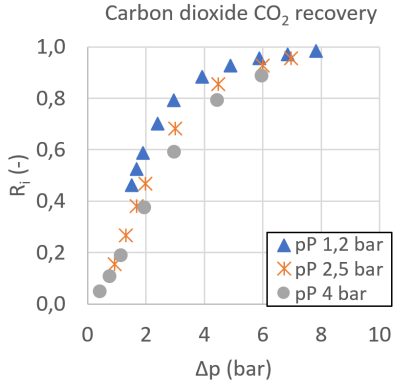

Figure 8. Carbon dioxide CO_2 recovery on total pressure drop.

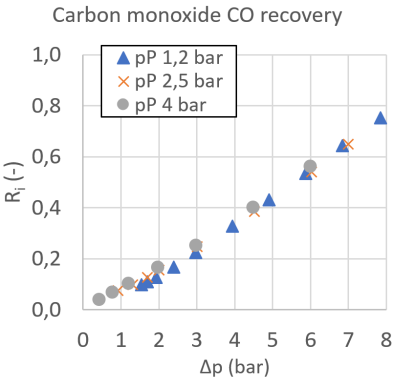

Figure 9. Carbon monoxide CO recovery on total pressure drop.

4. Conclusions

Several conclusions can be made based on the presented data. First, the tested hollow fibre module (polyetherimide-polyimide fibres manufactured by MemBrain) is suitable for H_2 and CO_2 separation, as the permeabilities of the pure components reach 1380 ± 62 Barrer for H_2 and 343 ± 11 Barrer for CO_2. The permeability of CO reached 23 ± 1 Barrer. The ideal selectivity (computed as the ratio of pure component permeabilities) for H_2/CO_2 and for CO_2/CO differ from the measured selectivities – the measured selectivities α_{H_2/CO_2} and $\alpha_{CO_2/CO}$ decrease with increasing stage cut and drop to 1/3 of the ideal selec-

tivity for α_{H_2/CO_2} and 1/10 of the ideal selectivity for $\alpha_{CO_2/CO}$ (both at stage cut $\theta \approx 0.9$).

Regarding the concentration of H_2 and CO_2 in the permeate flow, both values decrease with increasing stage cut θ approaching 1. For the concentration of CO_2, maximum values of the concentration of $c_P(CO_2)$ can be observed at a value of 66 %mol for stage cut $\theta = 0.40$ ($p_P = 1.2$ bar), 62.5 %mol for stage cut $\theta = 0.45$ ($p_P = 2.5$ bar) and 60.5 %mol for stage cut $\theta = 0.5$ ($p_P = 4$ bar).

The component recovery dependency on the permeate pressure drop has been studied. An observed trend is that the permeability of the component affects the recovery of the component so that the components with a higher permeability (when processed in pure form) reach higher recoveries at a given pressure difference. However, the increase in recovery is not directly proportional to permeability. Also, a dependency between the component recovery and the permeate pressure has been revealed, showing that increasing the permeate pressure results in lower recoveries of the components at a given pressure drop. This can be caused by multiple reasons that have not been specified; however, the potential causes are a decrease in sorption and diffusion coefficients with increasing pressure and/or by fibre compression resulting in a decrease in its permeability.

This study shows that component recovery of H_2, CO_2, and CO can be affected by process conditions. Therefore, for a successful industrial application of the membrane separation within the field of biomass gasification, a wider sample of process conditions must be studied to develop a reliable model for describing the process. After that, membrane operations could be used for adjusting the ratio of the components by changing the pressure conditions, which would compensate for the variance in the biomass gasification product composition (caused by unstable feed composition due to biomass nature) and allow a better optimization of the technology.

List of symbols

c_i concentration in component i [%mol]

L length of the module [m]

m_F, m_P, m_R mass flow of gas in feed, permeate, and retentate, respectively [$g\,s^{-1}$]

M_i molar weight of component i [$g\,mol^{-1}$]

n_i molar flow of component i [$mol\,s^{-1}$]

p_F, p_P, p_R pressure in the feed, permeate, and retentate branch, respectively [bar]

P_i permeability of component i [Barrer]

R_i i-component recovery

S total area of the module [m2]

T_F, T_P, T_R temperature in feed, permeate, and retentate, respectively [°C]

T_M mean measurement temperature [°C]

W thickness of wall of the fibres [μm]

Δp pressure difference [bar]

θ stage cut [–]

Acknowledgements

This work was supported by the Ministry of Education, Youth and Sports of the Czech Republic under OP RDE grant number CZ.02.1.01/0.0/0.0/16_019/0000753 "Research centre for low-carbon energy technologies" and by Student Grant Competition of CTU as part of grant no. SGS20/118/OHK2/2T/12.

References

[1] A. Y. Krylova. Products of the fischer-tropsch synthesis (A review). *Solid Fuel Chemistry* **48**(22-35), 2014. https://doi.org/10.3103/S0361521914010030.

[2] S. De Tissera, M. Köpke, S. D. Simpson, et al. Syngas biorefinery and syngas utilization. In K. Wagemann, N. Tippkötter (eds.), *Biorefineries. Advances in Biochemical Engineering/Biotechnology*, vol. 166. Springer, Cham, 2017. https://doi.org/10.1007/10_2017_5.

[3] W. Choi, P. G. Ingole, J.-S. Park, et al. H_2/CO mixture gas separation using composite hollow fiber membranes prepared by interfacial polymerization method. *Chemical Engineering Research and Design* **102**:297–306, 2015. https://doi.org/10.1016/j.cherd.2015.06.037.

[4] W. Huang, X. Jiang, G. He, et al. A novel process of H_2/CO_2 membrane separation of shifted syngas coupled with gasoil hydrogenation. *Processes* **8**(5):590, 2020. https://doi.org/10.3390/pr8050590.

[5] S. Lee, M. Binns, J. H. Lee, et al. Membrane separation process for CO_2 capture from mixed gases using TR and XTR hollow fiber membranes: Process modeling and experiments. *Journal of Membrane Science* **541**:224–234, 2017. https://doi.org/10.1016/j.memsci.2017.07.003.

[6] S. Qadir, A. Hussain, M. Ahsan. A computational fluid dynamics approach for the modeling of gas separation in membrane modules. *Processes* **7**(7):420, 2019. https://doi.org/10.3390/pr7070420.

[7] N. Alkhamis, D. E. Oztekin, A. E. Anqi, et al. Numerical study of gas separation using a membrane. *International Journal of Heat and Mass Transfer* **80**:835–843, 2015. https://doi.org/10.1016/j.ijheatmasstransfer.2014.09.072.

[8] S. Sharifian, N. Asasian-Kolur, M. Harasek. Process simulation of syngas purification by gas permeation application. *Chemical Engineering Transactions* **76**:829–834, 2019. https://doi.org/10.3303/CET1976139.

[9] W. Xiao, P. Gao, Y. Dai, et al. Efficiency separation process of $H_2/CO_2/CH_4$ mixtures by a hollow fiber dual membrane separator. *Processes* **8**(5):560, 2020. https://doi.org/10.3390/pr8050560.

EXPERIMENTAL VERIFICATION OF THE IMPACT OF THE AIR STAGING ON THE NO_X PRODUCTION AND ON THE TEMPERATURE PROFILE IN A BFB

Matěj Vodička*, Kristýna Michaliková, Jan Hrdlička, Pavel Skopec, Jitka Jeníková

Czech Technical University in Prague, Faculty of Mechanical Engineering, Department of Energy Engineering, Technická 4, 166 07 Prague, Czech Republic

* corresponding author: matej.vodicka@fs.cvut.cz

Abstract.

The results of an experimental research on air staging in a bubbling fluidized bed (BFB) combustor are presented within this paper. Air staging is known as an effective primary measure to reduce NO_X formation. However, in the case of a number of industrial BFB units, it does not have to be sufficient to meet the emission standards. Then selective non-catalytic reduction (SNCR) can be a cost-effective option for further reduction of the already formed NO_X. The required temperature range at the place of the reducing agent injection for an effective application of the SNCR without excessive ammonia slip is above the temperatures normally attained in BFBs. The aim of this paper is to evaluate the impact of staged air injection on the formation of NO_X in BFB combustors and to examine the possibility of increasing the freeboard temperature. Several experiments with various secondary/primary air ratios were performed with a constant oxygen concentration in the flue gas. The experiments were carried out using wooden biomass and lignite as fuel in a 30 kW_{th} laboratory scale BFB combustor. Furthermore, the results were verified using a 500 kW_{th} pilot scale BFB unit. The results confirmed that the air staging can effectively move the dominant combustion zone from the dense bed to the freeboard section, and thus the temperatures for an effective application of the SNCR can be obtained.

Keywords: Air staging, bubbling fluidized bed, NO_X, SNCR.

1. Introduction

Nitrogen oxides (NO_X), particularly NO and NO_2, are gaseous pollutants that can cause significant environmental issues. One of the main contributors to overall NO_X emissions is the combustion of solid fuels.

There are three mechanisms of NO_X formation in the combustion process: the thermal and prompt NO_X formation mechanism, where the source of NO_X is atmospheric nitrogen, and the oxidation of fuel-bound nitrogen. Since the breaking of tight N_2-bond is strongly temperature dependent, the thermal NO_X formation mechanism (described by Zeldovich et al. [1]) is usually considered important at temperatures higher than 1500 °C [2]. Then, the prompt formation of NO_X (described by Fenimore [3]) can be observed in fuel-rich zones in pre-mixed hydrocarbon flames. The prompt NO_X formation is also strongly temperature dependent and is relevant from above 1400 °C. These conditions are not typical for combustion in bubbling fluidized beds (BFBs) and therefore prompt and thermal NO_X are of minor importance, and fuel-bound nitrogen is considered to be the main contributor to NO_X formation there [4–6]. Fuel-bound nitrogen is an important source of NO_X in the combustion of fossil fuels and biomass. It is particularly important for coal combustion, which typically contains $0.5 - 2.0$ % wt. of nitrogen, and for the combustion of non-wooden biomass, where its content can reach up to 5 % wt. The degree of conversion of fuel-N to NO_X is almost independent of the type of nitrogen compound, but is significantly dependent on the local combustion environment [7]. In the furnace, fuel is thermally decomposed and volatile and char compounds are produced. Fuel-bound nitrogen is distributed between char and volatiles, depending on the fuel structure and devolatilisation conditions, such as temperature, heating rate, oxygen concentration, or residence time. In case of lower temperatures or shorter residence times, nitrogen preferably remains in the char, while at higher temperatures, it is part of the volatiles [8]. The mechanisms of volatile-N and char-N conversion were described by Winter et al. [9], who studied the combustion of a single particle of bituminous coal, subbituminous coal and beech wood in an electrically heated, laboratory-scale, fluidized bed combustor.

The NO_X reduction can be generally realized using different methods; either by modifying the combustion process itself to supress the NO_X formation (so-called primary measures) or applied after the combustion process to decrease the already formed NO_X (so-called secondary measures). Skopec et al. [6] observed using a 500 kW_{th} BFB combustor that the NO_X formation depends mainly on the excess of oxygen in the combustion zone and slightly also on the fluidized bed temperature. This was also confirmed by Svoboda

and Pohořelý [10], who studied the formation of NO_X and N_2O in a laboratory scale pressurized BFB. They observed that NO_X formation was strongly promoted by an increase in air stoichiometry (while N_2O formation was depressed) at atmopheric pressure. They also observed that an increase in the temperature of the fludized bed slightly promotes the formation of NO_X and decreases the formation of N_2O under slightly elevated pressure (0.25 MPa). Therefore, the primary measures reduce the temperature and oxygen concentration in the furnace and subsequently allow the oxidation of the remaining combustibles above the furnace. As primary measures, staged injection of air or fuel and flue gas recirculation could be used. Fuel staging requires secondary gas phase fuel and it is not a practically applied method for BFBs.

In the case of staged air injection, the oxidizer is separated into two or even more streams. The first stream is introduced into the BFB as the primary air (possibly mixed with the FGR). The second stream (and possibly the consequent streams) is introduced into the freeboard section above the fluidized bed. In the primary combustion zone, there are fuel-rich conditions (stoichiometric or even sub-stoichiometric oxygen/fuel ratio) that cause a smaller conversion of the NO_X precursor to NO_X and favor the formation of N_2. Furthermore, the already formed NO can be further reduced through a) reburning reactions with the released fuel N (mainly HCN and NH_3), or b) through reactions with carbon compounds that were not yet completely oxidized, or c) on the char surface through catalytic reactions [11, 12]. Gaseous products of incomplete combustion (CO and TOC), which are inevitably formed under such conditions, are subsequently oxidized in the freeboard section, where the secondary oxidizer is introduced. The efficiency of NO_X reduction through staged injection of air is significantly dependent on the residence time in the primary zone with sub-stoichiometric (reduction) conditions [12, 13]. The optimum residence time in the sub-stoichiometric zone may vary according to the fuel structure. For a lignite coal, it is about 1.5 s [13]. If the residence time in the this zone is too short, NO can further form in a significant amount in the secondary oxidation zone [12]. Sirisomboon and Charernporn [14] also observed that the relative reduction efficiency of the staged air injection depends on the overall stoichiometry of the combustion air. With the most extensive air staging, they observed a similar reduction of about 70 ppmv of NO at all air excess ratios (in the range from 20 to 80 %). Since the formation of NO_X is strongly affected by overall air stoichiometry, the reduction efficiency was higher for lower excess of air and lower for higher excess of air.

Secondary measures are mainly selective non-catalytic (SNCR) and selective catalytic reduction (SCR). These flue gas treatments use reducing agents containing NH_2 (ammonia, urea, ammonia water, etc.), which can reduce NO. The reduction follows

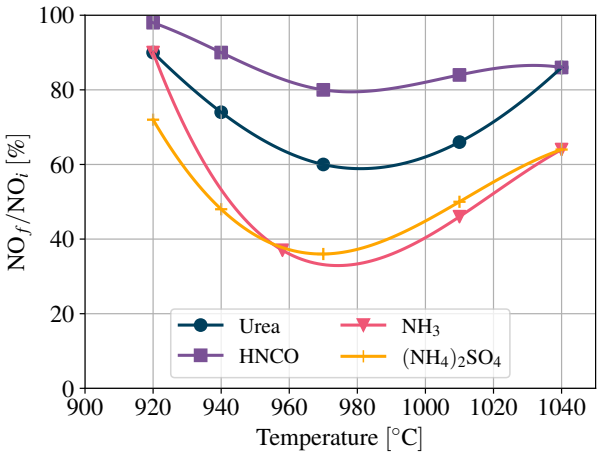

FIGURE 1. Comparison of the dependence of the NO_X reduction efficiency (expressed as a ratio of the final NO_X concentration with SNCR to the initial NO_X concentration without SNCR) using urea, cyanuric acid, ammonia and ammonium sulfate on the flue gas temperature [15].

Equation 1 in the case of using ammonia as a reducing agent

$$2\,NO + 2\,NH_3 + \frac{1}{2}\,O_2 \longrightarrow 2\,N_2 + 3\,H_2O \quad (1)$$

and Equation 2 in the case of using urea.

$$2\,NO + CO(NH_2)_2 + \tfrac{1}{2}\,O_2 \longrightarrow 2\,N_2 + CO_2 + 3\,H_2O \quad (2)$$

The effective operation of SNCR without excessive ammonia slip is determined by an optimal temperature range for the injection of the reducing agent into the combustor. The ideal temperature range depends on the reducing agent used, which can be seen in Figure 1. However, the required temperature range 900 – 1000 °C is normally achieved neither in the bed nor in the freeboard in BFBs.

The catalyst present in the SCR systems usually allows achieving higher reduction efficiency at significantly lower temperatures compared to SNCR technology, but at a high investment cost.

Air staging, which partly moves the combustion zone from the dense bed zone to the freeboard of the BFB, appears to be a suitable measure for increasing the freeboard temperature to the required temperature range. Sirisomboon and Charernporn [14] increased the temperature in the freeboard section of a pilot scale BFB of about 100 °C through air staging and reached up to 1 100 °C using high volatile sunflower shells as fuel.

Although NO_X formation and possible reduction paths in BFBs have been studied by a number of authors using multiple fuels and various scales of devices, the possible application of SNCR in BFBs has not been of significant interest yet.

This paper presents a comprehensive experimental study of the impact of staged air supply on NO_X formation in a BFB and on the temperature profile within

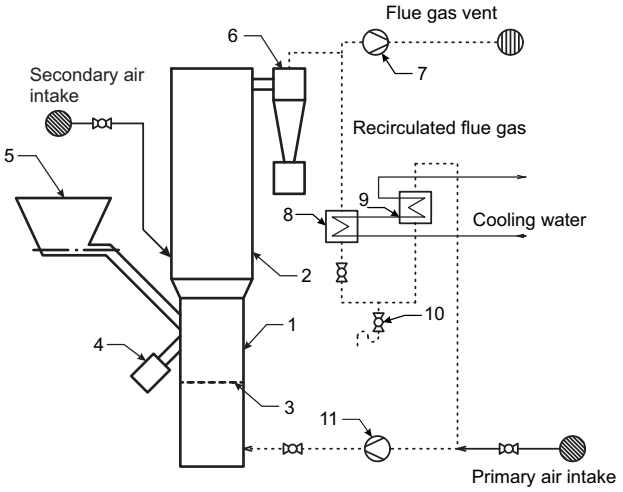

(a) . 30 kW_{th} experimental BFB facility and its equipment.

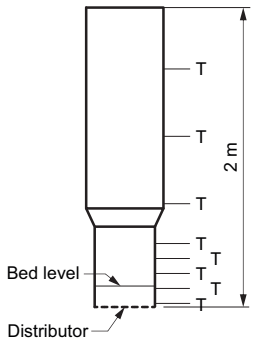

(b) . Indication of temperature measuring points.

Figure 2. Scheme of the 30 kW_{th} experimental BFB facility. 1) fluidized bed region, 2) freeboard section, 3) fluidizing gas distributor, 4) fluidized bed spillway, 5) fuel feeder, 6) cyclone particle separator, 7) flue gas fan, 8) and 9) FGR water coolers, 10) condensate drain, and 11) primary gas fan.

the combustor as a consequence of sub-stoichiometric combustion in the dense bed and subsequent oxidation of the remaining combustibles in the freeboard section in order to be able to define the process conditions for reaching the SNCR optimal temperature range. A number of experiments were performed combusting lignite and wooden pellets in various operating regimes of a 30 kW_{th} BFB experimental facility. Furthermore, to validate the results and their applicability to the industrial scale, the same experiments were performed in a 500 kW_{th} pilot-scale BFB combustor.

2. Experiments

2.1. Experimental setup

The 30 kW_{th} experimental facility has been comprehensively described elsewhere [16] and so it will be described only briefly here. Its scheme is given in Figure 2. The facility is 2 m high, has a rectangular cross-section, and is made of stainless steel insulated from the outside using the 50 mm thick Insulfrax board in the fluidized bed section and using mineral wool

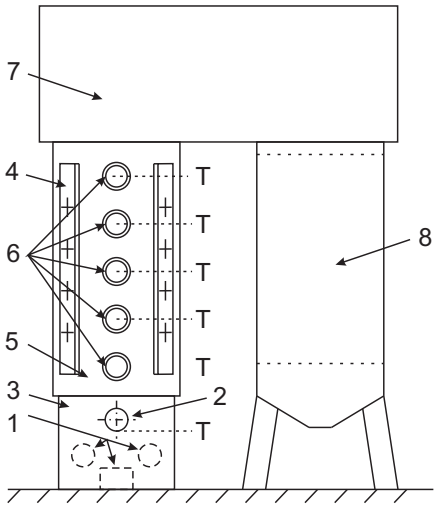

Figure 3. Scheme of the 500 kW_{th} pilot-scale BFB facility. 1) primary gas inlets, 2) fuel feeder, 3) fluidized bed region, 4) secondary air distributors, 5) freeboard section, 6) inspection windows, 7) crossover pass, and 8) heat exchanger. The 'T' signs indicates the temperature measurement points.

in the freeboard section. There are no internal heat exchangers in the facility.

Volumetric flows of primary and secondary air were measured using two rotameters. The temperature profile along the height of the facility was measured using five thermocouples in the dense bed region and three thermocouples in the freeboard region. Directly in the fluidized bed, the temperature was measured with two thermocouples. However, the value of only one placed 166 mm above the fluidizing gas distributor was taken as representative. Primary air with real flue gas recirculation were used to provide sufficient fluidization, and secondary air was introduced at the beginning of the freeboard section. The flue gas was continuously sampled and the volumetric fractions of CO_2, CO, SO_2 and NO_X were measured using a NDIR sensors, while the volumetric fraction of O_2 was measured using a paramagnetic sensor.

The scheme of the 500 kW_{th} pilot scale BFB boiler is given in Figure 3. This boiler consists of three main sections: the combustion chamber with freeboard, the crossover pass, and the heat exchanger. The fluidization gas, formed by primary air and recirculated flue gas, enters the bed trough distributor consisting of 36 nozzles placed in 6 rows. The combustion chamber and the freeboard section have a cylindrical cross section and are insulated with a fireclay lining with a water-cooled surface. In the freeboard area, the facility is equipped with 6 thermocouples along the height. Secondary air is supplied to the freeboard section by 4 distributors placed evenly on a perimeter, and each distributor can provide the secondary air inlet at 4 different heights. For the experiments, secondary air inlets at a height of 550 mm above the fluidized bed were used. From the freeboard section, the flue gas continues to the empty crossover pass

	as received				dry ash free					
	LHV [MJ · kg^{-1}]	water [wt. %]	ash [wt. %]	comb.* [wt. %]	C [wt. %]	H [wt. %]	N [wt. %]	S [wt. %]	O* [wt. %]	volatiles [wt. %]
lignite	17.6	21.1	9.9	69.0	72.3	6.3	1.1	1.3	19.0	47.0
wood	16.4	7.8	1.5	90.7	51.0	6.9	0.3	0.003	41.797	84.6

* Calculated as balance to 100 %.

TABLE 1. Proximate and ultimate analysis of the fuels used within the experiments.

		Liginite ash	LWA 0−2
ρ_s	kg · m^{-3}	2 195	1088
ρ_b	kg · m^{-3}	795	570
d_{mean}	mm	0.37	1.07
d_{mode}	mm	0.23	1.02
d_{10}	mm	0.15	0.54
d_{50}	mm	0.74	1.05
d_{90}	mm	1.77	1.59

TABLE 2. Results of the particle size distribution analysis of the fluidized bed materials.

with water-cooled surface and then enters the heat exchanger. The flue gas was continuously sampled and the volumetric fractions of CO_2, CO, SO_2 and NO_X were measured using NDIR sensors, while the volumetric fraction of O_2 was measured using a paramagnetic sensor.

2.2. MATERIALS

The experiments were carried out using Czech lignite Bílina HP1 135 and pellets from spruce wood as fuel. The proximate and ultimate analyses of lignite and wooden pellets are given in Table 1. Lignite has a significantly higher nitrogen content compared to spruce wood, so the NO_X yields should also be higher in case of combustion of lignite. Spruce wood combustibles contain about 100 % more volatiles compared to lignite, which should move the dominant combustion zone slightly higher in the facility in case of wood combustion. For experiments carried out using the 30 kW_{th} facility, the lignite was sieved to a particle size of up to 7 mm. The lignite ash was used as a bed material in the case of lignite combustion. Biomass combustion experiments were carried out using spruce wood pellets (according to the ENplus A1 standard) and using a lightweight ceramic aggregate (LWA) as an external bed material. The physical properties of the bed materials are given in Table 2. The arithmetic mean, mode, median, 1st decile (d_{10}), and 9th decile (d_{90}) particle size were evaluated. The density and bulk density were analyzed along with the particle size. The lignite ash can be classified as Geldart B particles which are well fluidizable and form vigorous bubbles. The used LWA population referred as '0−2' is on the boundary between B and D particle types in the Geldart classification, where the class D particles are difficult to fluidize in deep beds, they spout, form exploding bubbles or channels [17].

From the analysis of the particle size distribution (PSD), the minimum fluidization velocity, the minimum complete fluidization velocity (defined as u_{mf} calculated for the particle size d_{90}, and the terminal particle velocity were evaluated for two different conditions of the fluidization gas. The numerical approach was taken from [18]. First, the gas properties corresponded to air at 20 °C ($\rho_g = 1.20\,kg \cdot m^{-3}$, $\eta = 1.8 \cdot 10^{-5}$ Pa·s) and secondly to air at 850 °C ($\rho_g = 0.29\,kg \cdot m^{-3}$, $\eta = 3.8 \cdot 10^{-5}$ Pa·s). The fluidizing gas temperature of 850 °C was chosen, because when the fluidizing gas passes through the bed of hot material, it is heated to the bed temperature within a few millimeters above the fluidizing gas distributor [19]. The minimum fluidization velocities of both bed materials were also experimentally verified by measuring the correlation of bed pressure drop and superficial fluidizing gas velocity u_0. This method can be found in [18]. This test was carried out using air at 20 °C as fluidization gas. The calculated minimum fluidization velocities, the complete fluidization velocities, and the terminal velocities, as well as the experimentally determined minimum fluidization velocities, are given in Table 3.

2.3. METHODS

To evaluate the impact of staged air supply on NO_X emissions and on the temperature profile within the BFB combustor in consequence of the substoichiometric combustion in the dense bed and subsequent oxidation of the remaining combustibles in the freeboard, two series of experiments were performed using the 30 kW_{th} BFB experimental facility and using lignite and biomass as fuels. Furthermore, a series of experiments was done using the 500 kW_{th} pilot scale facility and only using lignite as fuel. To highlight this impact and reduce the side effects of fluidized bed temperature, the experiments were carried out with a constant bed temperature of 880 °C and the oxygen level in the dry flue gas maintained at 8 % for wooden pellets and at 6 % for lignite for both facilities. The bed temperature was controlled through the change of volumetric flow or of the composition of the fluidizing gas, which consisted of primary air and recirculated flue gas.

Conditions			Lignite ash	LWA 0−2
calculation (experimental) results				
air at 20 °C	u_{mf}	$\mathrm{m \cdot s^{-1}}$	0.37 (0.42)	0.40 (0.38)
	u_{mf-90}	$\mathrm{m \cdot s^{-1}}$	1.72	0.65
	u_t	$\mathrm{m \cdot s^{-1}}$	2.02	3.09
	u_{t-90}	$\mathrm{m \cdot s^{-1}}$	5.47	4.06
air at 850 °C	u_{mf}	$\mathrm{m \cdot s^{-1}}$	0.21	0.27
	u_{mf-90}	$\mathrm{m \cdot s^{-1}}$	2.59	0.62
	u_t	$\mathrm{m \cdot s^{-1}}$	2.36	4.95
	u_{t-90}	$\mathrm{m \cdot s^{-1}}$	10.23	7.24

Table 3. Minimum fluidization velocities u_{mf}, terminal velocities u_t (calculated for d_{mean}), minimum velocities of complete fluidization u_{mf-90}, and complete terminal velocities u_{t-90} (calculated for d_{90}) of the selected fluidized bed materials. The experimental values are in brackets.

The degree of the combustion air staging can be described using Equation 3.

$$\psi = \frac{V_{air,\,sec}}{V_{air,\,prim}}, \tag{3}$$

where $V_{air,\,sec}$ is the volumetric flow of secondary air and $V_{air,\,prim}$ is the volumetric flow of primary air.

In the experiments performed using 30 $\mathrm{kW_{th}}$ BFB facility, one case without air staging was measured as a reference for both fuels and then the following four cases with an increasing secondary/primary air ratio ψ to 2.75 were measured. The minimum amounts of primary and secondary air were limited by the flowmeters used for the volumetric flows measurement and were set to 10 $\mathrm{m^3_N/h}$. The step for increment of the secondary air flow was 6 $\mathrm{m^3_N/h}$. However, to keep the overall oxygen level constant and maintain the bed temperature and sufficient fluidization, it was not possible to exactly keep the required secondary/primary air ratio constant throughout. A reference case without air staging and three cases with an increasing secondary/primary air ratio ψ up to 1.6 were performed using the 500 $\mathrm{kW_{th}}$ pilot-scale facility.

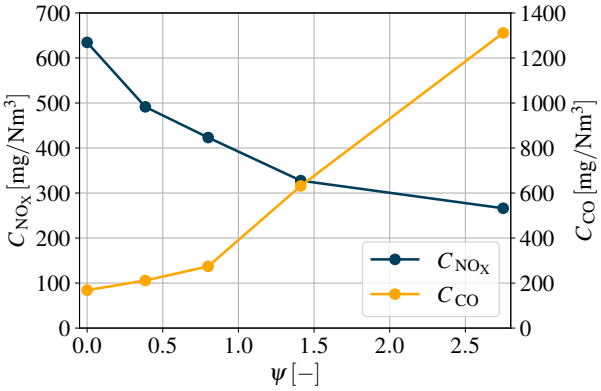

Figure 4. The dependence of the NO_X and CO volumetric concentration in dry flue gas on the ratio of the secondary to primary air volumetric flows ψ in the case of a lignite combustion in the 30 $\mathrm{kW_{th}}$ BFB facility. The gaseous pollutants concentrations related to 6 % vol. of O_2 in dry flue gas.

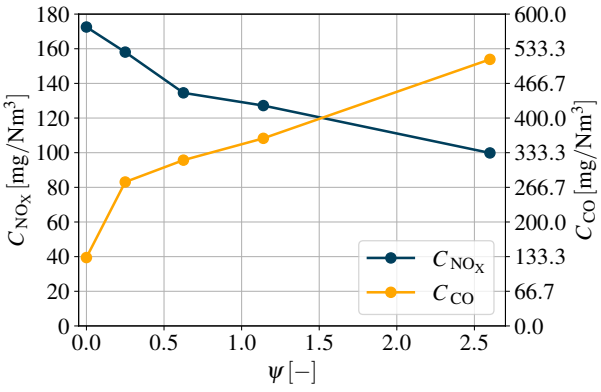

Figure 5. The dependence of the NO_X and CO volumetric concentration in dry flue gas on the ratio of the secondary to primary air volumetric flows ψ in the case of a biomass combustion in the 30 $\mathrm{kW_{th}}$ BFB facility. The gaseous pollutants concentrations related to 6 % vol. of O_2 in dry flue gas.

3. Results and Discussion

The results of biomass and coal combustion in the 30 $\mathrm{kW_{th}}$ facility (given in Figures 4 and 5 and Tables 4 and 5) show that the air staging positively affected NO_X concentration in the flue gas and the NO_X formation was suppressed with a higher secondary/primary air ratio. On the other hand, the CO level increased significantly, as can be seen in Figures 4 and 5. This could be caused by the decrease in excess oxygen to a sub-stoichiometric atmosphere in the fluidized bed region ($\lambda_{prim} < 1$) connected with incomplete combustion and increased CO production, which is then not oxidized effectively in the freeboard region, possibly due to lower temperatures there. Therefore, the application of air staging from this point of view is limited by acceptable CO emissions. Unfortunately, the flue gas temperature significantly decreased as

Parameter	Unit	'Case 1'	'Case 2'	'Case 3'	'Case 4'	'Case 5'
ψ	[–]	0.0	0.35	0.62	1.23	2.45
λ_{prim}	[–]	1.4	1.04	0.8	0.68	0.48
ϕ_{O_2}	[% vol.]	5.9 ± 0.03	5.93 ± 0.03	5.96 ± 0.03	6.09 ± 0.03	6.13 ± 0.01
t_{BFB}	[°C]	881 ± 0.6	889 ± 0.3	886 ± 0.3	890 ± 0.4	887 ± 0.3
C_{NO_X}	$[mg \cdot m_N^3]$	635 ± 1	491 ± 2	423 ± 1	328 ± 1	266 ± 0
C_{CO}	$[mg \cdot m_N^3]$	277 ± 7	347 ± 4	451 ± 1	1038 ± 5	2155 ± 8
u_0	$[m \cdot s^{-1}]$	1.73	1.73	1.86	1.71	1.71
N – NO	[% mole]	21.61	16.73	14.41	11.16	9.06
m_{fuel}	$[kg \cdot h^{-1}]$	5.8	5.8	5.8	5.8	5.8

TABLE 4. Experimental results of the staged supply of air on the NO_X formation in the case of lignite combustion in the 30 kW_{th} BFB facility. Gaseous pollutant concentrations are related to 6,% vol. of O_2 in dry flue gas.

Parameter	Unit	'Case 1'	'Case 2'	'Case 3'	'Case 4'	'Case 5'
ψ	[–]	0.0	0.25	0.6	1.09	2.29
λ_{prim}	[–]	1.64	1.29	1.03	0.81	0.48
ϕ_{O_2}	[% vol.]	8.21 ± 0.05	8.24 ± 0.04	7.91 ± 0.03	7.93 ± 0.04	7.44 ± 0.03
t_{BFB}	[°C]	888 ± 0.7	894 ± 0.5	888 ± 0.3	890 ± 0.7	897 ± 0.9
C_{NO_X}	$[mg \cdot m_N^3]$	173 ± 0	158 ± 0	135 ± 0	127 ± 0	100 ± 0
C_{CO}	$[mg \cdot m_N^3]$	217 ± 3	455 ± 5	524 ± 5	593 ± 6	843 ± 6
u_0	$[m \cdot s^{-1}]$	2.46	2.35	2.41	2.31	2.31
N – NO	[% mole]	12.01	11.0	9.36	8.85	6.95
m_{fuel}	$[kg \cdot h^{-1}]$	6.9	6.9	6.9	6.9	6.9

TABLE 5. Experimental results of the staged supply of air on the NO_X formation in the case of wood combustion in the 30 kW_{th} BFB facility. Gaseous pollutant concentrations are related to 6 % vol. of O_2 in dry flue gas.

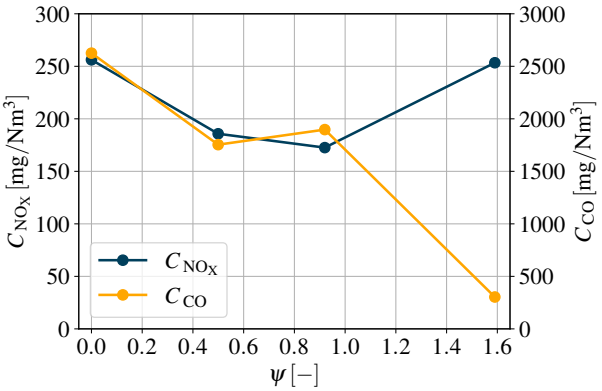

FIGURE 6. The dependence of the NO_X and CO volumetric concentration in dry flue gas on the ratio of the secondary to primary air volumetric flows ψ in the case of a lignite combustion in the 500 kW_{th} BFB facility. The gaseous pollutants concentrations related to 6 % vol. of O_2 in dry flue gas.

the gas passed through the facility due to poor insulation of the freeboard section of the 30 kW_{th} BFB facility. If the temperature is too low at the point of secondary air injection, the oxidation of the unburned combustibles is very slow, which reduces the desired effect of air staging.

Since both the fluidized bed and the freeboard section are well insulated by the fireclay lining in the 500 kW_{th} facility, the freeboard temperatures are significantly higher compared to the 30 kW_{th} facility. Therefore, secondary air properly oxidizes CO and other incomplete combustion products and the concentration of CO does not increase (moreover, it decreases) with an increasing secondary/primary air ratio ψ, as can be seen in Figure 6 and Table 6, where the results of lignite combustion in the 500 kW_{th} BFB facility are given. Based on the rise in the NO_X concentration in flue gas related to the increase in the secondary/primary air ratio ψ from 0.92 to 1.59 in Figure 6, it can be estimated that the NO_X reduction through the air staging has an optimum at the value of the secondary/primary air ratio ψ about 1. The further NO_X reduction observed in the results obtained using the 30 kW_{th} facility can then be explained by the increased CO concentration.

The impact of air staging on the temperature profile in the 30 kW_{th} combustor can be seen in Figures 7 and 8 and on the temperature profile in the 500 kW_{th} combustor in Figure 9.

In the case of the 30 kW_{th} combustor, it was not possible to achieve the temperatures required for SNCR while keeping the bed temperature constant for coal combustion. In the best scenario (for the secondary/primary air ratio ψ 1.4), the temperature rose by 10 °C in a small area directly above the fluidized bed, but this could also be caused by not exactly the same fluidized bed temperature. In general, no significant positive impact was observed from the increase in secondary air supply. In the case of biomass

Parameter	Unit	'Case 1'	'Case 2'	'Case 3'	'Case 4'
ψ	[−]	0.0	0.48	0.91	1.6
λ_{prim}	[−]	1.19	0.7	0.66	0.57
ϕ_{O_2}	[% vol.]	6.06 ± 0.06	5.27 ± 0.04	4.75 ± 0.04	5.73 ± 0.07
t_{BFB}	[°C]	887 ± 0.7	885 ± 0.5	878 ± 0.6	879 ± 0.4
C_{NO_X}	$[mg \cdot m_N^3]$	256 ± 2	186 ± 1	173 ± 1	253 ± 1
C_{CO}	$[mg \cdot m_N^3]$	4314 ± 209	2882 ± 206	3118 ± 236	499 ± 81
u_0	$[m \cdot s^{-1}]$	1.71	1.29	1.02	1.26
N − NO	[% mole]	8.72	6.32	5.87	8.63
m_{fuel}	$[kg \cdot h^{-1}]$	50.0	55.0	46.0	62.0

Table 6. Experimental results of the staged supply of air on the NO_X formation in the case of lignite combustion in the 500 kW_{th} BFB facility. Gaseous pollutants concentrations are related to 6 % vol. of O_2 in dry flue gas.

combustion, enhanced combustion of volatiles above the fluidized bed was observed with an increase in the secondary/primary air ratio, causing a considerable increase in temperature. There, a temperature greater than 900 °C was reached, thus conducive conditions could be provided for the application of SNCR, although the secondary/primary air ratio must be high. However, a significant decrease in freeboard temperatures can be observed for both biomass and coal combustion in Figures 7 and 8, possibly due to insufficient insulation of the freeboard section. The negative impact of staged air supply can be caused by increased volumetric flow, as the higher flow rate is then associated with heat loss. It can be expected that with insulation improvement, air staging would also increase the freeboard temperature for coal combustion, because it did so in the 500 kW_{th} facility, where both the fluidized bed and the freeboard section are insulated using an inner fireclay lining. As can be seen in Figure 9, where the dependence of the temperature height profile on the secondary/primary air ratio ψ is given, staged air injection can move the dominant combustion zone from the furnace to the freeboard section and therefore could increase the freeboard temperature sufficiently for efficient application of SNCR in the BFB boilers even in the case of a lignite combustion. The most significant increase in freeboard temperature was achieved for the secondary/primary air ratio 0.92, where the freeboard temperature was 953 °C for the fluidized bed temperature 880 °C. The further increase in the secondary/primary air ratio did not improve the freeboard temperature but rather cooled it. It can also be seen that the higher volumetric flow of the secondary air and so the higher flue gas velocity in the freeboard section moved the highest temperature measured in the height profile further in the flue gas stream. The increased temperature in the freeboard section invoked by the staged injection of air is also in agreement with the findings of Sirisomboon and Charenporn [14], who carried out the experiments in a well insulated pilot scale BFB.

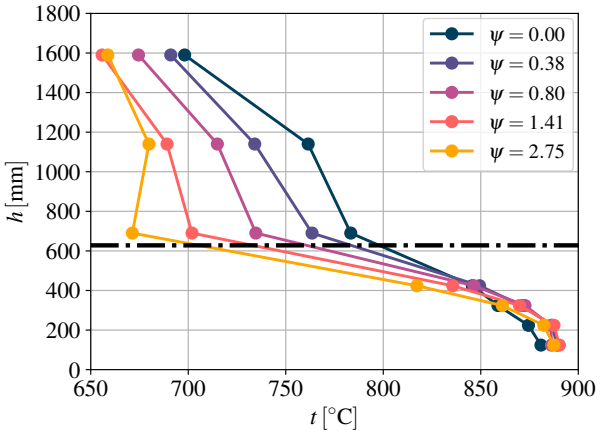

Figure 7. The dependence of the temperature height profile within the 30 kW_{th} BFB facility on the ratio of the secondary to primary air volumetric flows ψ in the case of a lignite combustion. The horizontal dash-and-dot line represents the height where the secondary air is injected.

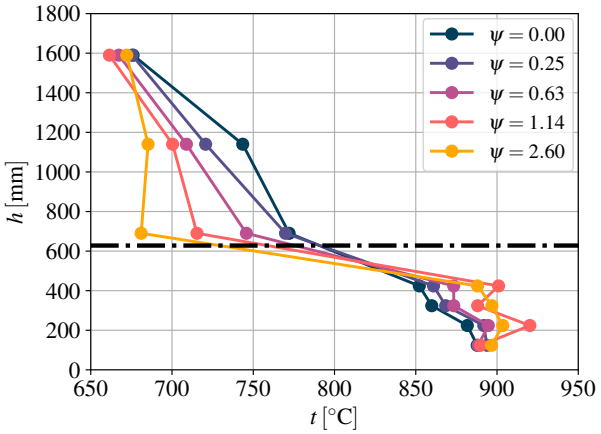

Figure 8. The dependence of the temperature height profile within the 30 kW_{th} BFB facility on the ratio of the secondary to primary air volumetric flows ψ in the case of a biomass combustion. The horizontal dash-and-dot line represents the height where the secondary air is injected.

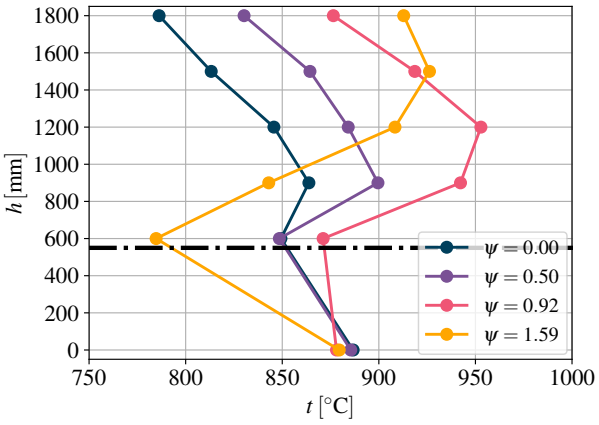

FIGURE 9. The dependence of the temperature height profile within the 500 kW_{th} BFB facility on the ratio of the secondary to primary air volumetric flows ψ in the case of a lignite combustion. The horizontal dash-and-dot line represents the height where the secondary air is injected.

4. CONCLUSION

The aim of the work was to experimentally verify the impact of air staging on NO_X emissions from combustion of coal and wooden biomass in BFB and to study the feasibility of providing sufficient conditions for the application of selective non-catalytic reduction of nitrogen oxides in BFB using two experimental combustors with thermal load 30 and 500 kW_{th}.

The experiments also showed that air staging itself is an effective primary measure for BFB to reduce NO_X formation. In the results from the 30 kW_{th} facility, the suppression of the NO_X directly correlated with an increased secondary/primary air flow ratio. The NO_X emissions reduction efficiency of about 55 % and 40 % was achieved in the case of lignite and biomass combustion, respectively. In the experiments carried out using the 500 kW_{th} facility, the best NO_X emissions reduction efficiency of 33 % was achieved for the secondary/primary air ratio ψ 0.92 and its further increase did not bring further NO_X reduction.

Due to the poor insulation of the freeboard section of the 30 kW_{th} BFB facility, it was not possible to increase the freeboard temperature to a value higher than the fluidized bed temperature for both fuels used. In the case of biomass combustion, the results confirmed that it is possible to reach the suitable temperature range for the SNCR of NO_X by air staging, but the secondary/primary air ratio must be significantly high, resulting in sub-stoichiometric conditions in the dense bed. However, a temperature increase was observed only in the well-insulated fluidized bed region below the secondary air inlets. For coal combustion, no positive impact of staged injection of combustion air was observed in the 30 kW_{th} facility. The experiments carried out with 500 kW_{th} BFB facility showed that if the combustion chamber and the freeboard section are properly insulated, the freeboard temperature increases with the increase of the secondary/primary air ratio. The ideal value of this ratio was approximately 1, for which the freeboard temperature was about 70 °C higher than the fluidized bed temperature. It can be expected that with insulation improvement of the 30 kW_{th} facility, the air staging would have a positive impact on the temperature profile for combustion of both fuels.

Recently, the insulation of the freeboard section of the 30 kW_{th} BFB facility was replaced with Insulfrax boards. Further experiments confirmed that temperature height profiles within the combustor are significantly improved. This study will continue with the characterization of the formation of gaseous pollutants in combustion of alternative biomass fuels in a BFB. In addition, the application of SNCR in the 500 kW_{th} BFB combustor will be studied.

ACKNOWLEDGEMENTS

This work was supported by the Ministry of Education, Youth and Sports under the OP RDE grant number CZ.02.1.01/0.0/0.0/16_019/0000753 “Research centre for low-carbon energy technologies”, which is gratefully acknowledged.

LIST OF SYMBOLS

BFB bubbling fluidized bed
LHV low heating value
LWA lightweight ceramic aggregate
PSD particle sized distribution
SCR selective catalytic reduction
$SNCR$ selective non-catalytic reduction
C_{CO} concentration of CO in the dry flue gas [mg/m^3_N]
C_{NO_X} concentration of NO_X in the dry flue gas [mg/m^3_N]
d_{10} 1st decile particle size [mm]
d_{90} 9th decile particle size [mm]
d_{50} median diameter [mm]
d_{mean} mean particle size [mm]
d_{mode} mode particle size [mm]
h height [mm]
m_{fuel} fuel load [$kg\,h^{-1}$]
N−NO conversion ratio of fuel nitrogen to NO [% mole]
t temperature [°C]
t_{BFB} temperature in the bubbling fluidized bed [°C]
u_o superficial gas velocity [$m\,s^{-1}$]
u_{mf} minimum fluidization velocity [$m\,s^{-1}$]
u_{mf-90} minimum fluidization velocity for d_{90} [$m\,s^{-1}$]
u_{t-90} terminal particle velocity for d_{90} [$m\,s^{-1}$]
u_t terminal particle velocity [$m\,s^{-1}$]
$V_{air\,prim}$ volumetric flow of primary air [m^3_N/h]
$V_{air\,sec}$ volumetric flow of secondary air [m^3_N/h]
λ_{prim} ratio of the air excess in the primary combustion zone [–]
ϕ_{O_2} volumetric fraction of O_2 in dry flue gas [% vol]
ρ_s density of solid material [$kg\,m^{-3}$]
ρ_b bulk density of solid material [$kg\,m^{-3}$]
ψ ratio of the secondary to primary air volumetric flows [–]

References

[1] Y. B. Zeldovich, P. Y. Sadovnikov, D. A. Frank-Kamenetskii. Oxidation of Nitrogen in Combustion. Tech. rep., Academy of Sciences of USSR, Institute of Chemical Physics, Moscow-Leningrad, 1947. Transl. by M. Shelef.

[2] I. Glassman, R. A. Yetter. *Combustion*. Academic Press, Elsevier, 4th edn., 2008.

[3] C. Fenimore. Formation of nitric oxide in premixed hydrocarbon flames. *Symposium (International) on Combustion* **13**(1):373–380, 1971. https://doi.org/10.1016/S0082-0784(71)80040-1.

[4] J. E. Johnsson. Formation and reduction of nitrogen oxides in fluidized-bed combustion. *Fuel* **73**(9):1398–1415, 1994. https://doi.org/10.1016/0016-2361(94)90055-8.

[5] J. Konttinen, S. Kallio, M. Hupa, F. Winter. NO formation tendency characterization for solid fuels in fluidized beds. *Fuel* **108**:238–246, 2013. https://doi.org/10.1016/j.fuel.2013.02.011.

[6] P. Skopec, J. Hrdlička, J. Opatřil, J. Štefanica. NO_X emissions from bubbling fluidized bed combustion of lignite coal. *Acta Polytechnica* **55**(4):275–281, 2015. https://doi.org/10.14311/AP.2015.55.0275.

[7] J. A. Miller, C. T. Bowman. Mechanism and modeling of nitrogen chemistry in combustion. *Progress in Energy and Combustion Science* **15**(4):287–338, 1989. https://doi.org/10.1016/0360-1285(89)90017-8.

[8] P. Glarborg, A. D. Jensen, J. E. Johnsson. Fuel nitrogen conversion in solid fuel fired systems. *Progress in Energy and Combustion Science* **29**(2):89–113, 2003. https://doi.org/10.1016/S0360-1285(02)00031-X.

[9] F. Winter, C. Wartha, G. Löffler, H. Hofbauer. The NO and N2O formation mechanism during devolatilization and char combustion under fluidized-bed conditions. *Symposium (International) on Combustion* **26**(2):3325–3334, 1996. https://doi.org/10.1016/S0082-0784(96)80180-9.

[10] K. Svoboda, M. Pohořelý. Influence of operating conditions and coal properties on NO_X and N2O emissions in pressurized fluidized bed combustion of subbituminous coals. *Fuel* **83**(7-8):1095–1103, 2004. https://doi.org/10.1016/j.fuel.2003.11.006.

[11] H. Stadler, D. Christ, M. Habermehl, et al. Experimental investigation of NO_X emissions in oxycoal combustion. *Fuel* **90**(4):1604–1611, 2011. https://doi.org/10.1016/j.fuel.2010.11.026.

[12] W. Fan, Y. Li, Q. Guo, et al. Coal-nitrogen release and NO_X evolution in the oxidant-staged combustion of coal. *Energy* **125**:417–426, 2017. https://doi.org/10.1016/j.energy.2017.02.130.

[13] H. Spliethoff, U. Greul, H. Rüdiger, K. R. Hein. Basic effects on NO_X emissions in air staging and reburning at a bench-scale test facility. *Fuel* **75**(5):560–564, 1996. https://doi.org/10.1016/0016-2361(95)00281-2.

[14] K. Sirisomboon, P. Charernporn. Effects of air staging on emission characteristics in a conical fluidized-bed combustor firing with sunflower shells. *Journal of the Energy Institute* **90**(2):316–323, 2017. https://doi.org/10.1016/J.JOEI.2015.12.001.

[15] S. L. Chen, J. A. Cole, M. P. Heap, et al. Advanced NO_X reduction processes using -NH and -CN compounds in conjunction with staged air addition. In *22nd Symposium (International) on Combustion*, pp. 1135–1145. The Combustion Institute, Pittsburgh, 1988.

[16] J. Hrdlička, P. Skopec, J. Opatřil, T. Dlouhý. Oxyfuel combustion in a bubbling fluidized bed combustor. *Energy Procedia* **86**:116–123, 2016. https://doi.org/10.1016/j.egypro.2016.01.012.

[17] D. Geldart. Types of gas fluidization. *Powder Technology* **7**(5):285–292, 1973. https://doi.org/10.1016/0032-5910(73)80037-3.

[18] D. Kunii, O. Levenspiel. *Fluidization Engineering*. Elsevier, 2nd edn., 1991. https://doi.org/10.1016/C2009-0-24190-0.

[19] I. G. C. Dryden (ed.). *Fluidized-bed combustion*, pp. 58–63. Butterworth-Heinemann, 2nd edn., 1982. https://doi.org/10.1016/B978-0-408-01250-8.50014-3.